Fall 2010

Effects of optimized and sub-optimum two degree of freedom lining tolerances on modeled inlet acoustic attenuation and normal incidence impedance measurement at elevated temperatures

David R. Burd

Department: Mechanical and Aerospace Engineering

EFFECTS OF OPTIMIZED AND SUB-OPTIMUM TWO DEGREE OF FREEDOM LINING TOLERANCES ON MODELED INLET ACOUSTIC ATTENUATION

and

NORMAL INCIDENCE IMPEDANCE MEASUREMENT AT ELEVATED TEMPERATURES

by

DAVID R. BURD

A DISSERTATION

Presented to the Faculty of the Graduate School of the

MISSOURI UNIVERSITY OF SCIENCE AND TECHNOLOGY

In Partial Fulfillment of the Requirements for the Degree

DOCTOR OF PHILOSOPHY

in

MECHANICAL ENGINEERING

2010

Approved by

Walter Eversman, Advisor
K. Krishnamurthy
Robert Landers
Kelly Homan
Vy K. Le

PUBLICATION DISSERTATION OPTION

There are two papers included in this dissertation. The first paper has been prepared in the style utilized by the *AIAA Journal*. The second paper has been prepared in the style utilized by the *Journal of Applied Acoustics*.

ABSTRACT

This work first investigates the effect of manufacturing tolerances on realized attenuation for two degree-of-freedom linings with the use of lining models and finite element duct propagation codes. Acoustic linings were created for two turbofan engines that optimize attenuation at takeoff/sideline and approach conditions. Lining physical and geometric parameters were set, which best meet the optimum impedance requirements at two target frequencies. Similar linings were created to investigate sub-optimum designs. Variations of these parameters representing realistic manufacturing tolerances were used to systematically examine the effect on installed impedance and predicted attenuation. Attenuation at sideline and approach conditions was found to be sensitive to manufacturing tolerances around optimum conditions. The results of the study are case dependent; however the analysis scheme presented provides a method for cost-benefit analysis of manufacturing processes. In a second study, an impedance tube, with an associated data analysis method, was developed and analyzed for temperature uncertainties that allowed the measurement of impedance of acoustic samples at elevated temperatures. This impedance measurement method was validated at room temperature by comparing the results with predicted impedance from empirically based impedance models and with impedance measurements in a standard traversing microphone impedance tube. Impedance for four samples was measured at elevated temperatures, and the results were compared to room temperature measurements. For two of the samples, the impedances measured at elevated temperatures were compared to the results of extensions of room temperature empirical models, confirming the trend of the results of the elevated temperature measurements.

ACKNOWLEDGMENTS

I would like to thank my advisor, Dr. Walter Eversman, for his tremendous support and guidance throughout my academic career. I had the advantage of having a mentor whose lifetime achievements have been recognized worldwide. Though he has reached the pinnacle of his profession, and I was only a student, he never treated me with anything less than a colleague's respect. He has my thanks and respect, and I intend to repay his generosity with dedication to a career that supports his legacy. I would also like to thank Spirit AeroSystems, Hawker Beechcraft, and Raytheon Aircraft for the opportunity to work on research that pushed the bounds of technology in industry and for providing the funding to support the research and further my academic career.

I would like to thank my committee members. Each member has influenced and helped further my academic career in his own way. Dr. Le, as one of my first contacts at the university, fueled my drive to take my educational career as far as I could and provided me with a strong mathematical base. Dr. Krishnamurthy pushed me to explore the world of robotics, controls, and microcontrollers. Dr. Landers expanded that foundation to newly emerging control system technologies and further encouraged my exploration in microcontrollers. And, Dr. Homan encouraged me to explore both analog and digital thermal instrumentation providing a basis for this work. I would not be the engineer that I am today without each of their efforts.

I would like to thank my family. No son could ask for the level of support they have provided me my entire life. My drive to succeed came from their lessons, and and my ability to succeed came from their actions.

TABLE OF CONTENTS

LIST OF ILLUSTRATIONS

PAPER 2

LIST OF TABLES

PAPER

1. EFFECTS OF OPTIMIZED AND SUB-OPTIMUM TWO DOF LINING TOLERANCES ON MODELED INLET ACOUSTIC ATTENUATION

ABSTRACT

This work investigates the effect of manufacturing tolerances on realized attenuation for two degree-of-freedom linings with the use of lining models and finite element duct propagation codes. Acoustic linings were created for two turbofan engines that optimize attenuation at takeoff/sideline and approach conditions. Lining physical and geometric parameters were set, which best meet the optimum impedance requirements at two target frequencies. Similar linings were created to investigate sub-optimum designs. Variations of these parameters representing realistic manufacturing tolerances were used to systematically examine the effect on installed impedance and predicted attenuation. Attenuation at sideline and approach conditions was found to be sensitive to manufacturing tolerances around optimum conditions. It was found that local lining impedance variation due to local sound pressure level also had a significant effect on realized attenuation in the sideline case. The results of the study are case dependent; however the analysis scheme presented provides a method for cost-benefit analysis of maintaining tight tolerances on manufacturing processes.

1. INTRODUCTION

Estimation of impedance of acoustic treatment is critically dependent on the fidelity of the model used to obtain a direct prediction based on design parameters. Murray, Ferrante, and Scofano [1], Jones, Parrott, and Watson [2], and Jones, Tracy, Watson, and Parrott [3] have investigated the effects of parameter variation on lining impedance for a single degree-of-freedom (one DOF) lining. In each case it was found that practical levels for manufacturing process tolerance can lead to significant variations in lining impedance. For the case of two degree-of-freedom (DOF) linings, several models are known to be in use, but they have been infrequently reported in the literature. Yu, Ruiz, and Kwan [4] have reported the essential features of the Goodrich model. The model is based on a combination of fundamental acoustic theory, fluid mechanics theory, and extensive empiricism. In the present study, impedance models are used that have been developed by Boeing and Spirit AeroSystems. The models are proprietary, however they are similar to the Goodrich model, and impedance predictions of both models produce similar results under similar circumstances. Some aspects of the models are discussed by Gallman and Kunze [5]. The models include a non-traditional septum with parameters similar to those investigated by Melling [6], Kraft, Yu, and Kwan [7], and Stinson and Shaw [8].

The conventional two degree-of-freedom (two DOF) lining consists of a perforated face sheet, a cavity behind the face sheet with depth referred to as the septum insertion depth, a perforated septum, and a rigidly backed cavity behind the septum.

Acoustic behavior in the cavities is well understood, leaving the impedance of the face sheet and septum as the critical elements of the model. Face sheet models lead to impedance dependent on grazing flow speed and sound pressure level (SPL) for both the traditional and non-traditional linings. Septum models are dependent on SPL, so the overall lining model is iterative to account for particle velocity at the face sheet and at the septum.

A conventional two degree-of-freedom lining having a composite face sheet that is perforated using a pin mat process and a laser drilled septum was the primary focus. There are, however, less conventional two degree-of-freedom linings that have been proposed. One of these was considered here. The septum was replaced by HexWeb® Acousti-Cap™ manufactured by Hexcel®. This was a weave material that was inserted in a single honeycomb core behind the face sheet (core depth comparable to the total thickness of a conventional two degree-of-freedom lining). The depth of insertion of the surface of this material behind the face sheet was equivalent to the septum insertion depth, and the material was equivalent to the septum in the conventional acoustic model. A model for this material based on several characteristic parameters has been the focus of extensive experimentation.

The linings considered in this investigation have been derived from an optimization philosophy that intended to maximize installed acoustic attenuation. In some cases this approach led to impedances that could not be achieved with physical parameters that are within manufacturing limits or that required excessive space (overall

lining depth). In these situations a “best” sub-optimum lining was synthesized. In the present investigation optimum and best sub-optimum lining designs were examined for two generic turbo-fan engine inlets. One represented a relatively small engine with high blade passage frequency, and the second was characteristic of a moderately sized engine. Acoustic treatment was designed to produce the highest attenuation of acoustic power at two flight conditions, take-off (sideline) and approach. The goal of this investigation was not to examine or critique the lining model. Rather, the goal was to examine the effect realizable manufacturing tolerances have on predicted impedance. In addition, the effect of manufacturing tolerances and installation effect on realized attenuation was examined.

2. TWO DEGREE-OF-FREEDOM LININGS

The accuracy of modeled impedance is a function of the fidelity of the model. A variety of models are available. Models such as the Goodrich model, discussed by Yu, Ruiz, and Kwan [4], allow direct prediction of estimated lining impedance based on design parameters. This model is an approximation based on acoustic theory and empirical data. The present study used models developed by Boeing and Spirit AeroSystems. The models are proprietary and discussed by Gallman and Kunze [5]. Impedance predictions are close to those obtained from the Goodrich model for similar conditions. The impedance models are iterative and based on theory and empirical data gathered over a period of many years.

Figure 1 shows the essential features of what is termed here as a conventional two DOF lining. It was composed of a perforated face sheet backed by a honeycomb face sheet cavity and a perforated septum that was in turn backed by a honeycomb septum cavity terminated by a rigid backing plate. The primary geometric and physical properties of this lining were the face sheet open area ratio (OAR), σ_{fs}, face sheet cavity depth (septum insertion depth), h_1, face sheet thickness, t_{fs}, face sheet hole diameter, d_{fs}, septum OAR, σ_s, septum cavity depth (backing cavity depth), h_2, septum thickness, t_s, and septum hole diameter, d_s. There are a number of manufacturing processes that can be used to produce the face sheet and septum, and the impedance models for these components of the lining are specific to the process used. In this investigation the

conventional lining had a composite face sheet perforated by a pin mat process and a septum that was perforated by laser drilling.

Figure 2 is a schematic of the less conventional lining. The face sheet was backed by a single monolithic honeycomb cavity with a rigid backing plate. At a specified depth Hexcel® HexWeb® Acousti-Cap™ weave was inserted to act as a septum. The lining had two layers. One consisted of the face sheet and face sheet cavity, as in the conventional lining, and one consisted of the weave acting as a septum with its backing space. The geometric and physical properties of this construction included the familiar ones for the first layer that were the face sheet OAR, σ_{fs}, septum insertion depth (depth of the weave surface), h_1, face sheet thickness, t_{fs}, and face sheet hole diameter, d_{fs}. Septum parameters were quite different and included septum non-linearity factor, F_{nl}, septum DC flow resistance, R_{dc}, and cross frequency, f_c. The process of insertion of the weave material in the honeycomb to act as a septum produced a slightly concave surface reminiscent of a meniscus. For this reason the septum insertion depth, h_1, and the septum cavity depth, h_2, were taken as defined by the mean location of the "meniscus". In the case of both lining configurations the face sheet was exposed to grazing flow characterized by grazing flow Mach number and boundary layer momentum thickness.

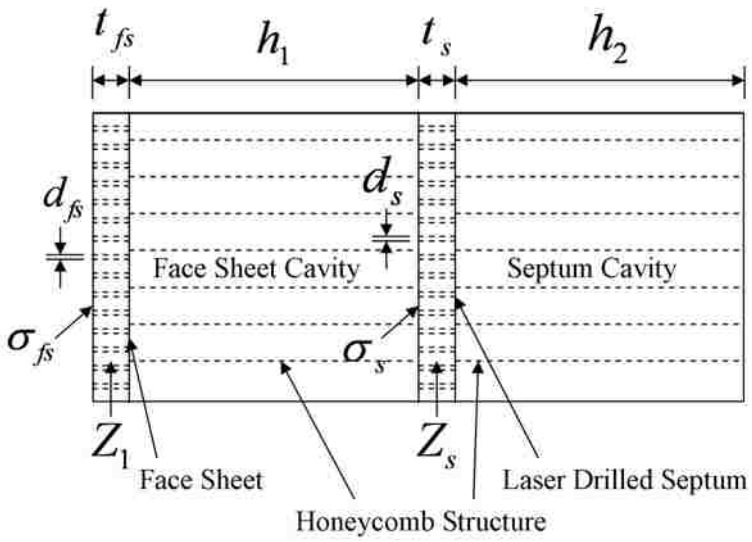

Figure 1. Schematic of two DOF lining with a laser drilled septum.

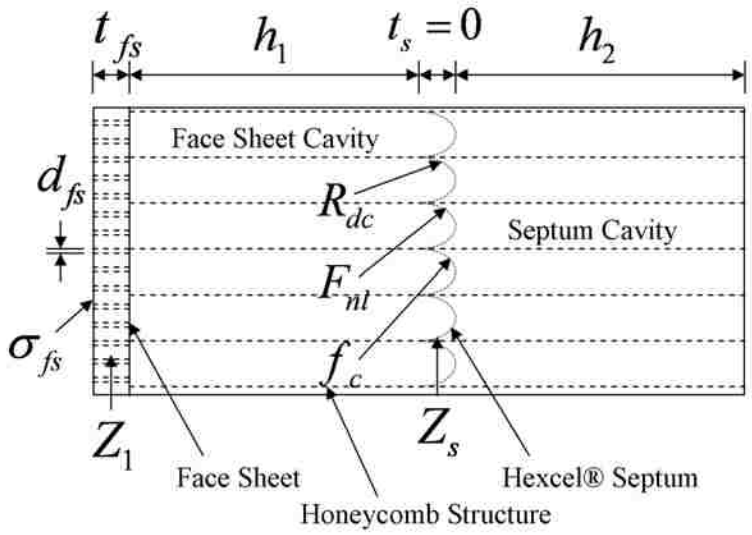

Figure 2. Schematic of two DOF lining with a Hexcel® septum.

3. ACOUSTIC MODELING

This investigation sought to determine how manufacturing tolerances in several physical parameters characterizing two DOF linings affect installed impedance and realized attenuation in a duct with geometry related to a turbofan engine inlet. For this purpose a suite of computer codes in FORTRAN and MATLAB were used. The codes break down into two categories: those associated with lining impedance models and those used for modeling acoustic propagation.

3.1. Models for Two Degree-of-Freedom Linings

The impedance Z of a two DOF lining can be given in terms of the components of the lining by [4],

$$Z = R + iX = Z_1 + \frac{Z_S \dfrac{\cos\left(kh_1\right)\sin\left(kh_2\right)}{\sin\left(kh\right)} - i\cot\left(kh\right)}{1 + i\,Z_S \dfrac{\sin\left(kh_1\right)\sin\left(kh_2\right)}{\sin\left(kh\right)}}, \tag{1}$$

where R is the assembled lining resistance, X is the assembled lining reactance, Z_1 is the face sheet impedance, Z_S is the septum impedance, h_2 is the septum backing cavity depth, h_1 is the face sheet backing space depth (septum insertion depth), and $h = h_1 + h_2$. Figures 1 and 2 show the geometry of the two DOF linings considered here. Face sheet impedance and septum impedance were individually represented by models that depended on the geometric and physical parameters applicable to the specific case. Impedance models for the conventional perforates used for face sheet and septum are

suggested in [4]. In this investigation a similar proprietary model developed by Boeing and Spirit AeroSystems was used with the expectation that no substantial difference in conclusions resulted.

A combination of FORTRAN and MATLAB codes was used to model the impedance given by Eq. (1). The critical elements of the codes were subroutines that produce the face sheet impedance Z_1 and septum impedance Z_S for specific cases. In the current case models for a composite perforate (face sheet), a laser drilled perforate (septum), and the HexWeb® Acousti-Cap™ weave by Hexcel® (septum) were considered. These codes included the non-linear effect of acoustic particle velocity on the component impedances and iteratively converged on impedance consistent with a specified incident acoustic SPL spectrum. This process is outlined in [4].

Related to the lining model was a code that began with two target impedances at two specified target frequencies and operating conditions and searched for a combination of face sheet and septum impedance and face sheet backing depth (septum insertion depth) and septum backing space depth with other lining parameters held fixed that came closest to producing the target impedances. Two approaches were used to search the parameter space. The methods used were the down hill Simplex method [9] and particle swarm optimization [10]. Both methods converged to the same result, but particle swarm optimization required a much less refined initial estimate, because it was a global search capable of handling a search domain topography with several local minimums or near minimums.

3.2. Propagation Models

Propagation and attenuation in a realistic model of a turbofan inlet was investigated using several finite element codes that modeled propagation in a non-uniform axi-symmetric duct with a potential mean flow [11-15]. The duct cross-section was contoured to represent the inlet, but the termination was reflection free. A number of benchmarks comparing this propagation code to one that includes radiation to the far field (radiation code) [15] have established that acoustic power attenuation due to the installation of acoustic treatment is well predicted by the simpler propagation code with the advantage of increased computational efficiency. A feature of the propagation code is the statistical modeling of the source [16, 17]. The source is represented in a specified circumferential mode with all propagating radial modes with modal amplitude and phase randomly chosen. Each random representation of the source represents one trial among many (typically 1000 trials). Lining performance is quantified by statistical measures over the many trials, such as mean (expected) acoustic power attenuation, maximum and minimum attenuation, and other statistical measures such as standard deviation about the mean. Expected attenuation is used as the metric to asses lining performance in this investigation. The usual implementation of this code has provisions for acoustic treatment that is segmented into three lengths for which impedance is specified. A variant of the code is coupled with the lining model discussed in Section 5.1. so that lining parameters are specified, and lining impedance is computed locally. The principal advantage to this form is that the dependence of impedance on local grazing flow Mach number and SPL can be taken into account.

The propagation code also is the core of an optimization code. In the optimization process a uniform lining impedance is sought that produces the maximum expected acoustic power attenuation for a source of specified circumferential mode and a random representation of the radial modes. The search is managed by the downhill Simplex method. In the typical use of this code for the case of a two DOF lining, optimum impedance is determined for two target engine operating points, and these target impedances were used in the search process described previously to set lining physical parameters that best met the impedance targets.

The suite of propagation codes also includes a version that produces an impedance map (a contour plot of attenuation on Cartesian axes of resistance and reactance axis). The impedance map is useful for the assessment of sensitivity of attenuation to perturbations in impedance or to pick sub-optimum impedance that meets attenuation requirements.

4. OPTIMIZED LINING DESIGN

Assessment of the effect of manufacturing tolerance on impedance and performance of acoustic linings was done in the context of linings designed to meet realistic goals. Two representative inlet geometries, source models, and operating conditions are used. Both ducts had the same contour defined by non-dimensional radius as a function of non-dimensional axial location as shown in Fig 3. Both radius and axial location were non-dimensional with respect to source plane radius. The lining location and length were the same for both ducts non-dimensionally beginning at $0.23R_f$ forward of the source plane and ending at $0.93R_f$. R_f was the source plane (fan) radius. The two geometry/source model/operating condition combinations are referred to as the smaller duct and the larger duct. A two DOF lining with a laser drilled buried septum and a two DOF lining with a Hexcel® septum were designed for the larger duct and the smaller duct. In the unconstrained design process it will be shown here that physical parameters required to meet the target impedances were not acceptable on the basis of conventional manufacturing capability, particularly with respect to septum insertion depth and backing cavity depth. These shortcomings also contributed to exceptional sensitivity to manufacturing errors if tolerances were assumed to be independent of the nominal parameter value. For this reason additional "best" sub-optimum lining designs were designed with parameters constrained to lie within a feasible design space. This resulted in eight separate physical two DOF linings.

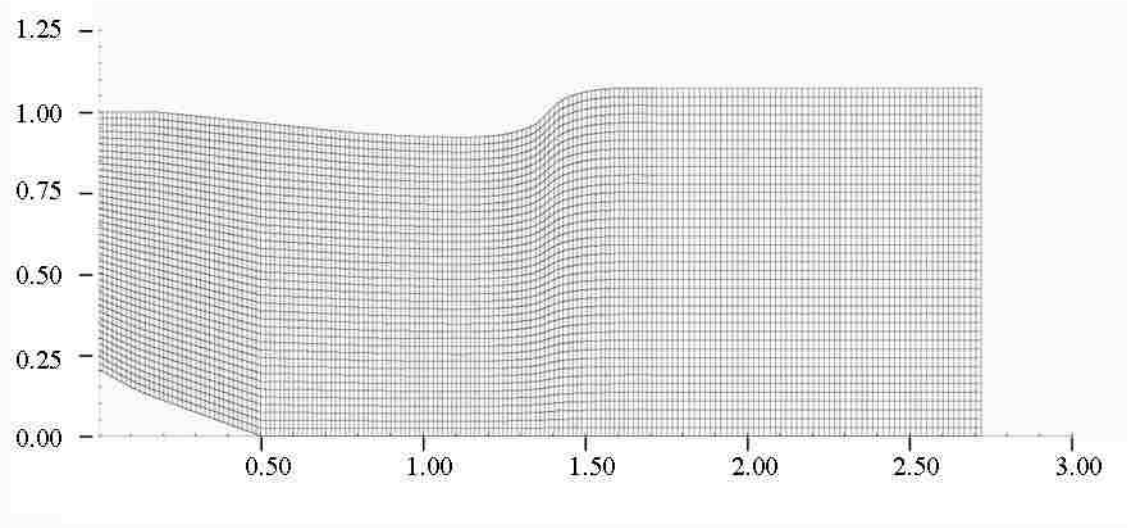

Figure 3. Non-dimensional inlet duct contour for both engines.

Each lining was designed to produce the best attenuation at both the sideline and approach operating conditions. The sideline condition was characterized by a spectrum dominated by a rotor locked pure tone at blade passage frequency with only a few propagating radial modes. The optimum lining was relatively sharply tuned and produced a very high attenuation. Typically the optimum impedance would require a high resistance. For the approach condition, the spectrum may have an identifiable tone at twice blade passage frequency, but this tone was at a low circumferential mode number with many propagating modes. In this case an optimum lining produced much more modest attenuation.

4.1. Inlet Geometry, Source Model, and Operating Conditions for the Smaller Duct

For the smaller duct the source had a 22 blade fan with 52 exit guide vanes. The fan radius was $R_f = 14.5$ in. One target operating condition was representative of blade

passage frequency at takeoff (sideline) condition at 10,999 RPM. This corresponded to a blade passage frequency of 4033 Hz. The non-dimensional frequency was $\eta = 2\pi f R_f / c = 27.41$. The speed of sound was $c = 1117\ ft/sec$. The source was circumferential mode $m = 22$. The source one-third octave band spectrum for this operating condition is shown in Fig. 4. SPL in the targeted 4 kHz one-third octave band (band 20) was 152 dB with an overall SPL of 154.7 dB. This exceeded the broadband spectrum level by 3 dB. The grazing flow Mach number was 0.537 at the source plane.

The second target operating condition was representative of the interaction tone at twice blade passage frequency at approach at 7150 RPM. Twice blade passage frequency was 5243 Hz. The non-dimensional frequency was $\eta = 35.63$. The source was in circumferential mode $m = -8$. The source one-third octave band spectrum for this operating condition is shown in Fig. 5. SPL in the 5 kHz one-third octave band (band 21) was 135 dB with an overall SPL of 140.9 dB. This exceeded the broadband spectrum level by only 0.8 dB. The duct Mach number at the source was 0.3.

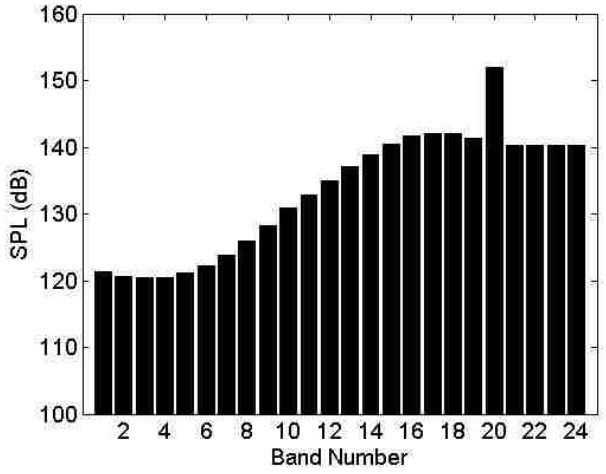

Figure 4. Source spectrum for takeoff (sideline) operating condition for the smaller engine.

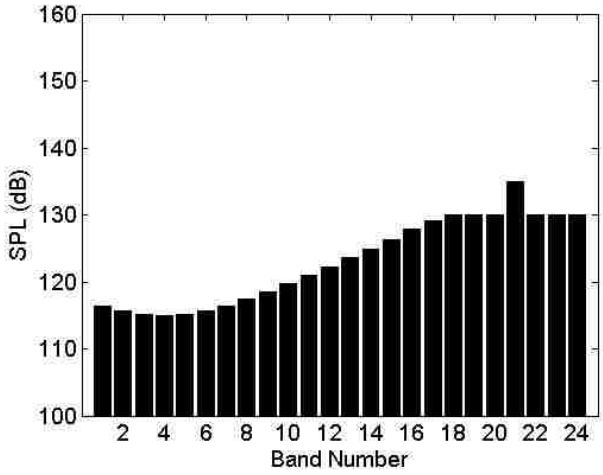

Figure 5. Source spectrum for approach operating condition for the smaller engine.

4.2. Inlet Geometry, Source Model, and Operating Conditions for the Larger Duct

In the case of the larger duct the source had a 24 blade fan with 56 exit guide vanes, and the fan radius was $R_f = 40.0$ in. As in the case of the smaller duct, the first target operating condition was representative of blade passage frequency at the takeoff

(sideline) condition. This corresponded to 4166 RPM and a blade passage frequency of 1666 Hz. The non-dimensional frequency was $\eta = 2\pi fR_f / c = 31.25$, and the speed of sound was $c = 1117\ ft/sec$. The source was circumferential mode $m = 24$. The source one-third octave band spectrum for this operating condition is shown in Fig. 6. SPL in the targeted 1.6 kHz one-third octave band (band 16) was 158.2 dB with an overall SPL of 160.7 dB exceeding the broadband spectrum level by 3.1 dB. The source plane Mach number was 0.55.

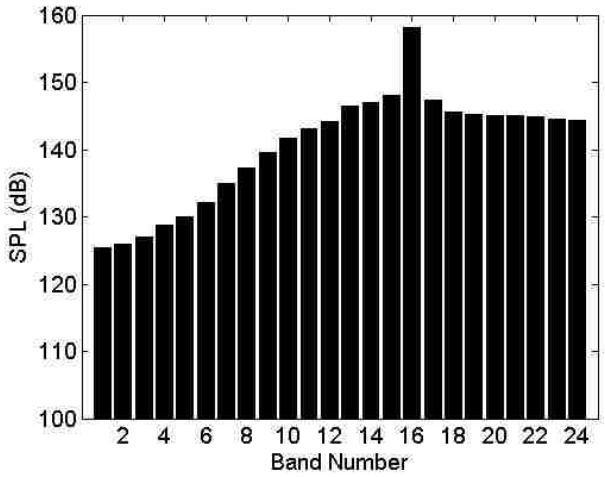

Figure 6. Source spectrum for takeoff (sideline) operating condition for the larger engine.

The second target operating condition was representative of the interaction tone at twice blade passage frequency at approach at 2916 RPM, which was twice the 2333 Hz blade passage frequency. The non-dimensional frequency was $\eta = 43.73$ with a source circumferential mode of $m = -8$. The source one-third octave band spectrum for this operating condition is shown in Fig. 7. SPL in the 2.5 kHz one-third octave band (band

18) was 131.6 dB with an overall SPL of 140.3 dB. This exceeded the broadband spectrum level by only 0.3 dB. The source plane Mach number was 0.35.

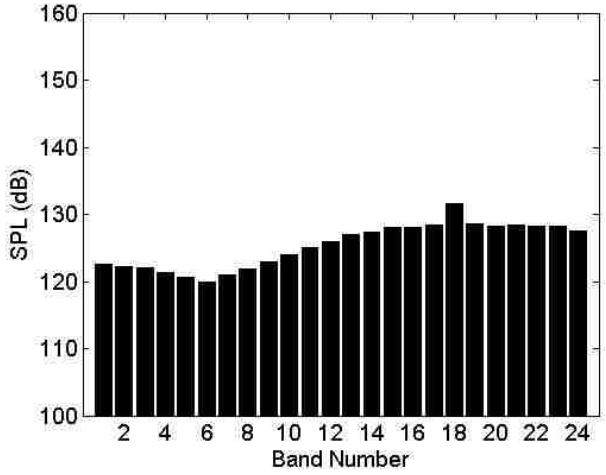

Figure 7. Source spectrum for approach operating condition for the larger engine.

4.3. Physical and Geometric Parameters for Each Optimum Lining

Two lining types were considered. One had conventional construction with a pin mat perforated face sheet and a laser drilled septum. The second had the same type of perforated face sheet with a HexWeb® Acousti-Cap™ septum made by Hexcel®. The design goal was to achieve the best attenuation at the two target conditions. Optimum impedance for the duct lining was found at each of the operating conditions. Then the physical lining parameters were determined based on target impedances, operating conditions, and physical manufacturing limitations.

Two operating conditions require that two impedance conditions be met simultaneously for each lining. One impedance provided optimum attenuation at the

sideline condition, and the other provided optimum attenuation at the approach condition. The optimum impedance for the sideline condition for the smaller duct was $Z = 6.11 - 1.20i$, and the optimum impedance for the approach condition was $Z = 2.70 - 0.38i$. The optimum impedance for the sideline condition for the larger duct was $Z = 7.73 - 0.85i$, and the optimum impedance for the approach condition was $Z = 3.14 - 0.31i$. A high resistance for a lining optimized for rotor locked blade passage frequency at the sideline condition is typical.

The models used to calculate lining impedance are based on operating condition and geometric and physical parameters. Required physical parameters cannot be back-calculated directly from desired impedance and operating conditions. Instead, impedance is calculated for multiple combinations of geometric and physical parameters at the operating condition. When the calculated impedance matches the desired impedance, the geometric and physical parameters are recorded as the design values. A systematic search based on Particle Swarm Optimization (PSO) was proven to be satisfactory for this application.

In order to find the geometric and physical lining parameters that would generate the optimum impedance at each operating condition, four parameters were allowed to vary in each model. Parameters that remain fixed in the design process were ones considered to be constrained to limited choices due to manufacturing and material property limitations. For the laser drilled septum lining model, face sheet OAR, σ_{fs}, face sheet backing space depth (septum insertion depth) h_1, septum OAR σ_S, and backing

cavity depth h_2 were allowed to vary. For the Hexcel® septum lining model, face sheet OAR, σ_{fs}, septum insertion depth, h_1, septum DC flow resistance R_{dc}, and backing cavity depth h_2 were allowed to vary. The parameter search domain was a primary input for PSO. It also required maximum and minimum allowable changes for each parameter. This allowed parameter domains of drastically different magnitudes to be searched simultaneously with no alteration of the algorithm. This search method was particularly well suited to this application, because of the topography of the search domain. There were several local minima that make traditional search routines less effective.

For the lining with the laser drilled septum, septum insertion depth and septum backing cavity depth were allowed to vary between 0.01 and 3 in. Face sheet and septum OAR were allowed to vary between 0.001and 0.4. For the lining with the Hexcel® septum, septum insertion depth and septum backing cavity depth were allowed to vary between 0.01 and 3 in. Face sheet OAR was allowed to vary between 0.001 and 0.4. The DC flow resistance was allowed to vary between 80 and 400 cgs Rayls.

For the conventional lining, fixed parameters were face sheet thickness $t_{fs} = 0.04$ in, face sheet hole diameter $d_{fs} = 0.043$ in, and boundary layer momentum thickness $\delta = 0.079$ in. For the lining with Hexcel® weave septum, face sheet parameters were the same, septum non-linearity factor $F_{nl} = 1.6$, and septum cross frequency $f_c = 10,000$ Hz.

For each lining in the smaller and larger ducts, the parameter search was able to yield a lining that exactly met the requirement for optimum impedance at the two operating conditions. Though satisfying the search, values of some parameters may not be considered acceptable, and this is addressed below. Optimum normalized impedance yielded expected acoustic power attenuation of 38 dB for the sideline condition and 5 dB for the approach condition in the smaller duct. The sideline and approach condition attenuations were 33 dB and 4 dB respectively in the larger duct. A summary of the lining designs follows in Table 1 and Table 2. The precision is intentional as the models were highly sensitive to parameter variation near the optimum design values. Dimensions are shown in centimeters and inches.

Table 1. Optimum lining parameters for the smaller duct.

Optimum Design				
Design parameter	Smaller duct - Pin mat face sheet/laser drilled buried septum		Smaller duct - Pin mat face sheet/Hexcel® septum	
Face sheet OAR	0.0229		0.0329	
Face sheet thickness, in (cm)	0.0400	(0.1016)	0.0400	(0.1016)
Face sheet hole diameter, in (cm)	0.0430	(0.1092)	0.0430	(0.1092)
Septum insertion depth, in (cm)	0.1264	(0.3211)	0.0714	(0.1814)
Septum OAR	0.009		N/A	
Septum thickness, in (cm)	0.0300	(0.0762)	N/A	
Septum hole diameter, in (cm)	0.0080	(0.0203)	N/A	
Septum backing depth, in (cm)	1.1056	(2.8082)	2.6501	(6.7313)
Septum non-linearity factor	N/A		1.6	
Cross frequency, Hz	N/A		10000	
Septum DC flow resistance, cgs Rayls	N/A		317.09	

Table 2. Optimum lining parameters for the larger duct.

Optimum Design				
Design parameter	Larger duct - Pin mat face sheet/laser drilled buried septum		Larger duct - Pin mat face sheet/Hexcel® septum	
Face sheet OAR	0.0168		0.017	
Face sheet thickness, in (cm)	0.0400	(0.1016)	0.0400	(0.1016)
Face sheet hole diameter, in (cm)	0.0430	(0.1092)	0.0430	(0.1092)
Septum insertion depth, in (cm)	0.4286	(1.0886)	0.3657	(0.9289)
Septum OAR	0.0114		N/A	
Septum thickness, in (cm)	0.0300	(0.0762)	N/A	
Septum hole diameter, in (cm)	0.0080	(0.0203)	N/A	
Septum backing depth, in (cm)	2.607	(6.6218)	2.7623	(7.0162)
Septum non-linearity factor	N/A		1.6	
Cross frequency, Hz	N/A		10000	
Septum DC flow resistance, cgs Rayls	N/A		284.23	

Several parameter values were not suited for manufacture and installation in the duct. For the smaller duct with the conventional lining, it would likely be concluded that the septum insertion depth was too small. In the case of the lining with the Hexcel® septum, the septum insertion depth was too small, and the septum backing cavity depth may have been too large. This indicated that a “best” sub-optimum design was required for a physically realizable design. Installed attenuation was maximized while design parameters were constrained to manufacturable values. The level of attenuation for the sub-optimum design is equal or less than the level of optimum attenuation.

Similar to the cases with the smaller duct, some parameter values were not suited for manufacture and installation in the larger duct. For the conventional lining, the

backing cavity depth was too large. A similar problem existed with the Hexcel® septum lining. Once again a sub-optimum design was required for manufacture.

The optimum impedances and attenuations were typical for the two operating conditions. Rotor locked blade passage frequency can generally be well attenuated with a lining having a high resistance. The twice blade passage frequency interaction tone exhibited significant, but lower attenuation levels. Impedance maps can be used to visualize the optimization and sensitivity to impedance variation at the two operating conditions for each lining. Figures 8 and 9 are impedance maps for the smaller duct. Figure 8 is an impedance map for an optimized lining for the sideline operating condition. It is centered on the optimum impedance $Z = 6.11 - 1.20i$ and reveals a sharp peak in attenuation near the optimum resulting in high sensitivity to variation in resistance and reactance near the optimum. Figure 9 is the equivalent impedance map for the approach condition centered on the optimum impedance $Z = 2.70 - 0.38i$. It confirms the much lower optimum attenuation and shows less sensitivity to variation in resistance and reactance near the optimum. Figures 10 and 11 show similar impedance maps for the larger duct. Since the achievable impedance is not constrained by limiting the lining physical parameters, the impedance maps are independent of the type of lining.

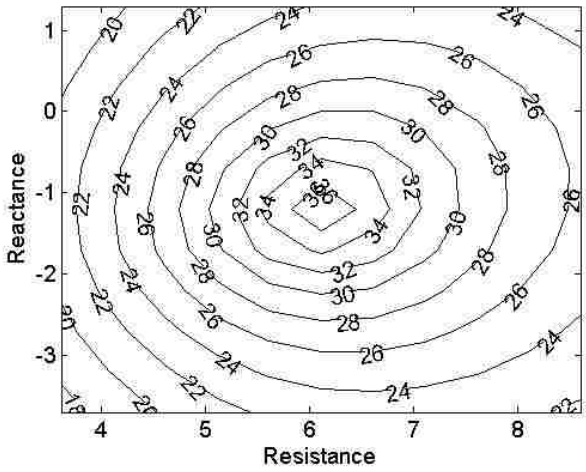

Figure 8. Contour plot of smaller duct attenuation sensitivity to impedance deviation for the sideline condition.

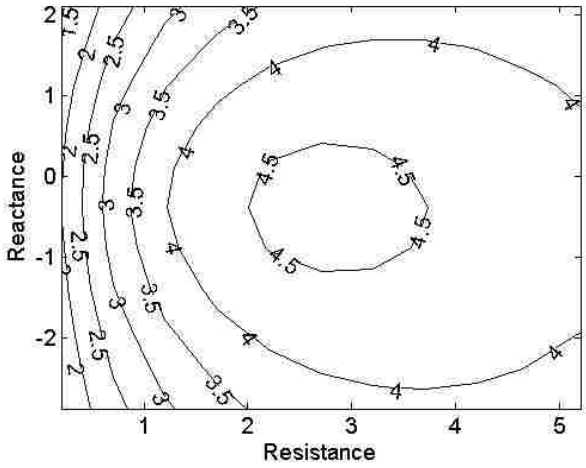

Figure 9. Contour plot of smaller duct attenuation sensitivity to impedance deviation for the approach condition.

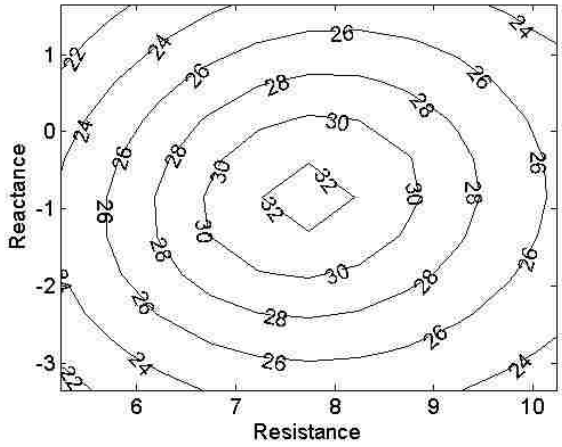

Figure 10. Contour plot of larger duct attenuation sensitivity to impedance deviation for the sideline condition.

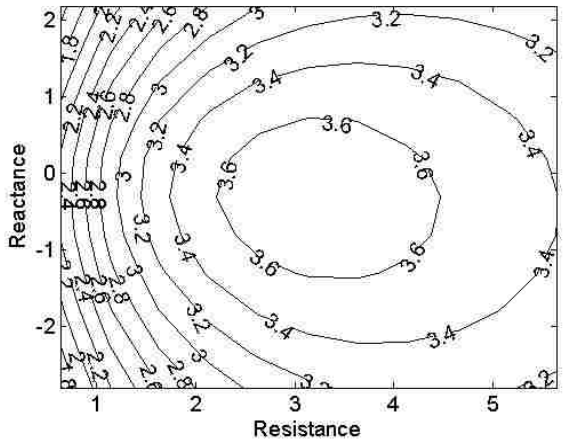

Figure 11. Contour plot of larger duct attenuation sensitivity to impedance deviation for the approach condition.

5. IMPEDANCE AND ATTENUATION ANALYSIS FOR OPTIMUM LINING DESIGNS

Impedance maps provide an indication of how realized attenuation is sensitive to the installed impedance. Impedance is in turn dependent on the geometric and physical parameters of the lining, and these parameters are designated as nominal values with some manufacturing tolerance. Because of these tolerances, the optimized linings will exhibit off-design impedance characteristics. The flight condition for which an optimized lining is designed is an approximation of the physical environment to which the lining will be subjected. While in flight some variation of the flight condition is expected. This will also contribute to impedance variation. These impedance variations may lead to degraded attenuation. The assembled two DOF linings with the laser drilled septum and the assembled two DOF linings with the Hexcel® septum are each modeled with eight geometric and physical parameters. Each of these parameters has a nominal value, an upper bound, and a lower bound based on the manufacturer's ability to maintain tolerance. The effects of these variations will be examined with two separate sets of numerical experiments.

In the first set, a range of operating conditions is considered, each defined by a combination of SPL spectrum and grazing flow Mach number. For each combination the effect of manufacturing tolerances on impedance is determined. This set of numerical experiments is used to determine whether the effect of changing operating conditions or the effect of manufacturing tolerances is most important in uncertainties in realized impedance. The cost-benefit of tightening manufacturing process tolerances can then be

considered relative to expected variation in the flight condition model. If the manufacturing process tolerances dominate the modeled impedance variation, then a low relative sensitivity of impedance variation to operating condition variation has been demonstrated. This justifies the use of a single operating condition in the second set of numerical experiments.

The second set of numerical experiments considers only the specific operating conditions for which the linings were designed. For these conditions, the effect of manufacturing tolerances on impedance is determined in two ways, and the impact of the magnitude of the impedance variations is determined by evaluating the effect on acoustic power attenuation in the duct. First, the largest impedance deviations due to all possible combinations of the manufacturing tolerances are found, and the associated attenuations are calculated. This indicates the range of attenuations that can be expected given known manufacturing process tolerances. Next, only one manufacturing tolerance is varied at a time to evaluate the magnitude of individual manufacturing tolerance effects on impedance. The single parameter variation impedance data are compared with the multiple parameter variation impedance and attenuation data to indicate which single manufacturing tolerance contributed most significantly to the maximum drop in attenuation. For example, assume that an increase in resistance and an increase in reactance both due to multiple parameter variation lead to the largest loss of attenuation. The single parameter variation data would be examined to determine which individual parameter variation led to the largest increase in resistance and which individual

parameter variation led to the largest increase in reactance. This information can then be used to more effectively identify problem areas in the manufacturing process.

The end result of these simulations is intended to provide a process for cost-benefit analysis of lining manufacturing processes in the sense that it will identify what parameter variations from nominal led to the largest potential for degrading lining performance. Presented here is a method for cost-benefit analysis. Manufacturing tolerance values are assumed independent of nominal parameter values. Each lining design is different, so the percentage of the nominal value that a parameter is allowed to vary can change significantly. Therefore the results cannot be generalized to other lining designs.

5.1. Impedance Variation with a Broad Range of Operating Conditions and Tolerance Combinations

The first investigation was an exhaustive search of multiple operating conditions and multiple values for geometric and physical parameter values within manufacturing tolerances. The goal of this investigation was to determine the influence of operating conditions on uncertainty in realized impedance related to manufacturing tolerances.

A nominal value, an upper tolerance bound, and a lower tolerance bound for each of the eight physical parameters yields 3^8 or 6561 possible physical models that could result from a single lining design at a single operating condition. In order to determine the largest deviation in the resistance and reactance that could result from these tolerances, the impedance for each of the possible physical configurations was evaluated at each

desired operating condition. For each operating condition, out of the 6561 models, the largest upper and lower deviation from the impedance of the lining with nominal geometric and physical properties at each frequency band was recorded. Though there are a large number of models, the calculation proceeded quickly.

For the smaller duct, each lining was modeled with grazing flow Mach numbers of 0.17, 0.3, and 0.5 and one third octave band sound spectra, constant over frequency bands between 50 and 10,000 Hz, with band levels of 80, 90, 100, 110, 120, 130, 140, and 150 dB. These correspond to overall levels of 94, 104, 114, 124, 134, 144, 154, and 164 dB, respectively. For the larger duct, each lining was modeled with grazing flow Mach numbers of 0.2, 0.4, and 0.6. The SPL spectra were the same as those used in the smaller duct. For this investigation physical and geometric parameters were taken as the nominal values (as designed) with upper and lower values set by estimates of manufacturing tolerances. Some tolerances are related to manufacturing processes, and others are related to methods available for verifying parameter values. Parameter ranges are shown in centimeters and inches in Table 3:

Table 3. Parameter tolerance ranges.

Design parameter tolerance	Pin mat face sheet/laser drilled buried septum		Pin mat face sheet/Hexcel® septum	
Face sheet OAR	± 0.01		± 0.01	
Face sheet thickness, in (cm)	± 0.005	(0.013)	± 0.005	(0.013)
Face sheet hole diameter, in (cm)	± 0.005	(0.013)	± 0.005	(0.013)
Septum insertion depth, in (cm)	± 0.020	(0.051)	± 0.020	(0.051)
Septum OAR	± 25% of OAR		N/A	
Septum thickness, in (cm)	± 0.002	(0.005)	N/A	
Septum hole diameter, in (cm)	± 0.0005	(0.001)	N/A	
Septum backing depth, in (cm)	± 0.060	(0.152)	± 0.060	(0.152)
Septum non-linearity factor	N/A		± 0.1	
Cross frequency Hz	N/A		± 500	
Septum DC flow resistance cgs Rayls	N/A		± 15	

The largest upper and lower deviations in the resistance and reactance of the impedance are displayed in a single plot with the nominal value in order to demonstrate the possible range of impedance that could be expected for the lining in question at the specified operating condition considering all possible manufacturing tolerance combinations. The results shown in Fig. 12 through Fig. 19 were typical of the results found at each SPL spectrum and Mach number combination for each lining in the smaller duct for the optimum design.

Figures 12 and 13 show the resistance for the lining with the laser drilled septum in the smaller duct for the optimum design at operating conditions having one-third octave band spectrum levels of 100 dB or 130 dB respectively. Both have a grazing flow Mach number of 0.3. Figures 14 and 15 are the companion results for reactance. Figure 16 through Fig. 19 repeats the same operating conditions with the Hexcel® septum.

The optimum cases showed maximum sensitivity to parameter variations near the design target frequencies of 4033 Hz and 5243 Hz in the smaller duct. It is clear that the impedance of the lining with the laser drilled septum was very sensitive to small changes in geometric parameters. This was particularly true for the resistance on the high side. The tolerance in the septum insertion depth was large relative to the nominal value for the optimized linings. This, in conjunction with the fact that the lining model was highly sensitive to changes in septum insertion depth, explains why the deviations in impedance near the design conditions were so pronounced.

In both ducts the lining with the Hexcel® septum was less sensitive, but the uncertainty bounds in impedance were still significant. And, though the effects of SPL were clearly present in the resistance for the laser drilled septum, the general trend of the uncertainty was due primarily to manufacturing tolerances. When the impedance ranges seen in Fig. 12 through Fig. 19 were compared with the attenuation levels shown in the impedance maps of Figs. 8 and 9, the potential effects on attenuation became clear. In this comparison it should be noted that operating conditions were not the same, so the observation is qualitative, suggesting that manufacturing tolerance levels can cause significant deviations from the design attenuation.

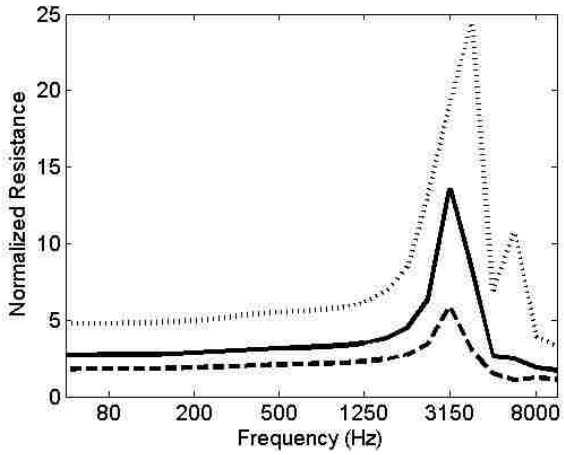

Figure 12. Resistance uncertainty for the optimum lining with the laser drilled septum in the smaller duct. The operating condition includes a grazing flow Mach number of 0.3 and third octave band levels of 100 dB across the spectrum. [… Upper Bound, ── Nominal, ----- Lower Bound]

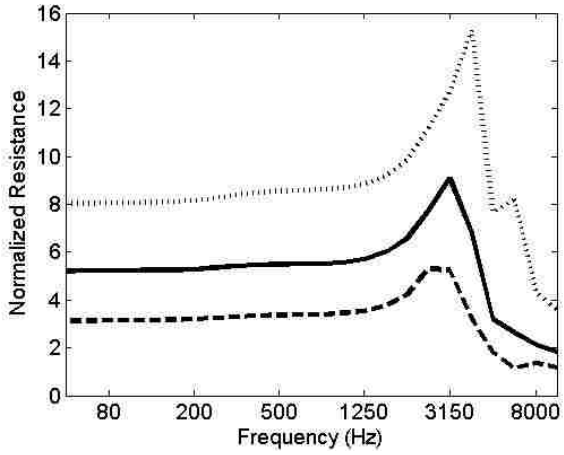

Figure 13. Resistance uncertainty for the optimum lining with the laser drilled septum in the smaller duct. The operating condition includes a grazing flow Mach number of 0.3 and third octave band levels of 130 dB across the spectrum. […
Upper Bound, ── Nominal, ----- Lower Bound]

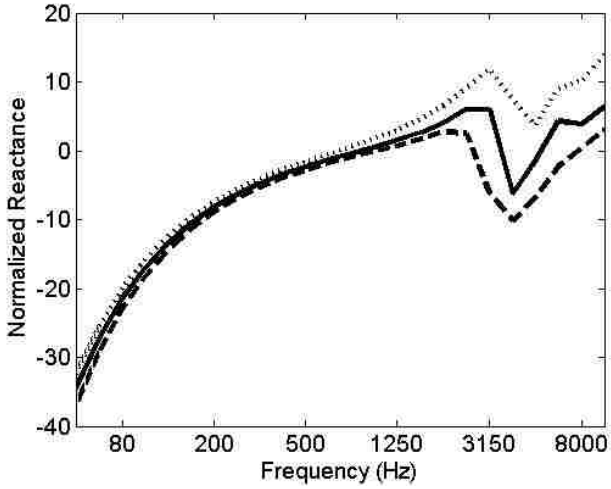

Figure 14. Reactance uncertainty for the optimum lining with the laser drilled septum in the smaller duct. The operating condition includes a grazing flow Mach number of 0.3 and third octave band levels of 100 dB across the spectrum. [… Upper Bound, ── Nominal, ----- Lower Bound]

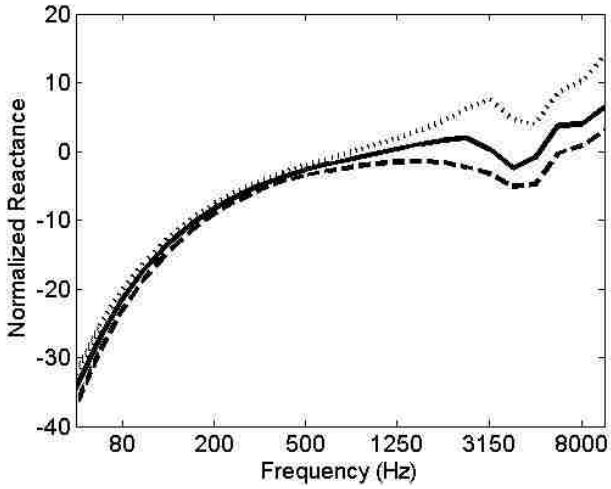

Figure 15. Reactance uncertainty for the optimum lining with the laser drilled septum in the smaller duct. The operating condition includes a grazing flow Mach number of 0.3 and third octave band levels of 130 dB across the spectrum. [… Upper Bound, ── Nominal, ----- Lower Bound]

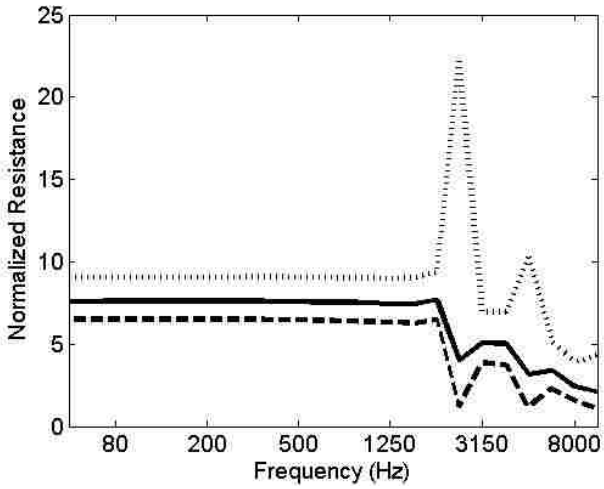

Figure 16. Resistance uncertainty for the optimum lining with the Hexcel® septum in the smaller duct. The operating condition includes a grazing flow Mach number of 0.3 and third octave band levels of 100 dB across the spectrum. [… Upper Bound, ── Nominal, ----- Lower Bound]

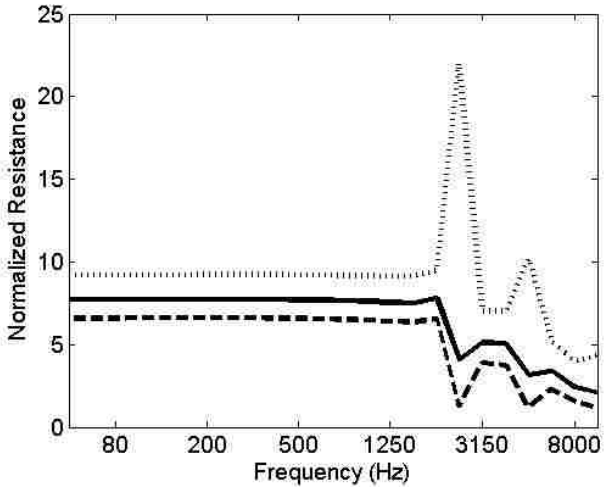

Figure 17. Resistance uncertainty for the optimum lining with the Hexcel® septum in the smaller duct. The operating condition includes a grazing flow Mach number of 0.3 and third octave band levels of 130 dB across the spectrum. [… Upper Bound, ── Nominal, ----- Lower Bound]

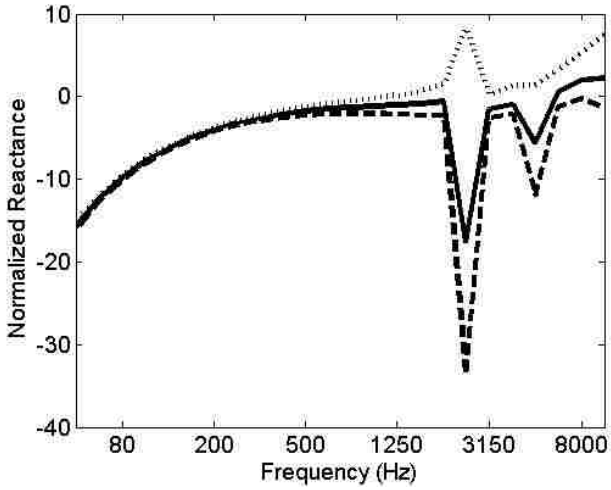

Figure 18. Reactance uncertainty for the optimum lining with the Hexcel® septum in the smaller duct. The operating condition includes a grazing flow Mach number of 0.3 and third octave band levels of 100 dB across the spectrum. [… Upper Bound, ── Nominal, ----- Lower Bound]

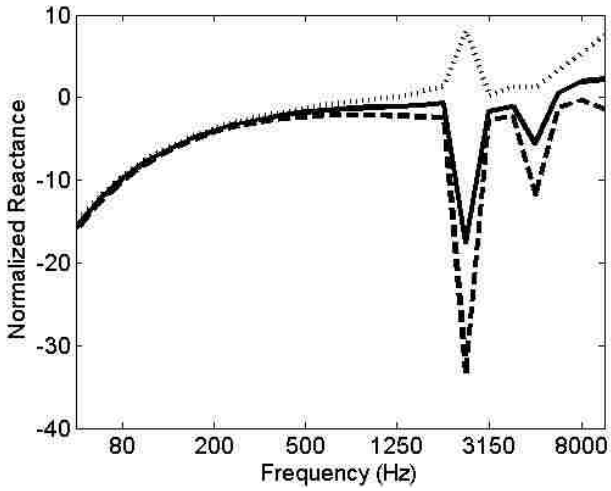

Figure 19. Reactance uncertainty for the optimum lining with the Hexcel® septum in the smaller duct. The operating condition includes a grazing flow Mach number of 0.3 and third octave band levels of 130 dB across the spectrum. [… Upper Bound, ── Nominal, ----- Lower Bound]

In reviewing Fig. 12 through Fig. 19 it can be observed that the laser drilled septum lining was more sensitive to SPL than the Hexcel® septum lining in the smaller

duct; in fact, the Hexcel® septum lining was nearly insensitive to SPL for the cases shown. Not explicitly addressed in these results was the observation that the Hexcel® septum lining was less sensitive to grazing flow Mach number than the laser drilled septum lining. It should be emphasized that the conclusions drawn here were undoubtedly dependent on the lining configuration, and this in turn was dependent on the conditions for which the lining was optimized.

Figure 20 through Fig. 27 represent the same conditions as Fig. 12 through Fig. 19 using the larger duct with the exception of the grazing flow Mach numbers. The conclusions drawn with the smaller duct are relevant here as well, though the details were modified by the different duct geometry and flight conditions. It was clear that even though these cases had an altered duct geometry and flight conditions, a pronounced effect on impedance variation was observed while using the same manufacturing tolerances. This lends credence to the supposition that reasonable manufacturing tolerance limits can have a substantial effect of the modeled resistance and reactance of an optimized lining regardless of the duct and flight conditions for which is was designed. Another observation is that an optimized lining is not robust near the design conditions.

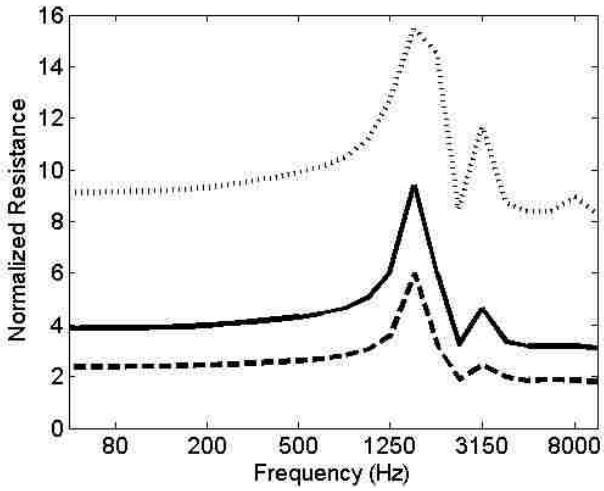

Figure 20. Resistance uncertainty for the optimum lining with the laser drilled septum in the larger duct. The operating condition includes a grazing flow Mach number of 0.4 and third octave band levels of 100 dB across the spectrum. [… Upper Bound, ── Nominal, ----- Lower Bound]

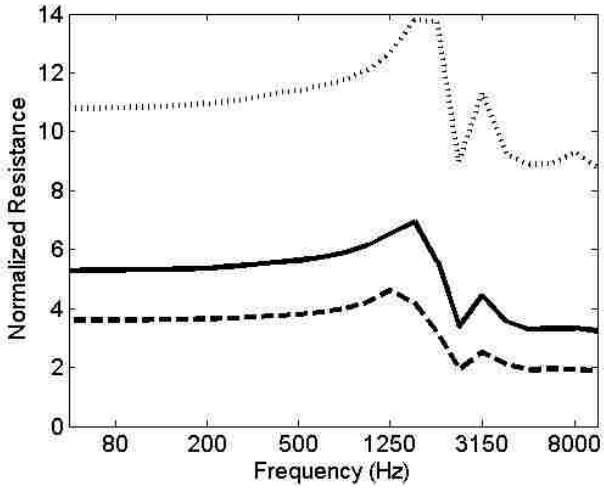

Figure 21. Resistance uncertainty for the optimum lining with the laser drilled septum in the larger duct. The operating condition includes a grazing flow Mach number of 0.4 and third octave band levels of 130 dB across the spectrum. [… Upper Bound, ── Nominal, ----- Lower Bound]

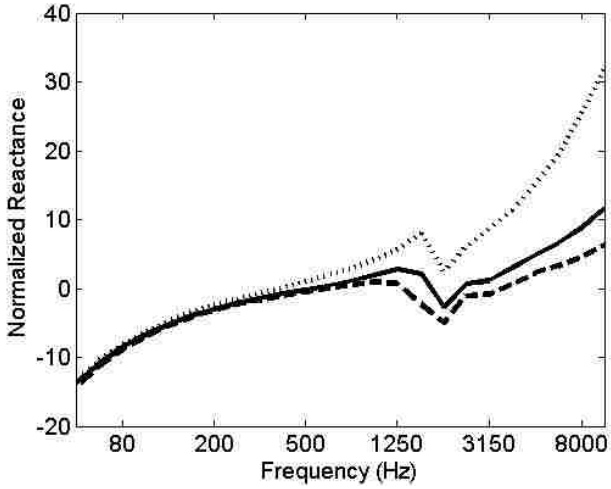

Figure 22. Reactance uncertainty for the optimum lining with the laser drilled septum in the larger duct. The operating condition includes a grazing flow Mach number of 0.4 and third octave band levels of 100 dB across the spectrum. [… Upper Bound, ── Nominal, ----- Lower Bound]

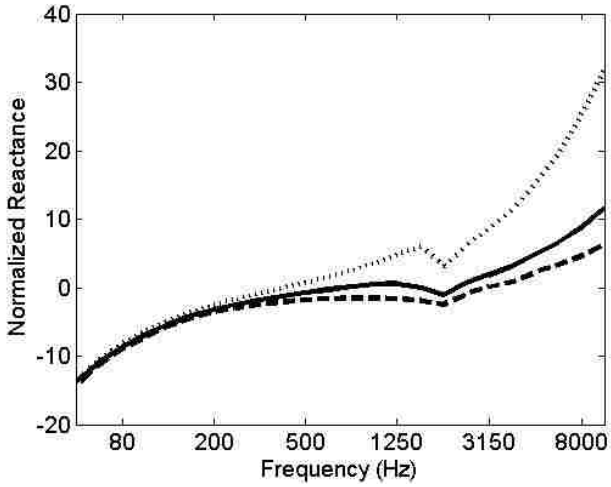

Figure 23. Reactance uncertainty for the optimum lining with the laser drilled septum in the larger duct. The operating condition includes a grazing flow Mach number of 0.4 and third octave band levels of 130 dB across the spectrum. [… Upper Bound, ── Nominal, ----- Lower Bound]

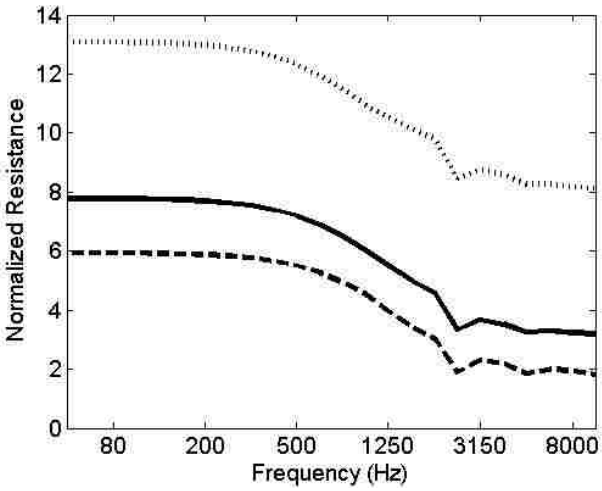

Figure 24. Resistance uncertainty for the optimum lining with the Hexcel® septum in the larger duct. The operating condition includes a grazing flow Mach number of 0.4 and third octave band levels of 100 dB across the spectrum. [… Upper Bound, ── Nominal, ----- Lower Bound]

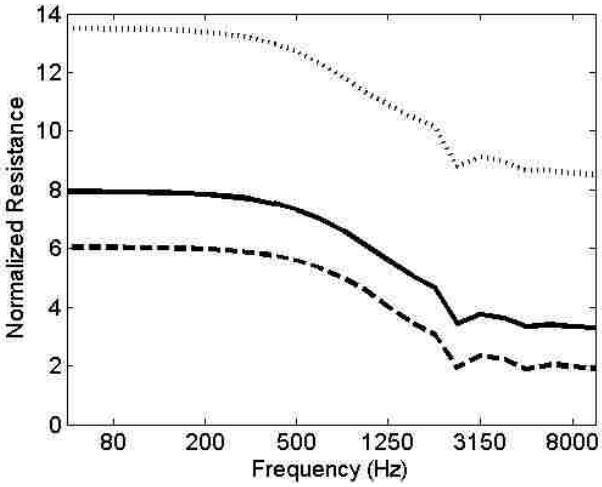

Figure 25. Resistance uncertainty for the optimum lining with the Hexcel® septum in the larger duct. The operating condition includes a grazing flow Mach number of 0.4 and third octave band levels of 130 dB across the spectrum. [… Upper Bound, ── Nominal, ----- Lower Bound]

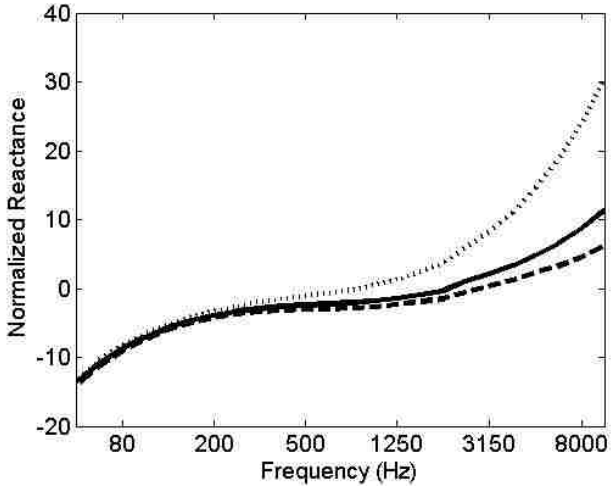

Figure 26. Reactance uncertainty for the optimum lining with the Hexcel® septum in the larger duct. The operating condition includes a grazing flow Mach number of 0.4 and third octave band levels of 100 dB across the spectrum. [… Upper Bound, ── Nominal, ----- Lower Bound]

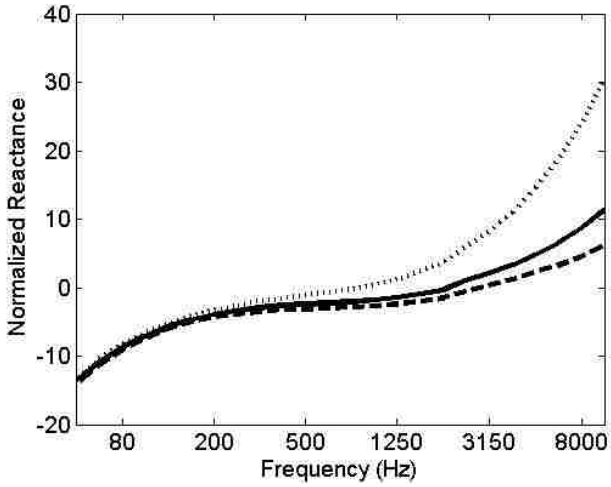

Figure 27. Reactance uncertainty for the optimum lining with the Hexcel® septum in the larger duct. The operating condition includes a grazing flow Mach number of 0.4 and third octave band levels of 130 dB across the spectrum. [… Upper Bound, ── Nominal, ----- Lower Bound]

5.2. Impedance Variation with Sideline and Approach Operating Conditions and Single Parameter Tolerance Variation

When evaluating the cost-benefit of the manufacturing process, it is important to isolate the most problematic portions of the process where possible. Variation of a single geometric or physical parameter at a time provides an indication of the sign and magnitude of the modeled resistance and reactance deviation from nominal at each frequency band center frequency due to tolerance in a single geometric or physical parameter such as face sheet OAR or septum DC flow resistance. Since maintaining a manufacturing tolerance in each type of geometric or physical parameter will have its own associated costs, isolation of single parameter effects is very useful. It is important to note that the cumulative effect of multiple simultaneous parameter variations on impedance is not a summation of the individual parameter variation effects on impedance. Furthermore, the effects on impedance deviation are not strictly positive or negative over all frequency bands. This implies that analysis using single parameter variation is useful in cost-benefit analysis, but it should not be extrapolated to represent cumulative tolerance effects on impedance.

A set of models was evaluated for the optimum lining with the laser drilled septum in the smaller duct. Sideline and approach conditions were investigated as a single parameter was varied in the positive direction by the amount of the manufacturing tolerance. All other values were kept at design values. The same parameter was then varied in the negative direction by the amount of the manufacturing tolerance. This parameter was returned to the design value, and the process was repeated with the next parameter. Once all parameters had been individually varied, the process was repeated for

the lining model with the Hexcel® septum. The impedances were compared as each parameter was varied. The parameter variation that showed the largest impedance deviation from the nominal value was recorded. The results are shown in Table 4. This process was repeated for the optimum design in the larger duct. Those results are shown in Table 5.

Table 4 is segmented for the sideline and approach cases for the optimum design for the smaller duct and in each of these cases into the laser drilled and Hexcel® septum linings. Consider the first line of the table. This indicates that at the sideline condition for the lining model with the laser drilled septum, decreasing the face sheet OAR by the manufacturing tolerance caused a higher resistance than variation of any other single parameter. The design value was 6.1100, and the model that included the variation of face sheet OAR produced a resistance of 9.6399. Comparing this value with the contour plot in Fig. 8, it can be seen that there can be a large attenuation loss due to the tolerance in face sheet OAR. It is clear that manufacturing tolerances can significantly degrade lining attenuation. Table 4 indicates that face sheet OAR was one of the most important parameters on which to maintain a tight manufacturing tolerance for those particular lining designs in that particular manufacturing process. The most significant parameters may vary for different lining configurations where the tolerance is large relative to the nominal parameter value.

Table 4. Largest impedance deviations due to variations in single geometric parameters within manufacturing tolerance limits for the smaller duct with the optimum design.

Sideline					
	Impedance Type	**Parameter**	**Parameter Tolerance Variation**	**Design Impedance Value**	**Model Impedance**
Laser Drilled	Resistance High	Face Sheet OAR	Negative	6.1100	9.6399
	Reactance High	Face Sheet OAR	Negative	-1.2050	1.1607
	Resistance Low	Face Sheet OAR	Positive	6.1100	4.7481
	Reactance Low	Face Sheet OAR	Positive	-1.2050	-2.1509
Hexcel	Resistance High	Face Sheet OAR	Negative	6.1100	7.1679
	Reactance High	Face Sheet OAR	Negative	-1.2048	0.5786
	Resistance Low	Septum Insertion Depth	Positive	6.1100	5.3304
	Reactance Low	Face Sheet OAR	Positive	-1.2048	-1.0202
Approach					
	Impedance Type	**Parameter**	**Parameter Tolerance Variation**	**Design Impedance Value**	**Model Impedance**
Laser Drilled	Resistance High	Face Sheet OAR	Negative	2.7039	4.0709
	Reactance High	Face Sheet OAR	Negative	-0.3845	2.8543
	Resistance Low	Face Sheet OAR	Positive	2.7039	2.1509
	Reactance Low	Septum Insertion Depth	Negative	-0.3845	-1.7894
Hexcel	Resistance High	Face Sheet OAR	Negative	1.1529	3.1448
	Reactance High	Face Sheet OAR	Negative	-0.3846	1.2026
	Resistance Low	Backing Cavity Depth	Negative	1.1529	1.7014
	Reactance Low	Backing Cavity Depth	Negative	-0.3846	-0.9373

Table 5. Largest impedance deviations due to variations in single geometric parameters within manufacturing tolerance limits for the larger duct with the optimum design.

Sideline					
	Impedance Type	**Parameter**	**Parameter Tolerance Variation**	**Design Impedance Value**	**Model Impedance**
Laser Drilled	Resistance High	Face Sheet OAR	Negative	7.7340	18.8583
	Reactance High	Face Sheet OAR	Negative	-0.4455	2.1041
	Resistance Low	Face Sheet OAR	Positive	7.7340	5.0285
	Reactance Low	Face Sheet OAR	Positive	-0.4455	-1.6030
Hexcel	Resistance High	Face Sheet OAR	Negative	7.7340	17.8067
	Reactance High	Face Sheet OAR	Positive	-0.4455	1.8155
	Resistance Low	Face Sheet OAR	Negative	7.7340	5.2751
	Reactance Low	Face Sheet OAR	Positive	-0.4455	-1.5555
Approach					
	Impedance Type	**Parameter**	**Parameter Tolerance Variation**	**Design Impedance Value**	**Model Impedance**
Laser Drilled	Resistance High	Face Sheet OAR	Negative	3.1370	7.7771
	Reactance High	Face Sheet OAR	Positive	-0.3088	3.4983
	Resistance Low	Face Sheet OAR	Negative	3.1370	2.2816
	Reactance Low	Face Sheet OAR	Positive	-0.3088	-1.2684
Hexcel	Resistance High	Face Sheet OAR	Negative	3.1370	7.6440
	Reactance High	Face Sheet OAR	Positive	-0.3088	3.3854
	Resistance Low	Face Sheet OAR	Negative	3.1370	2.2768
	Reactance Low	Face Sheet OAR	Positive	-0.3088	-1.2768

Table 5 is segmented for the sideline and approach cases for the optimum design in the larger duct and in each of these cases into the laser drilled and Hexcel® septum

linings. For this duct tolerance in face sheet OAR contributed most significantly to impedance variation in each case. This was different from the smaller duct and most likely due to the relative levels of the design parameters and the associated tolerance. This indicates the importance of evaluating each unique lining design and manufacturing process.

5.3. Attenuation Variation Due to Manufacturing Tolerance

A search of the uncertainty of realized impedance related to all systematically varied combinations of manufacturing tolerance limits was also carried out for the approach and sideline operating conditions in each duct with each lining. All possible combinations of each parameter at its design value, the design value plus the associated tolerance, and the design value minus the associated tolerance were evaluated for the effect on the impedance of the resulting lining. The impedance at the optimum lining design with no manufacturing tolerances considered is referred to as the nominal impedance. The maximum deviations, above and below nominal, of resistance and reactance for the two linings at the one-third octave band center frequencies were recorded. Results for the extreme variations in resistance and reactance were of a similar magnitude to those displayed in Fig. 12 through Fig. 27. An additional step was taken here. Attenuation variations corresponding to cases of the extremes of the impedance variation were found using the propagation code. The models used to generate these attenuations are not based on the lining model. They are instead based on the impedance found in the parameter variation studies. The lining model used in the determination of

attenuation included the non-linear effect of source SPL spectrum on impedance but not the effect of variation of SPL locally on the lining.

The results for attenuation can be summarized as shown in Figs. 28 and 29. Each figure is divided into clusters applicable to approach and sideline conditions for the laser drilled and Hexcel® septum linings. For the sideline case, attenuation is shown for the targeted blade passage frequency, and for the approach case, attenuation is shown for the targeted twice blade passage frequency. Each cluster has eight cases of extremes of resistance and reactance variations as well as the nominal case. In the optimum design cases, attenuation for the nominal laser drilled septum and Hexcel® septum linings was the same at each flight condition. This was because the lining parameters could be found to exactly produce the optimum impedance.

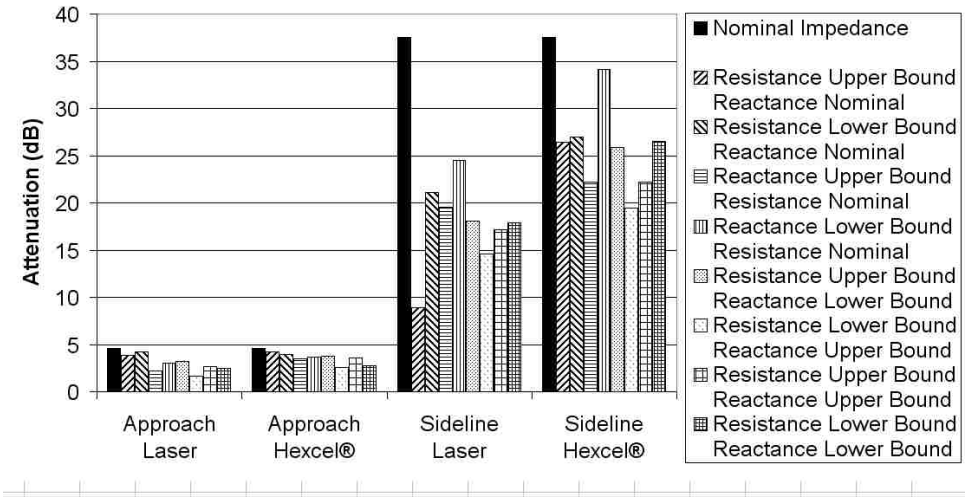

Figure 28. Variation in propagation attenuation due to manufacturing tolerance in the smaller duct for the optimum design.

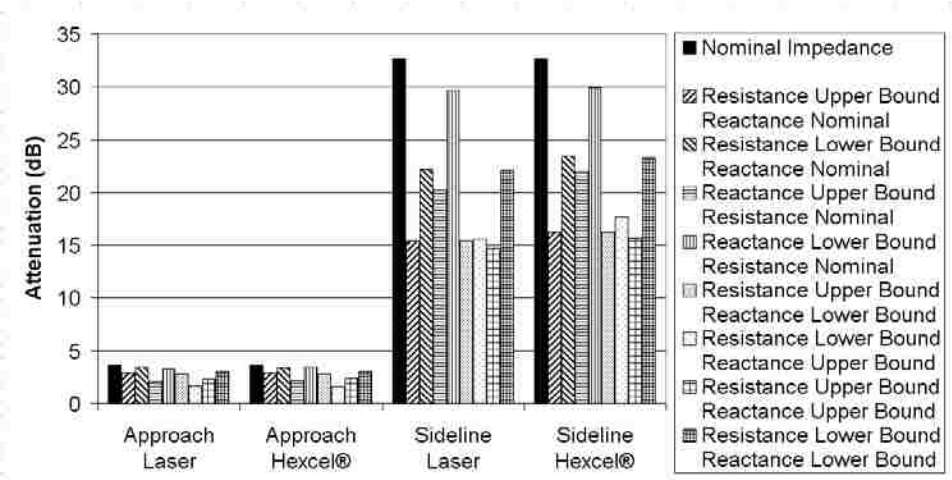

Figure 29. Variation in propagation attenuation due to manufacturing tolerance in the larger duct for the optimum design.

Two groupings of extreme variations of impedance are shown. In one grouping only resistance or only reactance was allowed to assume its extreme value (the remaining component of impedance remained nominal). In the second grouping four combinations of simultaneous extreme variations of resistance and reactance were used.

The most obvious result was that attenuation at blade passage frequency at the sideline condition potentially could be substantially reduced due manufacturing tolerances. This was consistent with the impedance maps that show that the optimum condition was sharply tuned and that sensitivity of attenuation to impedance variation was high.

For the sideline condition in the optimum smaller duct with the lining that has the laser drilled septum, the impedance condition that generated the lowest attenuation was that which allowed the resistance to stray to its upper value with the nominal reactance

value. Table 4 indicates through single parameter variation analysis that face sheet OAR straying toward the lower manufacturing tolerance level was the most significant contributor to the higher resistance in this lining. In the case of the lining with the Hexcel® septum, a combination of the lower tolerance in resistance and higher tolerance in reactance led to the lowest attenuation. The impedance tolerances that led to the lowered attenuation were a consequence of the tolerance in the septum insertion depth and the face sheet OAR. The cost of tightening manufacturing tolerances in these parameters should be weighed against the potential loss in attenuation.

In the approach case in the optimum smaller duct, attenuation was slightly less sensitive to manufacturing tolerances for the Hexcel® septum than for the laser drilled septum. In the approach case for both linings, the impedance variations that led to the largest reduction in attenuation over the nominal case were those that allowed the resistance to stray to lower values and the reactance to stray to higher values. The chief contributors to generating these impedance conditions were a variation in the face sheet OAR and backing cavity depth.

In the case of the larger duct, the sideline condition also indicated higher attenuation than the approach condition. The sideline cases, as compared to the smaller duct, indicated a similar sensitivity to variation in impedance. In both the sideline and approach conditions, manufacturing tolerance can lead to a marked reduction in attenuation. Table 5 indicates that face sheet OAR contributes most significantly to the reduction in attenuation.

6. ATTENUATION ANALYSIS WITH LOCAL LINING IMPEDANCE DEPENDANCE ON SPL

Attenuation predictions to this point have been obtained with a lining model in which impedance is dependent on the SPL spectrum of the source. In this section a variant of the propagation code was used that has a lining model imbedded so that based on physical and geometric parameters impedance is calculated at every point on the lining. Impedance is additionally dependent on local grazing flow Mach number and local SPL spectrum. Grazing flow Mach number is fixed by the duct mean flow, however the local SPL spectrum depends on the duct acoustic field. Dependence on SPL therefore enters in a non-linear way. An iterative approach is used in which the spectrum everywhere on the lining is initially assumed to be the source spectrum. The acoustic field is calculated locally on the lining, and the local impedance is recalculated based on the adjusted SPL spectrum. This process proceeds for several iterations until convergence is obtained, yielding local lining impedance consistent with the local acoustic field. It is assumed that the lining is only effective for the one-third octave band containing the targeted frequency. This effect of local variation in SPL spectrum is heavily dependent on the nature of the source spectrum. If the target one-third octave band level dominates the spectrum, then this band accounts for most of the non-linear behavior of the lining and reduction in this band level has a significant effect on the spectrum particle velocity that influences impedance. If the targeted band is nearly the same as adjacent bands little non-linear effect on impedance will result, because spectrum particle velocity will be dominated by the broad band levels.

6.1. Effect of Local Variation of Impedance Due to Local Variation of Grazing Flow Mach Number and SPL Spectrum

In this section an assessment is made of the importance of local variation of impedance on attenuation for nominal values of lining physical and geometric parameters for each duct. In the approach case the one-third octave band spectrum was predominately broadband, as shown in Figs. 5 and 7. The band containing the target frequency did not dominate the spectrum. With the assumption that the impedance affects only the target band, it was expected that little effect of local variation of the SPL spectrum would be seen. In the case of the sideline operating condition the source spectrum shown in Figs. 4 and 6 was dominated by at least 10 dB by the band containing the target frequency. In this case it was expected that a significant effect of local variation in SPL would occur. Figures 30 and 31 compare attenuation between cases where the lining impedance depended only on the source SPL spectrum and where it depended on the local SPL spectrum. This was done for nominal lining physical and geometric parameters. The approach operating condition and the sideline operating condition are shown. For each operating condition, attenuations for the laser drilled and Hexcel® septum models are shown. For both linings in both ducts, the effect of local variation of SPL on impedance had little effect on attenuation at the approach condition. At the sideline condition attenuation was high, but slightly different for the laser drilled septum and the Hexcel® septum. In Figs. 28 and 29 nominal attenuations were predicted using specified constant impedance, and laser drilled and Hexcel® septum models yielded the same impedance. In the present case local source SPL spectrum and grazing flow Mach number influenced local lining impedance, and this accounted for slightly different lining performance. When the local SPL spectrum was used in the lining model, attenuation at

the sideline condition was reduced approximately 4 dB for the laser drilled septum and decreased by approximately 0.4 dB for the Hexcel® septum in the smaller duct. The larger duct exhibited an increase in attenuation for both linings at the sideline condition. The approach cases in both ducts showed almost no variation in attenuation. This supported the proposition that the effect of local SPL on attenuation is minimal when the spectrum has broadband character and that a significant effect on attenuation can, but does not necessarily, occur when the target frequency of the lining dominates the spectrum.

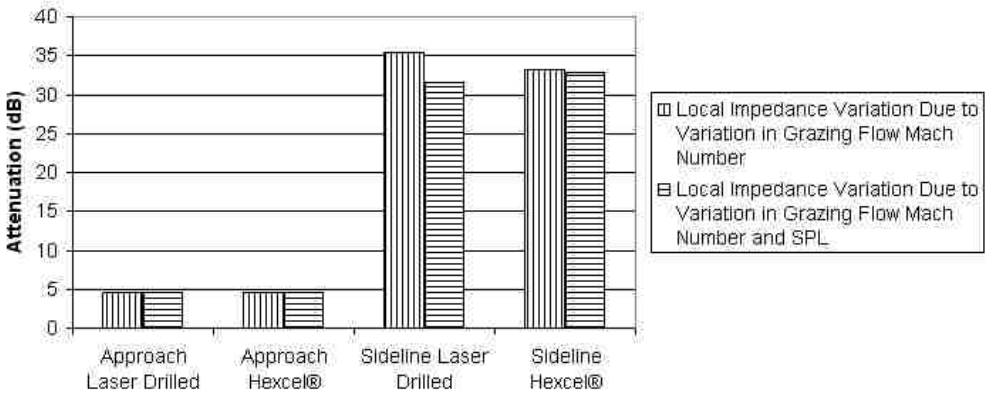

Figure 30. Effect of local SPL spectrum variation on attenuation in the smaller duct for the optimum design.

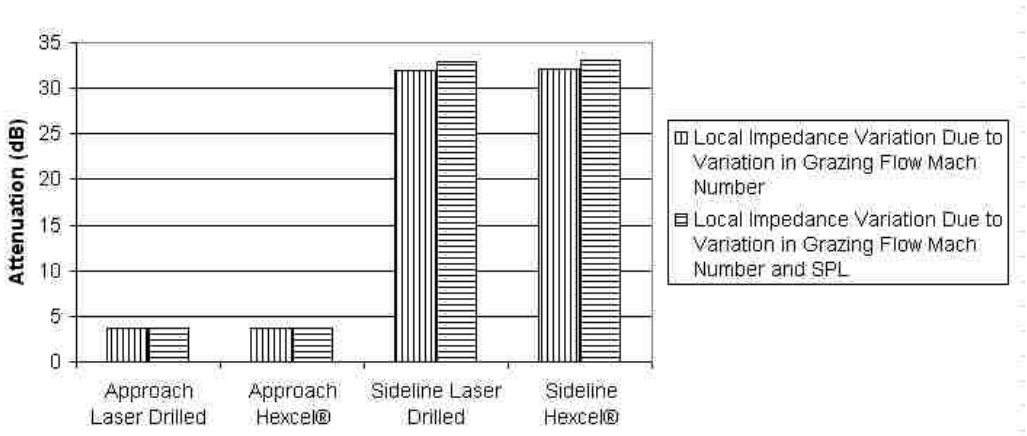

Figure 31. Effect of local SPL spectrum variation on attenuation in the larger duct for the optimum design.

6.2. Attenuation Variation Due to Manufacturing Tolerance with Local SPL Spectrum Variation

In this section the effect of local variation of SPL spectrum on lining impedance, and therefore on attenuation, is extended to include manufacturing tolerances. A systematic search for impedance variation was carried out for the sideline and approach operating conditions for both ducts and multiple values for geometric and physical parameter values varied within manufacturing tolerances. A nominal design value, an upper tolerance bound, and a lower tolerance bound for each of the eight physical parameters yields all possible physical models that could result from a single lining design. The impedance was evaluated for each resulting lining model identifying the parameter combination that yielded the largest deviation in resistance and reactance from the nominal. This was done for each flight condition in each duct.

The models that led to the largest deviations in resistance and reactance were used as the input for the summary plots shown in Figs. 32 and 33. The “nominal values”

condition used a lining design that did not account for manufacturing tolerances. As an example of the effects of impedance variation on attenuation, consider the case in Fig. 32 labeled Resistance Upper Bound. For this case, the model whose parameter combinations led to the largest deviation in resistance in the positive direction was used to define the lining parameters. Reactance did not remain at the nominal value, but it was also not the upper or lower limiting case. In the sideline and approach cases the effects of the manufacturing tolerance produced a potentially significant reduction in attenuation levels.

Consider the sideline case with the lining with the laser drilled septum for the smaller duct. Figure 32 indicates that the impedance conditions that generated the lowest attenuations were those that allowed the resistance or reactance to stray to higher values. Table 4 indicates through single parameter variation analysis that face sheet OAR straying towards the lower manufacturing tolerance level was the most significant contributor to these impedance conditions. Therefore, the cost of tightening that manufacturing tolerance should be weighed against the potential loss in attenuation if it is not. In the case of the lining with the Hexcel® septum, face sheet OAR straying toward its lower bound was the chief contributor to the lowest attenuation.

Considering the approach cases for each lining in the smaller duct, face sheet OAR and backing cavity depth straying toward the lower manufacturing tolerance level contributed to the lowest attenuation for the lining with the laser drilled septum and Hexcel® septum respectively. This reinforced the previous finding that, in a cost-benefit

analysis of the manufacturing process for the smaller duct, the manufacturing tolerance of the face sheet OAR was critical.

In the case with the larger duct, tolerance in face sheet OAR was again the most significant contributor to loss in attenuation. Significant potential changes in attenuation reinforced the sensitivity of attenuation to face sheet OAR for the larger duct in this manufacturing process.

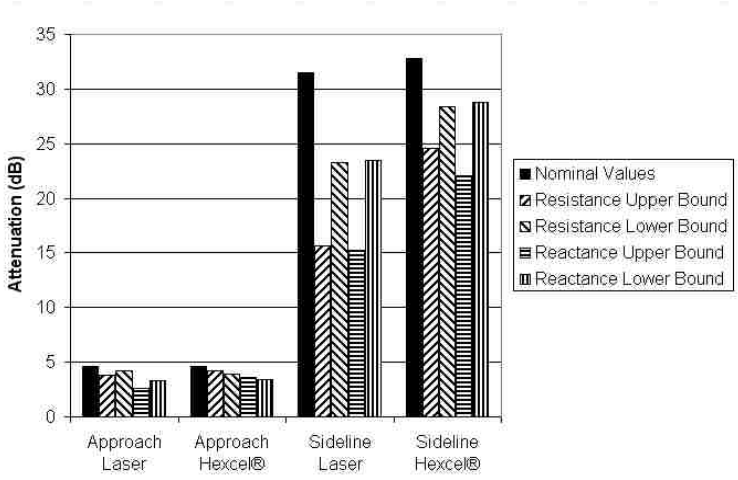

Figure 32. Variation in propagation attenuation due to manufacturing tolerance and local impedance variation in the smaller duct for the optimum design.

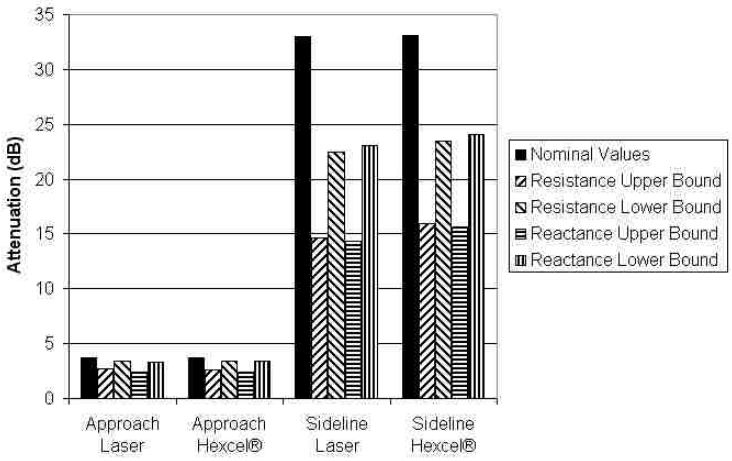

Figure 33. Variation in propagation attenuation due to manufacturing tolerance and local impedance variation in the larger duct for the optimum design.

7. SUB-OPTIMUM LINING DESIGN

The impedance of a two DOF lining can be extremely sensitive to physical and geometric properties near the optimum values. The manufacturing process for any lining imposes physical constraints on the range of geometric and physical properties that can be achieved. For this reason it may be necessary to settle for a lining that does not have the optimum impedance for maximum attenuation. But, the lining must still have a minimum attenuation level including manufacturing process tolerance to be acceptable. Two linings were designed for each duct that came as close to the optimum impedance as possible while adhering to prescribed manufacturing process limits. The same duct geometries and flight conditions used in the optimized design were used for this study.

7.1. Physical and Geometric Parameters for Each Sub-Optimum Lining

The search space for the lining parameters was limited to manufacturable values. This guaranteed a realizable lining but did not guarantee acceptable attenuation levels. The attenuation analysis must still be performed. The physical and geometric parameters for each lining were allowed to vary within prescribed ranges chosen to facilitate manufacturability. These ranges can be seen in Table 6.

Table 6. Sub-optimum design parameter values and ranges.

Design parameter ranges	Pin mat face sheet/laser drilled buried septum		Pin mat face sheet/Hexcel® septum	
Face sheet OAR	0.035 - 0.25		0.035 - 0.25	
Face sheet thickness, in (cm)	0.04	(0.102)	0.04	(0.102)
Face sheet hole diameter, in (cm)	0.043	(0.109)	0.043	(0.109)
Septum insertion depth, in (cm)	0.25 - 2.5	(0.635 - 6.35)	0.25 - 2.5	(0.635 - 6.35)
Septum OAR	0.035 - 0.25		N/A	
Septum thickness, in (cm)	0.03	(0.076)	N/A	
Septum hole diameter, in (cm)	0.008	(0.020)	N/A	
Septum backing depth, in (cm)	0.25 - 2.5	(0.635 - 6.35)	0.25 - 2.5	(0.635 - 6.35)
Septum non-linearity factor	N/A		1.6	
Cross frequency, Hz	N/A		10,000	
Septum DC flow resistance, cgs Rayls	N/A		80 - 200	

The optimum impedances could not be matched with these physical restrictions. Due to the high levels of potential attenuation that can be achieved at the sideline condition, preference was given to matching the approach impedance condition. The impedance at the sideline condition was allowed more variation. The closest match for the lining with the laser drilled septum in the smaller duct yielded an impedance of $Z = 1.72 + 0.74i$ for the sideline condition and $Z = 2.70 - 0.38i$ for the approach condition. The closest match for the lining with the Hexcel® septum in the smaller duct yielded an impedance of $Z = 4.09 + 1.31i$ for the sideline condition and $Z = 2.70 - 0.38i$ for the approach condition. The closest match for the lining with the laser drilled septum in the larger duct yielded an impedance of $Z = 3.82 + 0.31i$ for the sideline condition and $Z = 3.14 - 0.31i$ for the approach condition. The closest match for the lining with the Hexcel® septum in the larger duct yielded an impedance of $Z = 4.45 - 0.49i$ for the

sideline condition and $Z = 3.14 - 0.31i$ for the approach condition. The lining parameters are shown in Table 7 and Table 8.

The sensitivity of attenuation to parameter variation was high near the optimum impedance. The impedances of the sub-optimum linings were close enough to the optimum that the sensitivity was still high. The impedance maps shown in Fig. 34 through Fig. 41 illustrate the potential loss in attenuation for the sub-optimum designs. The impedance maps are centered on the lining impedance.

Table 7. Sub-optimum designs for the smaller duct linings.

Sub-Optimum Design				
Design parameter	Smaller duct - Pin mat face sheet/laser drilled buried septum		Smaller duct - Pin mat face sheet/Hexcel® septum	
Face sheet OAR	0.1059		0.0415	
Face sheet thickness, in (cm)	0.0400	(0.1016)	0.0400	(0.1016)
Face sheet hole diameter, in (cm)	0.0430	(0.1092)	0.0430	(0.1092)
Septum insertion depth, in (cm)	0.5412	(1.3746)	0.2502	(0.6355)
Septum OAR	0.0598		N/A	
Septum thickness, in (cm)	0.0300	(0.0762)	N/A	
Septum hole diameter, in (cm)	0.0080	(0.0203)	N/A	
Septum backing depth, in (cm)	0.5780	(1.4681)	1.1673	(2.9649)
Septum non-linearity factor	N/A		1.6	
Cross frequency, Hz	N/A		10000	
Septum DC flow resistance, cgs Rayls	N/A		80.5	

Table 8. Sub-optimum designs for the larger duct linings.

Sub-Optimum Design				
Design parameter	Larger duct - Pin mat face sheet/laser drilled buried septum		Larger duct - Pin mat face sheet/Hexcel® septum	
Face sheet OAR	0.0350		0.0350	
Face sheet thickness, in (cm)	0.0400	(0.1016)	0.0400	(0.1016)
Face sheet hole diameter, in (cm)	0.0430	(0.1092)	0.0430	(0.1092)
Septum insertion depth, in (cm)	0.8568	(2.1763)	0.3929	(0.9980)
Septum OAR	0.035		N/A	
Septum thickness, in (cm)	0.0300	(0.0762)	N/A	
Septum hole diameter, in (cm)	0.0080	(0.0203)	N/A	
Septum backing depth, in (cm)	1.5771	(4.0058)	2.2931	(5.8245)
Septum non-linearity factor	N/A		1.6	
Cross frequency, Hz	N/A		10000	
Septum DC flow resistance, cgs Rayls	N/A		139.55	

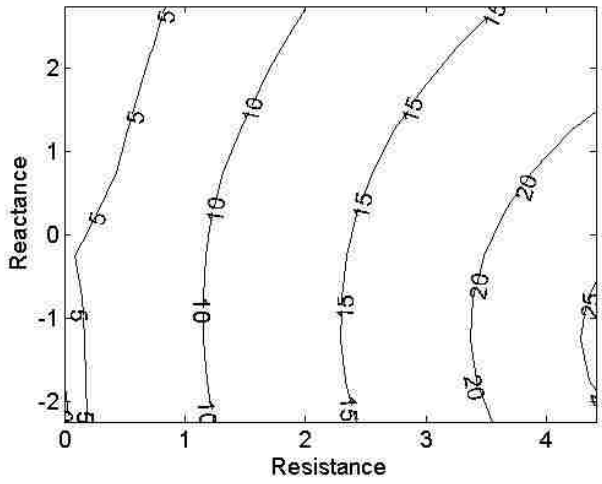

Figure 34. Contour plot of attenuation sensitivity to impedance variation for the sub-optimal smaller duct sideline condition and laser drilled septum.

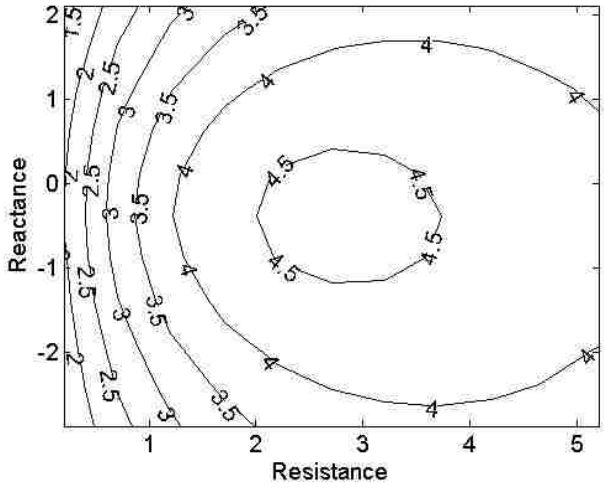

Figure 35. Contour plot of attenuation sensitivity to impedance variation for the sub-optimal smaller duct approach condition and laser drilled septum.

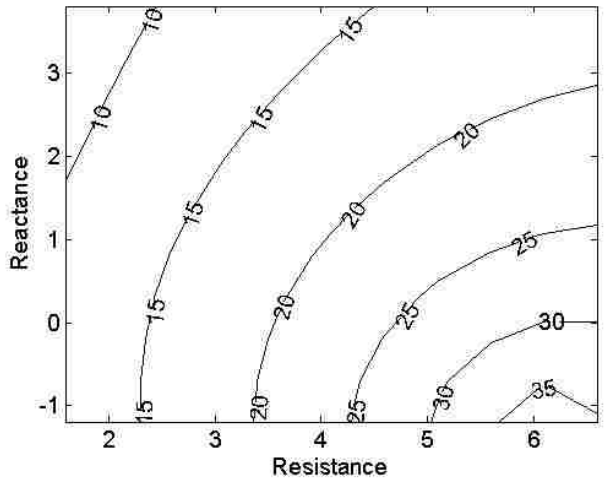

Figure 36. Contour plot of attenuation sensitivity to impedance variation for the sub-optimal smaller duct sideline condition and Hexcel® septum.

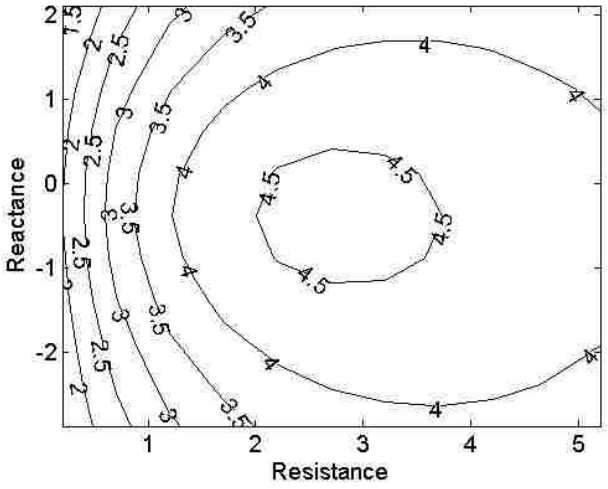

Figure 37. Contour plot of attenuation sensitivity to impedance variation for the sub-optimal smaller duct approach condition and Hexcel® septum.

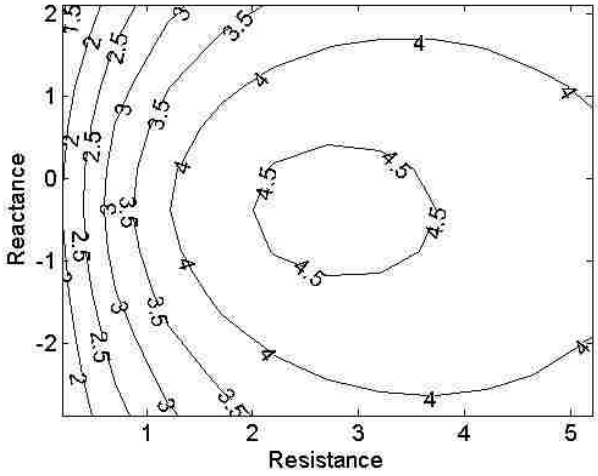

Figure 38. Contour plot of attenuation sensitivity to impedance variation for the sub-optimal larger duct sideline condition and laser drilled septum.

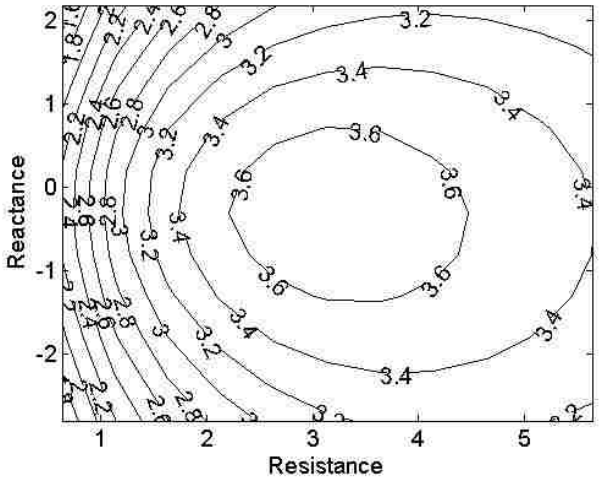

Figure 39. Contour plot of attenuation sensitivity to impedance variation for the sub-optimal larger duct approach condition and laser drilled septum.

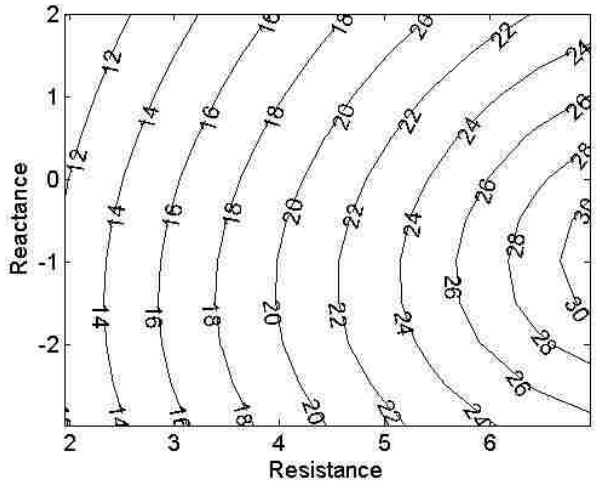

Figure 40. Contour plot of attenuation sensitivity to impedance variation for the sub-optimal larger duct sideline condition and Hexcel® septum.

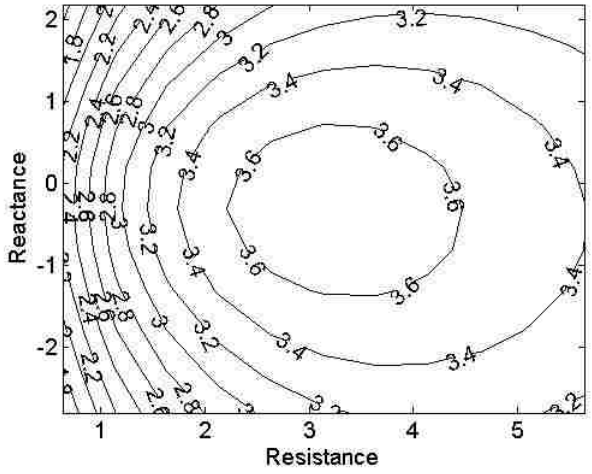

Figure 41. Contour plot of attenuation sensitivity to impedance variation for the sub-optimal larger duct approach condition and Hexcel® septum.

7.2. Impedance Variation with a Broad Range of Operating Conditions and Tolerance Combinations for the Sub-Optimum Linings

The same numerical experiments described in Section 7.1. were conducted using the sub-optimum lining designs to determine impedance variation. The first experiment varying both parameter values and flight condition produced results similar to the optimum data. One important difference was that the frequencies where the impedance variation was most significant has shifted from the optimum data. This can be seen in Fig. 42 through Fig. 57 and is expected with a sub-optimum design.

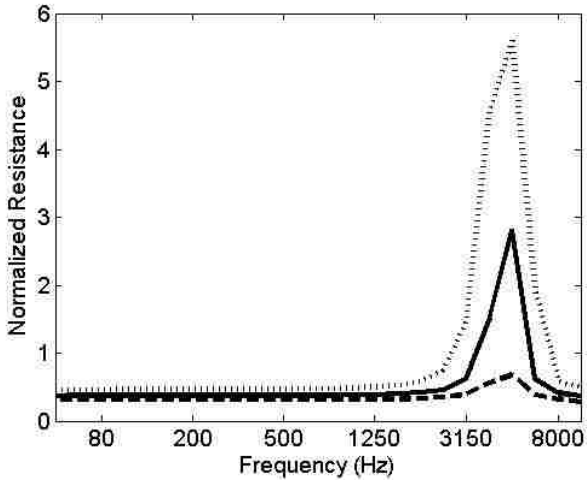

Figure 42. Resistance uncertainty for the sub-optimum lining with the laser drilled septum in the smaller duct. The operating condition includes a grazing flow Mach number of 0.3 and third octave band levels of 100 dB across the spectrum. [… Upper Bound, ── Nominal, ----- Lower Bound]

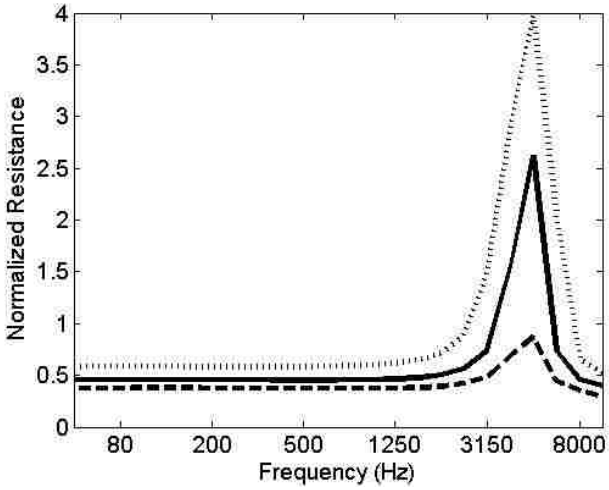

Figure 43. Resistance uncertainty for the sub-optimum lining with the laser drilled septum in the smaller duct. The operating condition includes a grazing flow Mach number of 0.3 and third octave band levels of 130 dB across the spectrum. [… Upper Bound, ── Nominal, ----- Lower Bound]

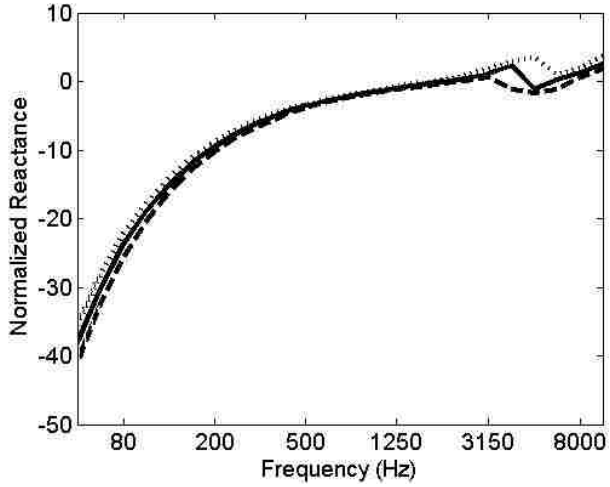

Figure 44. Reactance uncertainty for the sub-optimum lining with the laser drilled septum in the smaller duct. The operating condition includes a grazing flow Mach number of 0.3 and third octave band levels of 100 dB across the spectrum. [… Upper Bound, ── Nominal, ----- Lower Bound]

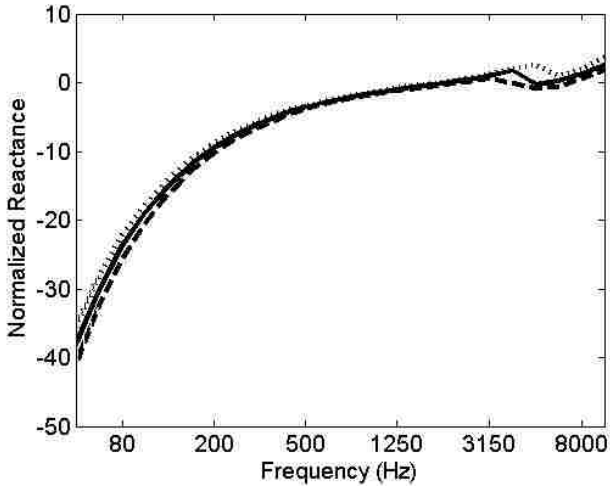

Figure 45. Reactance uncertainty for the sub-optimum lining with the laser drilled septum in the smaller duct. The operating condition includes a grazing flow Mach number of 0.3 and third octave band levels of 130 dB across the spectrum. [… Upper Bound, ── Nominal, ----- Lower Bound]

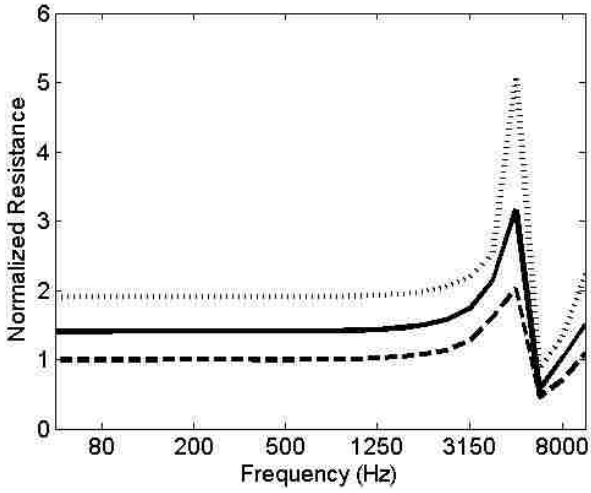

Figure 46. Resistance uncertainty for the sub-optimum lining with the Hexcel® septum in the smaller duct. The operating condition includes a grazing flow Mach number of 0.3 and third octave band levels of 100 dB across the spectrum. [… Upper Bound, ── Nominal, ----- Lower Bound]

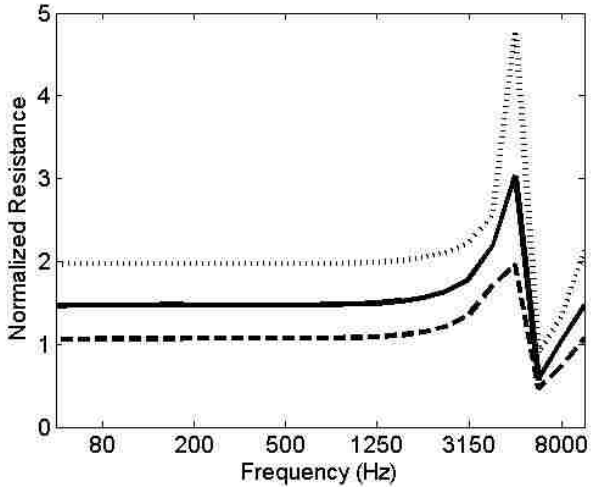

Figure 47. Resistance uncertainty for the sub-optimum lining with the Hexcel® septum in the smaller duct. The operating condition includes a grazing flow Mach number of 0.3 and third octave band levels of 130 dB across the spectrum. [… Upper Bound, ── Nominal, ----- Lower Bound]

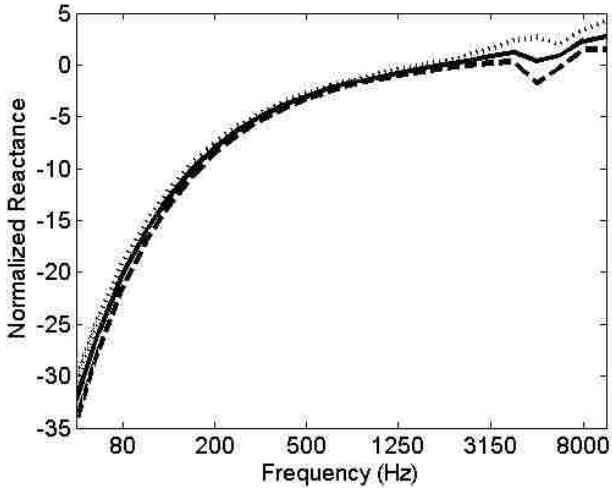

Figure 48. Reactance uncertainty for the sub-optimum lining with the Hexcel® septum in the smaller duct. The operating condition includes a grazing flow Mach number of 0.3 and third octave band levels of 100 dB across the spectrum. [… Upper Bound, ── Nominal, ----- Lower Bound]

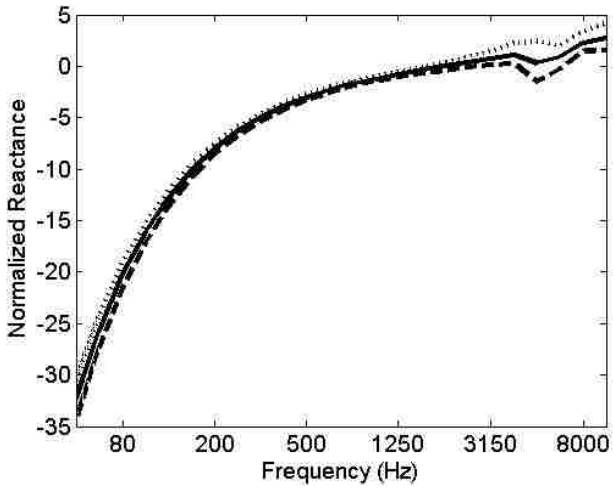

Figure 49. Reactance uncertainty for the sub-optimum lining with the Hexcel® septum in the smaller duct. The operating condition includes a grazing flow Mach number of 0.3 and third octave band levels of 130 dB across the spectrum. [… Upper Bound, ── Nominal, ----- Lower Bound]

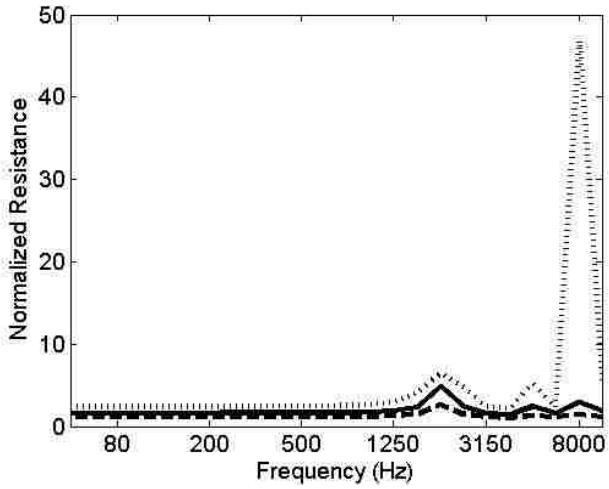

Figure 50. Resistance uncertainty for the sub-optimum lining with the laser drilled septum in the larger duct. The operating condition includes a grazing flow Mach number of 0.4 and third octave band levels of 100 dB across the spectrum. [… Upper Bound, ── Nominal, ----- Lower Bound]

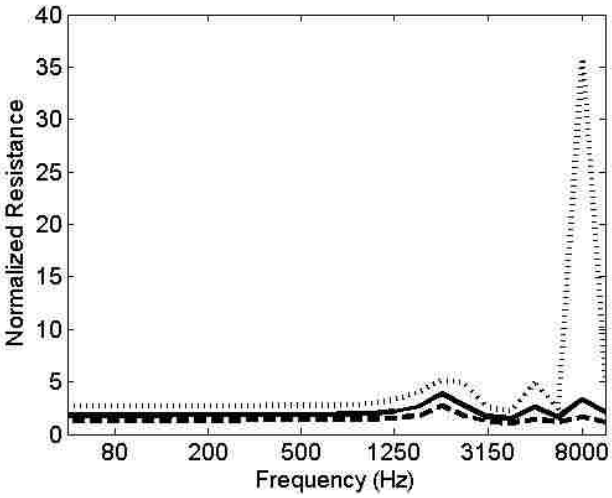

Figure 51. Resistance uncertainty for the sub-optimum lining with the laser drilled septum in the larger duct. The operating condition includes a grazing flow Mach number of 0.4 and third octave band levels of 130 dB across the spectrum. [… Upper Bound, ── Nominal, ----- Lower Bound]

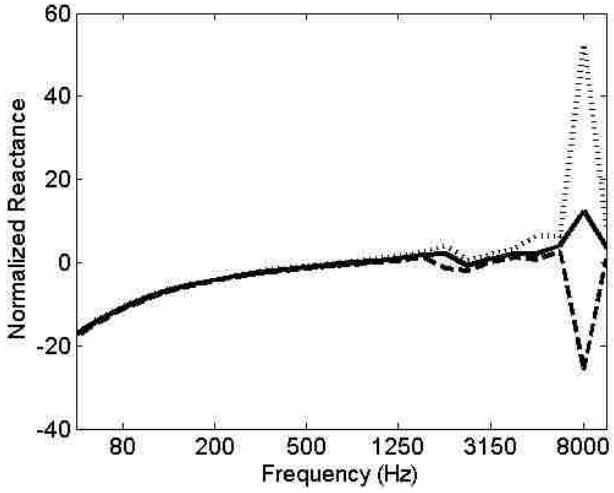

Figure 52. Reactance uncertainty for the sub-optimum lining with the laser drilled septum in the larger duct. The operating condition includes a grazing flow Mach number of 0.4 and third octave band levels of 100 dB across the spectrum. [… Upper Bound, ── Nominal, ----- Lower Bound]

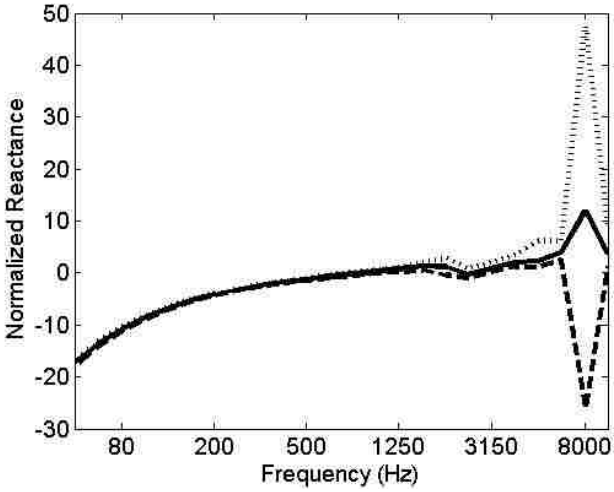

Figure 53. Reactance uncertainty for the sub-optimum lining with the laser drilled septum in the larger duct. The operating condition includes a grazing flow Mach number of 0.4 and third octave band levels of 130 dB across the spectrum. [… Upper Bound, ── Nominal, ----- Lower Bound]

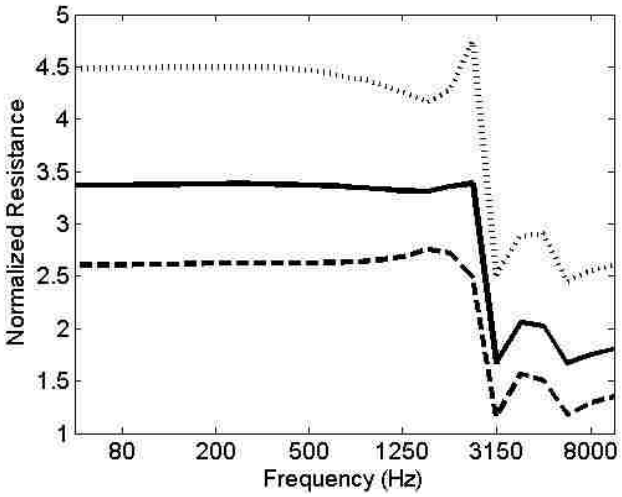

Figure 54. Resistance uncertainty for the sub-optimum lining with the Hexcel® septum in the larger duct. The operating condition includes a grazing flow Mach number of 0.4 and third octave band levels of 100 dB across the spectrum. [… Upper Bound, ── Nominal, ----- Lower Bound]

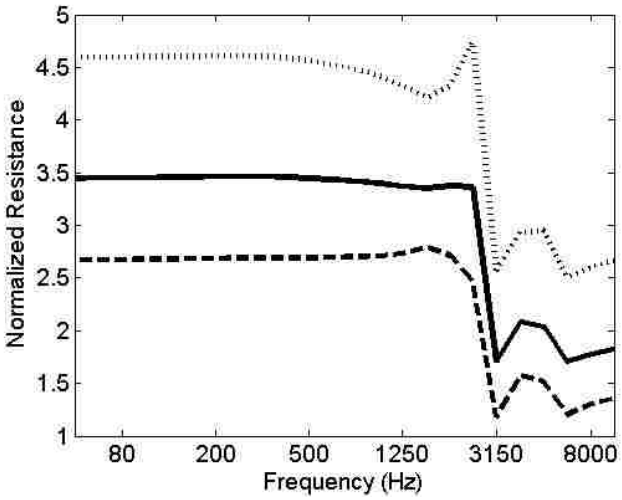

Figure 55. Resistance uncertainty for the sub-optimum lining with the Hexcel® septum in the larger duct. The operating condition includes a grazing flow Mach number of 0.4 and third octave band levels of 130 dB across the spectrum. [… Upper Bound, ── Nominal, ----- Lower Bound]

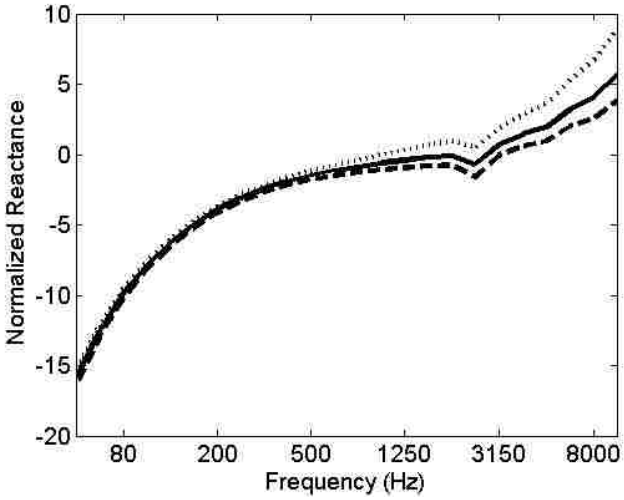

Figure 56. Reactance uncertainty for the sub-optimum lining with the Hexcel® septum in the larger duct. The operating condition includes a grazing flow Mach number of 0.4 and third octave band levels of 100 dB across the spectrum. [… Upper Bound, ── Nominal, ----- Lower Bound]

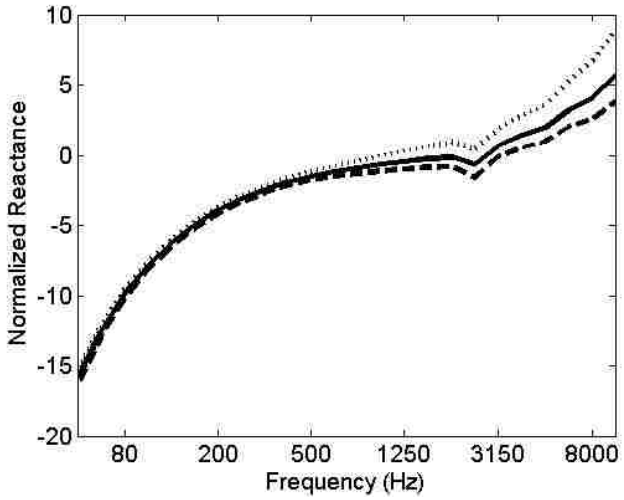

Figure 57. Reactance uncertainty for the sub-optimum lining with the Hexcel® septum in the larger duct. The operating condition includes a grazing flow Mach number of 0.4 and third octave band levels of 130 dB across the spectrum. [… Upper Bound, ── Nominal, ----- Lower Bound]

7.3. Impedance Variation with Sideline and Approach Operating Conditions and Individual Tolerance Variation for the Sub-Optimum Linings

When evaluating a manufacturing process for a sub-optimal lining design, it is even more critical to identify specific parameters that lead to loss of attenuation and to quantify potential loss of attenuation. A single parameter variation study was conducted as described in Section 7.2. Though the duct geometry was the same as the optimum case, vast differences were seen in the single parameter variation results. The impedance ranges were lower, but Fig. 34 through Fig. 41 indicate that these ranges were still significant. The results also indicated that several parameters were responsible for the various impedance extremes. This demonstrated the need to consider each lining design/manufacturing process combination individually when evaluating the manufacturing process. The results can be seen in Table 9 and Table 10.

Table 9. Largest impedance deviations due to variations in single geometric parameters within manufacturing tolerance limits for the smaller duct with the sub-optimum design.

Sideline					
	Impedance Type	**Parameter**	**Parameter Tolerance Variation**	**Design Impedance Value**	**Model Impedance**
Laser Drilled	Resistance High	Backing Cavity Depth	Positive	1.7165	1.8091
	Reactance High	Septum OAR	Positive	0.7356	1.1607
	Resistance Low	Septum OAR	Positive	1.7165	1.4271
	Reactance Low	Septum OAR	Negative	0.7356	0.3638
Hexcel	Resistance High	Face Sheet OAR	Negative	4.0938	4.4034
	Reactance High	Face Sheet OAR	Negative	1.3063	2.1230
	Resistance Low	Face Sheet OAR	Positive	4.0938	3.3133
	Reactance Low	DC Flow Resistance	Positive	1.3063	1.0846
Approach					
	Impedance Type	**Parameter**	**Parameter Tolerance Variation**	**Design Impedance Value**	**Model Impedance**
Laser Drilled	Resistance High	Septum OAR	Positive	2.7039	3.2403
	Reactance High	Septum OAR	Positive	-0.3847	0.7555
	Resistance Low	Septum OAR	Negative	2.7039	0.9804
	Reactance Low	Backing Cavity Depth	Positive	-0.3847	-0.4898
Hexcel	Resistance High	Backing Cavity Depth	Negative	2.7039	2.5584
	Reactance High	Face Sheet OAR	Negative	-0.3846	0.7097
	Resistance Low	Backing Cavity Depth	Positive	2.7039	1.0117
	Reactance Low	Face Sheet OAR	Positive	-0.3846	-0.5107

Table 10. Largest impedance deviations due to variations in single geometric parameters within manufacturing tolerance limits for the larger duct with the sub-optimum design.

Sideline					
	Impedance Type	**Parameter**	**Parameter Tolerance Variation**	**Design Impedance Value**	**Model Impedance**
Laser Drilled	Resistance High	Face Sheet OAR	Negative	3.8207	5.2898
	Reactance High	Face Sheet OAR	Negative	0.3057	0.8188
	Resistance Low	Face Sheet OAR	Positive	3.8207	3.1080
	Reactance Low	Face Sheet OAR	Negative	0.3057	-0.0251
Hexcel	Resistance High	Face Sheet OAR	Negative	4.4535	5.8529
	Reactance High	Face Sheet OAR	Negative	-0.4856	-0.0650
	Resistance Low	Face Sheet OAR	Positive	4.4535	3.8134
	Reactance Low	Face Sheet OAR	Positive	-0.4856	-0.7237
Approach					
	Impedance Type	**Parameter**	**Parameter Tolerance Variation**	**Design Impedance Value**	**Model Impedance**
Laser Drilled	Resistance High	Septum OAR	Positive	3.1370	4.2292
	Reactance High	Face Sheet OAR	Negative	-0.3085	0.0283
	Resistance Low	Septum OAR	Negative	3.1370	2.4938
	Reactance Low	Face Sheet OAR	Positive	-0.3085	-0.5346
Hexcel	Resistance High	Face Sheet OAR	Negative	3.1369	3.8431
	Reactance High	Face Sheet OAR	Negative	-0.3088	0.1932
	Resistance Low	Face Sheet OAR	Positive	3.1369	2.9436
	Reactance Low	Face Sheet OAR	Positive	-0.3088	-0.5967

7.4. Attenuation Variation Due to Manufacturing Tolerance for the Sub-Optimum Linings

A systematic search of the uncertainty of realized impedance related to manufacturing tolerances was performed as described in Section 7.3. It was performed for the approach and sideline operating conditions in each duct with each sub-optimum lining. The associated installed attenuation levels are shown in Figs. 58 and 59. These figures illustrate the importance of considering a sub-optimum design. The design attenuations were lower than those seen in the optimum design case. The optimum design results can be seen in Figs. 28 and 29. They were still, however, at an adequately high level to satisfy the performance requirements. When the manufacturing process uncertainties were taken into consideration, the minimum potential attenuation was comparable for each sub-optimum lining in the smaller duct. This indicated that the sub-optimum designs were as effective as the optimum designs. This is critical, because the optimal designs cannot be physically realized. In the larger duct, each sub-optimum lining again performed nearly as well or better than the optimum linings. Though better performance is not guaranteed, these studies clearly indicate the importance of the sub-optimum design and analysis methods.

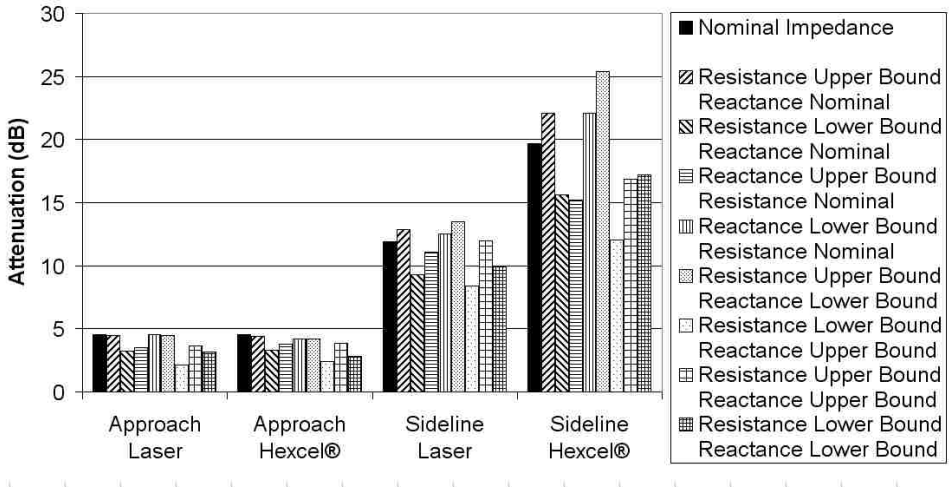

Figure 58. Variation in propagation attenuation due to manufacturing tolerance in the smaller duct for the sub-optimum design.

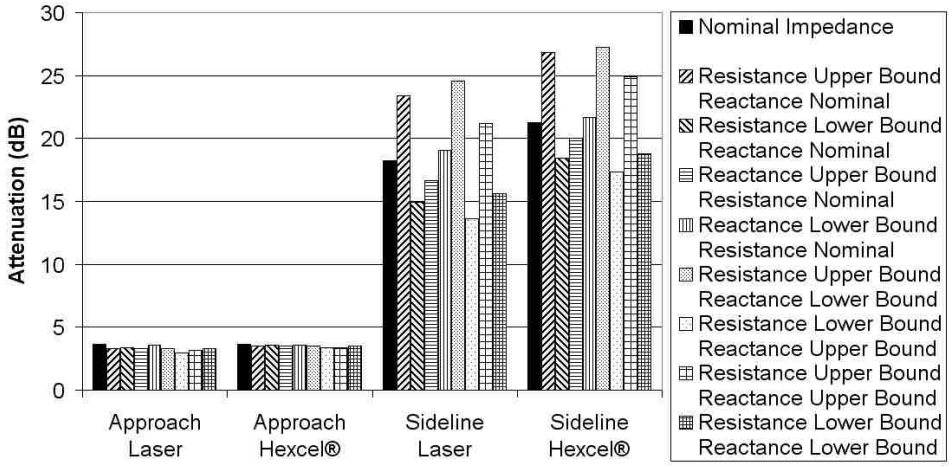

Figure 59. Variation in propagation attenuation due to manufacturing tolerance in the larger duct for the sub-optimum design.

7.5. Attenuation Variation Due to Manufacturing Tolerance with SPL Spectrum Variation for the Sub-Optimum Linings

As described in Section 8.2. local SPL spectrum variation was considered in the attenuation calculations. The results can be seen in Figs. 60 and 61. When compared with the optimum design attenuation results shown in Figs. 32 and 33, it is shown that there

was a loss in performance with the sub-optimum designs. But, the attenuation loss compared to the optimum designs was reasonable given the manufacturing constraints. This indicated once again that the sub-optimum designs should be used in each duct.

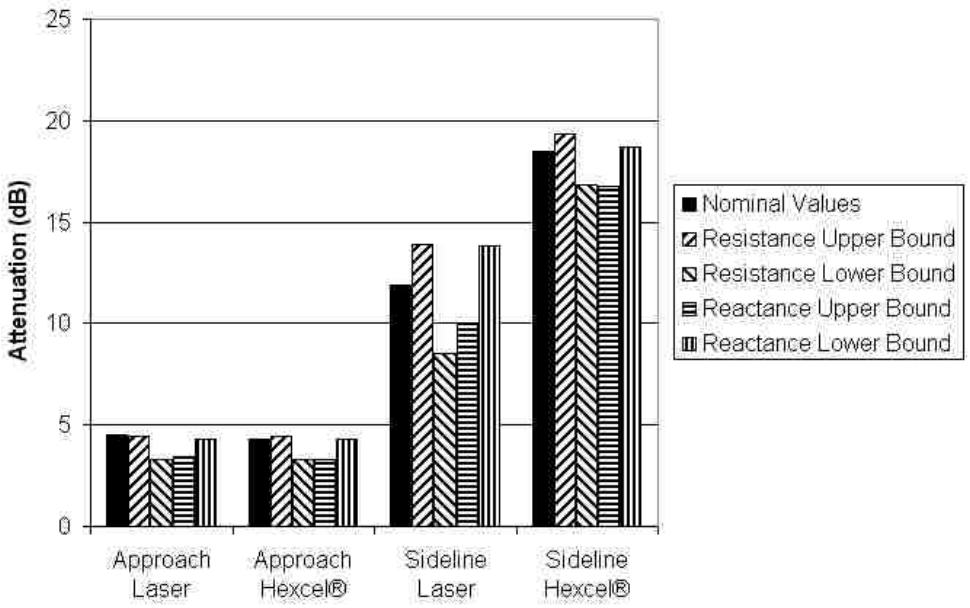

Figure 60. Variation in propagation attenuation due to manufacturing tolerance and local impedance variation in the smaller duct for the sub-optimum design.

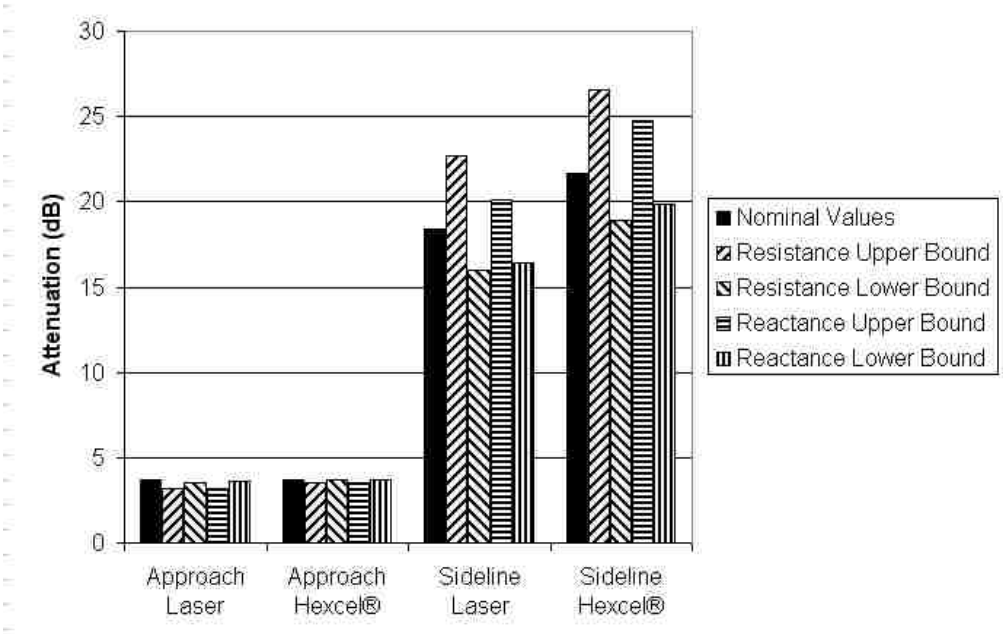

Figure 61. Variation in propagation attenuation due to manufacturing tolerance and local impedance variation in the larger duct for the sub-optimum design.

8. CONCLUSIONS

This work used iterative models for two DOF lining impedance and finite element propagation models to design eight linings and evaluate their performance. Optimum uniform lining impedance was determined on the basis of maximizing acoustic power attenuation at two operating conditions not accounting for the effects of local impedance variation due to local SPL and grazing flow Mach number for two ducts. The optimization process led to a high sensitivity of impedance to variation in lining parameters. Optimum lining model parameters required to best achieve the target impedances were determined using a particle swarm optimization technique. When these parameters were found to be outside of a manufacturable range, parameters for a separate set of sub-optimum linings were determined using particle swarm optimization with a constrained search space. It was shown that each sub-optimum lining design was an acceptable alternative to the optimum designs. The impedance of each lining design was then modeled subjected to a wide range of operating conditions including the two for which it was designed. In a separate analysis, the impedance of the linings was modeled subjected to an exhaustive set of manufacturing tolerance combinations at the two operating conditions for which they were designed. The effects on attenuation of these impedance variations were modeled in two ways. In one, a propagation model was used in which the SPL spectrum at the source set the SPL locally at the lining. In this case local grazing flow Mach number was used by the lining model to produce locally varying impedance. In the second propagation model an iterative approach was used to allow local dependence of impedance on SPL.

In the analysis method advantage was taken of the fact that lining and propagation models were computationally very efficient. This allowed an exhaustive evaluation of impedance and attenuation over a wide range of operating conditions and physical and geometric parameter variations of the linings. A large data base can be formed and information becomes available on effects of manufacturing tolerance on impedance and attenuation. It has been shown that each lining considered shows significant impedance and attenuation uncertainties due to manufacturing tolerance levels.

Observations were made on the basis of linings optimized for specific applications, and the sensitivity of attenuation performance to individual parameter uncertainties was undoubtedly case dependent. The analysis method is general and can reveal the most direct ways to limit performance uncertainties in any application. When combined with a manufacturing cost-benefit analysis it provides a method to identify the most significant contributors to error and to project the cost of producing a lining that is most likely to perform within an acceptable range of attenuation.

9. REFERENCES

[1] Murray, P., Ferrante, P., and Scofano, A., "Manufacturing Process and Boundary Layer Influences on Perforate Lining Impedance", AIAA-2005-2849, 2005.

[2] Jones, M., Parrott, T., and Watson, W., "Uncertainty and Sensitivity Analyses of a Two-Parameter Impedance Prediction Model", AIAA-2008-2928, 2008.

[3] Jones, M., Tracy, M., Watson, W., and Parrott, T., "Effects of Lining Geometry on Acoustic Impedance", AIAA-2002-2446, 2002.

[4] Yu, J., Ruiz, M., and Kwan, H., "Validation of Goodrich Perforate Lining Impedance Model Using NASA Langley Test Data", AIAA-2008-2930, 2008.

[5] Gallman, J., and Kunze, R., "Grazing Flow Acoustic Impedance Testing for the NASA AST Program", AIAA-2002-2447, 2002.

[6] Melling, T. H., "The Acoustic Impedance of Perforates at Medium and High Sound Pressure Levels", *Journal of Sound and Vibration*, 29(1), 1973, pp. 1-65.

[7] Kraft, J., Yu, J, and Kwan, H., "Acoustic Treatment Impedance Models for High Frequencies", 3rd AIAA/CEAS Aeroacoustics Conference, AIAA-97-1653, 1997.

[8] Stinson, M. R. and Shaw, E. A. G., "Acoustic Impedance of Small Circular Orifices in Thin Plates", *Journal of the Acoustical Society of America*, 77(6), 1985, pp. 2039-2042.

[9] Nelder, J., and Mead, R., "A Simplex Method for Function Minimization", *Computer Journal*, (7), 1965, pp. 308-313.

[10] Kennedy, J., and Eberhart, R., "Particle Swarm Optimization," IEEE International Conference on Neural Networks, Vol. 4, IEEE Service Center, Piscataway, NJ, 1995, pp. 1942-1948.

[11] Eversman, W., "A Reverse Flow Theorem and Acoustic Reciprocity in compressible Potential Flow in Ducts", *Journal of Sound and Vibration*, 264(1), 2001, pp. 71-95.

[12] Listerud, E., and Eversman, W., "Finite Element Modeling of Acoustics Using Higher Order Elements. Part I: Nonuniform Duct Propagation", *Journal of Computational Acoustics*, 12(3), 2004, pp. 397-429.

[13] Eversman, W., "The Boundary Condition at an Impedance Wall in a Non-Uniform Duct With Potential Mean Flow", *Journal of Sound and Vibration*, 246(1), 2001, pp. 63-69.

[14] Eversman, W., "Numerical Experiments on Acoustic Reciprocity in Compressible Potential Flows in Ducts", *Journal of Sound and Vibration*, 246(1), 2001, pp. 97-113.

[15] Listerud, E., and Eversman, W., "Finite Element Modeling of Acoustics Using Higher Order Elements. Part II: Turbofan Acoustic Radiation", *Journal of Computational Acoustics*, 12(3), 2004, pp. 431-446.

[16] Zlavog, G., and Eversman, W., "Source Effects on Attenuation in Lined Ducts. Part I: A Statistically Based Computational Approach", *Journal of Sound and Vibration*, 307, 2007, pp. 113-138.

[17] Zlavog, G., and Eversman, W., "Source Effects on Attenuation in Lined Ducts. Part II: Statistical Properties", *Journal of Sound and Vibration*, 307, 2007, pp. 113-138.

[18] Myers, M., K., "On the Acoustic Boundary Condition in the Presence of Flow", *Journal of Sound and Vibration*, 71, 1980, pp. 429-434.

[19] Eversman, W., "Numerical Experiments on Acoustic Reciprocity in Compressible Potential Flows in Ducts", *Journal of Sound and Vibration*, 246(1), 2001, pp. 97 113.

[20] Heidelberg, E., and Rice, E., "Acoustic Performance of Inlet Suppressors on an Engine Generating a Single Mode", AIAA-81-1965, 1965.

[21] Jones, M., Parrott, T., and Watson, W., "Comparison of Acoustic Impedance Eduction Techniques for Locally-Reacting Linings", AIAA-2003-3306, 2003.

[22] Drevon, E., "Measurement Methods and Devices Applied to A380 Nacelle Double Degree-Of-Freedom Acoustic Lining Development", AIAA-2004-2907, 2004.

[23] Jones, M., Watson, W., and Parrott, T., "Benchmark Data for Evaluation of Aeroacoustic Propagation Codes with Grazing Flow", AIAA-2005-2853, 2005.

[24] Nark, D., Watson, W., and Jones, M., "Uncertainty and Sensitivity Analyses of Duct Propagation Models", AIAA-2008-2832, 2008.

[25] Watson, W., Jones, M., and Parrott, T., "Investigation of an anomaly Observed in Impedance Eduction Techniques", AIAA-2008-3013, 2008.

[26] Listerud, E., and Eversman, W., "Finite Element Modeling of Acoustics Using Higher Order Elements. Part II: Turbofan Acoustic Radiation", *Journal of Computational Acoustics*, 12(3), 2004, pp. 431-446.

PAPER

2. NORMAL INCIDENCE IMPEDANCE MEASUREMENT AT ELEVATED TEMPERATURES

ABSTRACT

An impedance tube, with an associated data analysis method, was developed that allowed the measurement of impedance of acoustic samples at elevated temperatures. The traditional two-microphone impedance tube method was combined with a finite element model that transfers impedance from a transition plane to the sample across a known temperature profile within the impedance tube. This impedance measurement method was validated at room temperature by comparing the results with predicted impedance from empirically based impedance models and with impedance measurements in a standard traversing microphone impedance tube. Impedance for four samples was measured at elevated temperatures, and the results were compared to room temperature measurements. For two of the samples, the impedances measured at elevated temperatures were compared to the results of extensions of room temperature empirical models, confirming the trend of the results of the elevated temperature measurements. Finally, this work examined uncertainty in measured impedance due to uncertainty in the definition of the temperature profile in the air within the impedance tube.

1. INTRODUCTION

Standing wave normal incidence impedance tubes are an established technology. They typically have either one microphone that traverses the length of the tube and measures the standing wave pattern [1, 2] or two microphones mounted in the tube sidewall at a fixed location [2 - 8]. These methods require plane wave acoustic propagation and a uniform speed of sound along the length of the tube. In some applications impedance of an acoustic material sample must be measured at high temperature. If the entire impedance tube is run at an elevated temperature, obvious problems can arise with the driver and microphones, which can function only over a limited temperature range. This investigation proposes a new procedure in which the sample is heated in an oven at the termination end of the tube. The temperature, density, and speed of sound profiles in the tube are allowed to seek their natural levels so that the temperature reduces with increasing distance from the sample. It has been found that with sample temperatures of interest it is possible to have both the acoustic driver and the microphones operate at near ambient temperature if they are located a suitable distance from the sample. The location of a temperature measurement point determines the reference plane in which impedance is measured. The final step of translating this impedance to the sample face plane is accomplished by modeling this propagation path with a one-dimensional finite element model, which replaces the analytical translation that is a feature of the traditional two-microphone method.

The length of the modified impedance tube tested here permitted both the driver and microphones to operate at near ambient temperatures and in a region with locally

uniform temperature. The choice of tube length was ad hoc and based on the philosophy that a simple circulating water coil could be wrapped around the hot end of the tube to control the temperature profile. With the microphones placed 2.69 m from the heated end of the tube, active cooling was not necessary when the sample was at approximately 394 °C, the maximum temperature at which the most robust of the samples could be safely tested. Testing was performed with a broad band noise source, and Fourier analysis based on microphone autocorrelation and cross-correlation was consistent with published procedures. Care was exercised to ensure a satisfactory signal-to-noise ratio due to a less than ideal acoustic environment for the testing.

Validation was carried out using several approaches. Samples of common absorbing materials such as ceiling tiles were tested at room temperature in the new tube and in an older classroom demonstration tube that uses the traversing microphone method. Comparisons showed reasonable agreement when it is considered that the tubes were of different diameters precluding the use of identical samples of the obviously nonuniform material. In a second approach, materials for which approximate analytical models exist were tested for impedance at room temperature, and the results were compared with the models. Given that the models are not exact, the results were reasonably close. Benchmarking is difficult at elevated temperatures, because proven high temperature impedance models are not available. Nevertheless, comparisons with best impedance model estimates were used, and comparison was not unreasonable. Comparisons were better in the case for which there was more confidence in the model.

This paper begins with a review of the essentials of the traditional two-microphone method based on one-dimensional wave propagation, leading to the transfer function manipulations required to determine impedance and absorption coefficient. The finite element model for propagation in a medium with nonuniform density and speed of sound is introduced and it is shown how to couple it with the traditional two-microphone method. Several analytical benchmark tests are given to substantiate the analysis procedure. The new elevated temperature test apparatus is then shown in detail and experimental benchmarking and other experimental results are presented.

2. ELEVATED TEMPERATURE IMPEDANCE MEASUREMENT

The acoustic impedance of a material determines how it reacts with an acoustic environment [9]. Measurement of acoustic impedance traditionally requires a pressure measurement transducer, which has a limited operational temperature range. The temperature of a material can directly affect its acoustic impedance, so it can be necessary to measure a material's impedance at temperatures outside of typical transducer limits. The method presented here allows the transducers to remain at room temperature while the sample is heated beyond the operational limits of the transducer. The method uses a combination of traditional two-microphone tube impedance measurement and finite element modeling code.

The two-microphone method is used in the region of the tube where the temperature, speed of sound, and density are uniform. Impedance is determined at the termination of this region known as the transition plane. The finite element method is implemented in a form that allows the determination of termination impedance for known source plane impedance. The measured transition plane impedance from the two-microphone method becomes the source plane impedance for the finite element method model and is effectively translated across the temperature profile to the sample face plane.

2.1. Two-Microphone Impedance Analysis

The typical two-microphone method test fixture consists of an acoustic driver coupled to one end of a tube and a sample to be tested inserted into the other end of the tube. Microphones are mounted in the side of the tube. The geometry is shown in Fig. 1.

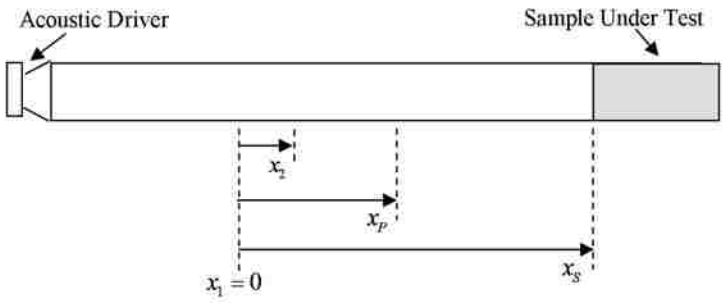

Figure 1. Schematic of a typical two-microphone impedance tube.

With the assumption of plane wave harmonic propagation within the tube, the complex pressure amplitude at two locations in the tube can be expressed as

$$P_1(\omega, x_1) = P_r(\omega)e^{i(-kx_1)} + P_l(\omega)e^{i(kx_1)} \tag{1}$$

and

$$P_2(\omega, x_2) = P_r(\omega)e^{i(-kx_2)} + P_l(\omega)e^{i(kx_2)}, \tag{2}$$

where $P_1(\omega, x_1)$ and $P_2(\omega, x_2)$ represent complex pressures measured within the tube by Microphones 1 and 2 respectively, $P_r(\omega)$ and $P_l(\omega)$ are the amplitudes of the right and left running pressure waves respectively, ω is the angular frequency, c is the speed of sound, and $k = \omega / c$ is the wave number [9]. x_1, x_2, x_P, and x_S are locations along the tube relative to a fixed reference point. Microphone 1, Microphone 2, the transition plane, and the sample face are located at x_1, x_2, x_P, and x_S respectively. A solution for $P_r(\omega)$ and $P_l(\omega)$ in terms of the measured pressures yields

$$P_r(\omega) = \frac{P_1(\omega, x_1)e^{i(kx_2)} - P_2(\omega, x_2)e^{i(kx_1)}}{e^{i(k(x_2-x_1))} - e^{i(-k(x_2-x_1))}} \tag{3}$$

and

$$P_l(\omega) = \frac{P_1(\omega, x_1)e^{i(-kx_2)} - P_2(\omega, x_2)e^{i(-kx_1)}}{e^{i(-k(x_2-x_1))} - e^{i(k(x_2-x_1))}}. \tag{4}$$

Equations (3) and (4) are used to determine the ratio

$$\frac{P_l(\omega)}{P_r(\omega)} = \frac{\frac{P_2(\omega,x_2)}{P_1(\omega,x_1)}e^{i(-kx_1)} - e^{i(-kx_2)}}{e^{i(kx_2)} - \frac{P_2(\omega,x_2)}{P_1(\omega,x_1)}e^{i(kx_1)}}. \tag{5}$$

Let s be the spacing between the two microphones, and let

$$H_{12}(\omega) = \frac{G_{12}(\omega)}{G_{11}(\omega)} = \frac{P_2(\omega, x_2)P_1^*(\omega, x_1)}{P_1(\omega, x_1)P_1^*(\omega, x_1)} = \frac{P_2(\omega, x_2)}{P_1(\omega, x_1)} \tag{6}$$

where $H_{12}(\omega)$ is the instantaneous transfer function between the two microphone locations, $G_{11}(\omega)$ is the auto power spectrum, $G_{12}(\omega)$ is the cross power spectrum, and the * denotes the complex conjugate. This is consistent with the ASTM Standard [3]. Equation (5) becomes

$$\frac{P_l(\omega)}{P_r(\omega)} = \frac{H_{12}(\omega) - e^{i(-ks)}}{e^{i(ks)} - H_{12}(\omega)}e^{i(-2kx_1)}. \tag{7}$$

The frequency dependent acoustic reflection coefficient, $R_c(\omega)$, is defined as

$$R_c(\omega) = \frac{P_l(\omega)}{P_r(\omega)}. \tag{8}$$

The axis system origin is taken at the location of Microphone 1. Then $x_1 = 0$, and the frequency dependent reflection coefficient referenced to the origin becomes

$$R_c(\omega) = \frac{H_{12}(\omega) - e^{i(-ks)}}{e^{i(ks)} - H_{12}(\omega)}. \tag{9}$$

The normal incidence absorption coefficient, $\alpha(\omega)$, is defined as

$$\alpha(\omega) = 1 - \left|R_c(\omega)\right|^2. \tag{10}$$

The acoustic impedance, $\tilde{Z}(\omega, x)$, is defined as

$$\tilde{Z}(\omega, x_P) = \frac{P(\omega, x_P)}{u(\omega, x_P)} = \rho c \frac{e^{i(-kx_P)} + R_c(\omega) e^{i(kx_P)}}{e^{i(-kx_P)} - R_c(\omega) e^{i(kx_P)}}, \tag{11}$$

where $P(\omega, x)$ is the acoustic pressure $u(\omega, x)$ is the acoustic particle velocity, ρ is the density of air, and c is the speed of sound in air. Impedance can be calculated at any plane along the tube. The term x_P is defined as the distance between Microphone 1 and the desired impedance plane. If $x_P = x_s$ the impedance at the sample face is calculated.

2.2. Finite Element Modeling Code

Acoustic measurements required to determine impedance of the sample cannot be made directly adjacent to the sample due to the high temperature environment. Furthermore, in the vicinity of the sample large temperature and density variation of the acoustic medium will exist rendering the standard approaches of deducing impedance from acoustic pressure measurements based on standing waves in a uniform medium inapplicable. At a suitable distance from the sample where temperature and density variations are negligible, defined as the transition plane, acoustic impedance can be deduced by standard methods and transferred to the sample location. A method for transferring measured impedance at the transition plane to the sample location is

proposed here. It is based on an iterative process in which the termination impedance is assumed, and the impedance at the transition plane is computed. A downhill Simplex optimization scheme is used to minimize the magnitude squared error between the varied termination impedance and the known measured impedance at the transition plane.

The mathematical model for propagation in the tube assumes a nonviscous, nonheat conducting medium with a specified steady, one-dimensional temperature and density field. Acoustic propagation is considered to be in the form of linear plane waves.

2.2.1. Fundamental Equations for Acoustic Propagation in a Medium with Temperature and Density Gradients

In a similar problem involving acoustic propagation in combustion cans, Kapur, Cummings, and Mungur [10] and Cummings [11] have formulated the governing equations for the acoustic field in a duct or tube containing an acoustic medium with nonuniform temperature, density, and speed of sound. The nonuniformity was in this case due to a heat source (flame) at one end of the tube. The principal goal was to model the acoustic impedance seen by the source that is represented by the combustion zone. In the present study that general model is adopted, but the development of the governing field equations is somewhat more extensive, beginning with first principles.

It was assumed in this analysis that the standing wave tube was of suitable diameter, or alternatively that the frequency range of interest was sufficiently low so that only plane waves propagated. The properties of the acoustic medium were assumed to vary only along the duct axis and not transverse to it. This means that the model of

propagation in the tube is one-dimensional. It was assumed that a heat source present produced a variation of temperature of the acoustic medium in which the highest temperature was at the sample end, and the lowest was at the source end of the tube. The ambient pressure in the tube was assumed uniform, and density varied with temperature according to the perfect gas law. The governing equations for acoustic propagation in the tube were based on linear acoustic perturbations on the initially quiescent medium. The fundamental equations for a nonviscous medium without heat conduction are

Continuity:

$$\frac{\partial \rho}{\partial t} + div\, \rho \vec{V} = 0 \tag{12}$$

Momentum:

$$\frac{\partial}{\partial t} \rho \vec{V} + div\, \rho \vec{V}\vec{V} = \text{-}grad\ p \tag{13}$$

Energy:

$$\frac{\partial}{\partial t} \rho \left[\hat{u} + \frac{V^2}{2} \right] + div\, \rho \left[\hat{u} + \frac{V^2}{2} + \frac{p}{\rho} \right] \vec{V} = 0 . \tag{14}$$

In Eqs. (12) through (14) p is fluid pressure, ρ is density, $\hat{u}$ is internal energy per unit mass, and $\vec{V}$ is fluid velocity, $\vec{V} = V \vec{i}$.

A modified form of the momentum equation is obtained by expanding Eq. (13) and then using the continuity Eq. (12) to yield

$$\rho \frac{\partial \vec{V}}{\partial t} + \rho \vec{V} \cdot grad\, \vec{V} = -grad\ p . \tag{15}$$

Internal energy per unit mass is given in terms of temperature, T, pressure, p, density, ρ, specific heat, c_v, and gas constant, R_g, by using the perfect gas law $p = \rho R_g T$ yielding

$$\hat{u} = c_v T = \frac{c_v}{R_g}\frac{p}{\rho}. \tag{16}$$

Internal energy in terms of pressure is defined by

$$\rho\hat{u} = \frac{c_v}{R_g}p = \frac{1}{\gamma - 1}p \tag{17}$$

and enthalpy by

$$\rho\hat{u} + p = \frac{\gamma}{\gamma - 1}p. \tag{18}$$

The energy equation is rewritten, with γ assumed constant, as

$$\frac{1}{\gamma - 1}\frac{\partial p}{\partial t} + \frac{\gamma}{\gamma - 1} div\, p\vec{V} + \frac{\partial}{\partial t}\rho\frac{V^2}{2} + div\,\rho\frac{V^2}{2}\vec{V} = 0. \tag{19}$$

The continuity Eq. (12) is used to eliminate two terms in an expanded version of Eq. (19) to obtain

$$\frac{1}{\gamma - 1}\frac{\partial p}{\partial t} + \frac{\gamma}{\gamma - 1} div\, p\vec{V} + \rho\frac{\partial}{\partial t}\frac{V^2}{2} + \rho\vec{V}\cdot grad\frac{V^2}{2} = 0. \tag{20}$$

The identity

$$grad\frac{V^2}{2} = \vec{V}\times\nabla\times\vec{V} + \vec{V}\cdot grad\,\vec{V} \tag{21}$$

is used with the additional identity

$$\vec{V}\cdot\vec{V}\times\nabla\times\vec{V} = 0 \tag{22}$$

to obtain yet another form of the energy equation

$$\frac{1}{\gamma-1}\frac{\partial p}{\partial t}+\frac{\gamma}{\gamma-1}div\, p\vec{V}+\rho\vec{V}\cdot\left[\frac{\partial\vec{V}}{\partial t}+\vec{V}\cdot grad\,\vec{V}\right]=0\,, \tag{23}$$

which with the momentum Eq. (15) simplifies to

$$\frac{1}{\gamma-1}\frac{\partial p}{\partial t}+\frac{\gamma}{\gamma-1}div\, p\vec{V}-\vec{V}\cdot grad\ p=0\,. \tag{24}$$

With the identity $div\, p\vec{V}=p\,div\vec{V}+\vec{V}\bullet grad\ p$ and a collection of terms results in

$$\frac{\partial p}{\partial t}+\gamma\ p\,div\vec{V}+\vec{V}\cdot grad\ p=0\,. \tag{25}$$

Insert the continuity equation in the form

$$div\vec{V}=-\frac{1}{\rho}\left[\frac{\partial\rho}{\partial t}+\vec{V}\cdot grad\ \rho\right] \tag{26}$$

into Eq. (26) and rearrange to obtain the final form of the energy equation

$$\frac{\partial p}{\partial t}+\vec{V}\cdot grad\ \ p=\frac{\gamma p}{\rho}\left[\frac{\partial\rho}{\partial t}+\vec{V}\cdot grad\ \rho\right]\,. \tag{27}$$

Equation (27) at this point has not been restricted to one dimension and is subject only to the constraint that γ is constant (in addition to nonviscous, nonheat conducting).

The acoustic approximation is obtained by considering small perturbations on the assumed ambient medium with properties p_0 , ρ_o , and $\vec{V}_0$ with the relations

$$\begin{aligned} p&=p_0+\tilde{p}\\ \rho&=\rho_0+\tilde{\rho}\\ \vec{V}&=\vec{V}_0+\vec{v} \end{aligned}\,. \tag{28}$$

Enforce the assumption of no steady mean flow $\left(\vec{V}_0=0\right)$ and uniform mean pressure $\left(grad\ p_0=0\right)$ to obtain a linearized acoustic continuity equation

$$\frac{\partial \rho}{\partial t} + \rho_0 \, div \, \vec{v} + \vec{v} \cdot grad \, \rho_0 = 0 \tag{29}$$

where for simplicity of notation the perturbation density and pressure $\tilde{\rho}$ and $\tilde{p}$ are replaced by ρ and p. Similarly, a linearized acoustic momentum equation is

$$\rho_0 \frac{\partial \vec{v}}{\partial t} = -grad \, p \, , \tag{30}$$

and a linearized acoustic energy equation is

$$\frac{\partial p}{\partial t} = \frac{\gamma p_0}{\rho_0} \left[\frac{\partial \rho}{\partial t} + \vec{v} \cdot grad \, \rho_0 \right] . \tag{31}$$

The local speed of sound in the medium is defined by

$$c_0{}^2 = \frac{\gamma p_0}{\rho_0} . \tag{32}$$

This leads to the final linearized form of the acoustic energy equation

$$\frac{\partial p}{\partial t} = c_0{}^2 \left[\frac{\partial \rho}{\partial t} + \vec{v} \cdot grad \, \rho_0 \right] , \tag{33}$$

where $c_0{}^2 = \gamma R_g T_0 = c_0{}^2 (x)$ and $\rho_0 = \rho_0 (x)$.

An acoustic wave equation is found by first combining the acoustic continuity Eq. (29) and acoustic energy Equation (33) to obtain

$$\frac{1}{c_0{}^2} \frac{\partial p}{\partial t} + \rho_0 \, div \, \vec{v} = 0 . \tag{34}$$

Equation (34) and the acoustic momentum Eq. (30) are combined to produce a wave equation

$$\frac{1}{c_0{}^2} \frac{\partial^2 p}{\partial t^2} - \nabla^2 p + \frac{1}{\rho_0} grad \, \rho_0 \cdot grad \, p = 0 . \tag{35}$$

With the restriction that the density gradient is one-dimensional with $grad\,\rho_0 = \frac{\partial \rho_0}{\partial x}\vec{i}$, the wave equation is

$$\nabla^2 p - \frac{1}{\rho_0}\frac{\partial \rho_0}{\partial x}\frac{\partial p}{\partial x} - \frac{1}{{c_0}^2}\frac{\partial^2 p}{\partial t^2} = 0 . \tag{36}$$

A nondimensional form is formed by the replacements

$$p \to \rho_s {c_s}^2 p \quad , \quad \rho \to \rho_s \rho \quad , \quad x \to Rx \quad , \quad r \to Rr \quad , \text{ and, } \quad t \to \frac{R}{c_s} t$$

where ρ_s, p_s, and c_s are conditions at the acoustic source plane, θ is the angular location in the cross-section of the duct, and R is the duct radius, assumed uniform in the present case. Harmonic excitation is assumed in the form $p = P(x,r,\theta)e^{i\omega t} \to P(x,r,\theta)e^{i\eta t}$, with $\eta_r = \frac{\omega R}{c_s}$. Nondimensional mean properties of the acoustic medium are defined by $\rho_r = \frac{\rho_0}{\rho_s}$ and $c_r = \frac{c_0}{c_s}$. The nondimensional form of the Helmholtz equation for this problem is

$$\nabla^2 p - \frac{1}{\rho_r}\frac{\partial \rho_r}{\partial x}\frac{\partial p}{\partial x} + \frac{{\eta_r}^2}{{c_r}^2} p = 0 . \tag{37}$$

Equation (37) describes harmonic acoustic excitation in a duct with a temperature and density variation. The density variation is restricted to be one-dimensional along the x axis. The temperature variation, represented by the speed of sound, is not restricted to being one-dimensional, however in this analysis it is assumed that it is. Equation (37) is not restricted to a one-dimensional acoustic field, and the finite element method numerical model is in principal three-dimensional. The choices of duct geometry, boundary conditions, and acoustic source conditions are chosen so that only plane wave

propagation is considered. This field equation, referred to here as a Helmholtz equation, is augmented by boundary conditions. On the lateral surfaces of the duct it is assumed that the normal acoustic velocity vanishes, $\vec{v}\bullet\vec{n}=0$, where $\vec{n}$ is the unit outward normal. At the end of the duct, $x=L$, an impedance condition is given in the form

$$p=\frac{\tilde{Z}}{\rho_s c_s}\,\vec{v}\bullet\vec{n}=Z\,\vec{v}\bullet\vec{n}\,. \tag{38}$$

$\tilde{Z}$ is the dimensional normal incidence acoustic impedance, and Z is the nondimensional normal acoustic impedance, defined relative to source density and speed of sound. The source at $x=0$ is defined in terms of acoustic pressure or normal acoustic velocity, $\vec{v}\bullet\vec{n}$. Normal velocity boundary conditions are replaced by acoustic pressure gradient boundary conditions by using the acoustic momentum Eq. (31) in nondimensional form

$$\vec{v}\bullet\vec{n}=\frac{i}{\eta_r\rho_r}\nabla p\bullet\vec{n}\,. \tag{39}$$

At the source plane the nondimensional mean density is $\rho_r=\rho_0/\rho_s=1$, and at the termination plane $\rho_r=\rho_t/\rho_s$ where ρ_t is the density at the termination plane.

Acoustic energy density and acoustic energy flux follow from Eq. (30) multiplied by $\vec{v}$,

$$\rho_0\vec{v}\bullet\frac{\partial\vec{v}}{\partial t}=-\vec{v}\bullet grad\ p\,, \tag{40}$$

Eq. (34) multiplied by p,

$$\frac{1}{\rho_0 c_0{}^2}\,p\frac{\partial p}{\partial t}+\ p div\ \vec{v}=0\,, \tag{41}$$

and combined to yield

$$\frac{\partial}{\partial t}\left(\frac{1}{2}\rho_0 v^2 + \frac{1}{2\rho_0 c_0{}^2}p^2\right) + div(p\vec{v}) = 0\,. \tag{42}$$

Equation (42) is an acoustic energy equation with acoustic energy per unit volume, e, given by

$$e = \frac{1}{2}\rho_0 v^2 + \frac{1}{2\rho_0 c_0{}^2}p^2 \tag{43}$$

and acoustic energy flux per unit area $\vec{N}$ given by

$$\vec{N} = p\vec{v}\,. \tag{44}$$

These are the same results obtained for the classical wave equation in which the medium temperature, speed of sound, and density are uniform. The same conservation law applies, namely that in the present case acoustic power on any cross-section of the tube is conserved. The ambient medium does not dissipate acoustic power.

2.2.2. Finite Element Method Formulation

Kapur, Cummings, and Mungur [10] had as their goal the determination of the transfer impedance from the source (combustion area) to the termination (open ended tube). Their numerical implementation was based on a Runge-Kutta integration scheme. Cummings [11] approached the same problem with an approximate analytical method. The goal in the present study is the determination of the termination impedance with knowledge of the source impedance, somewhat the reverse of the goal in references [10, 11]. The governing "wave" Eq. (36) and its nondimensional equivalent Eq. (37) is the same as studied in references [10, 11]. The numerical approach used here was the finite element method. The code developed was based on work previously carried out related to

propagation and radiation from turbofan inlets and in nonuniform ducts [12 - 14]. These previous investigations provided the basic computational structure and most of the finite element method code used here.

A weighted residual formulation begins with an approximation $\hat{p}$ to the Helmholtz equation. The approximation $\hat{p}$ is sought such that the residual weighted with respect to each member $\tilde{W}$ of a set of functions vanishes, so that

$$\iiint_{\mathbb{R}} \tilde{W}\left(\nabla^2 \hat{p} - \frac{1}{\rho_r}\frac{\partial \rho_r}{\partial x}\frac{\partial \hat{p}}{\partial x} + \frac{\eta_r^{\,2}}{c_r^{\,2}}\hat{p}\right) dV = 0\,, \tag{45}$$

where $\mathbb{R}$ is the volume enclosed by the surfaces of the duct. A weak form of the weighted residual is introduced by using the identity

$$\tilde{W}\nabla^2 \hat{p} = \tilde{W}\nabla\bullet\nabla\hat{p} = \nabla\bullet\tilde{W}\nabla\hat{p} - \nabla\tilde{W}\bullet\nabla\hat{p} \tag{46}$$

to obtain

$$\iiint_{\mathbb{R}}\left(\nabla\bullet\tilde{W}\nabla\hat{p} - \nabla\tilde{W}\bullet\nabla\hat{p} - \frac{1}{\rho_r}\frac{\partial \rho_r}{\partial x}\tilde{W}\frac{\partial \hat{p}}{\partial x} + \frac{\eta_r^{\,2}}{c_r^{\,2}}\tilde{W}\hat{p}\right) dV = 0\,. \tag{47}$$

In this weak form of the weighted residual formulation the solution $\hat{p}$ is in the class of continuous functions as is the set of weighting functions, $\tilde{W}$.

The Divergence Theorem

$$\iiint \nabla\tilde{W}\bullet\nabla\,\hat{p}\,dV = \iint \tilde{W}\,\nabla\,\hat{p}\bullet\vec{n}\,dS \tag{48}$$

is used to isolate boundary integrals on the surface of $\mathbb{R}$ as

$$\iiint_{\mathbb{R}}\left(\nabla\tilde{W}\bullet\nabla\hat{p} + \frac{1}{\rho_r}\frac{\partial \rho_r}{\partial x}\tilde{W}\frac{\partial \hat{p}}{\partial x} - \frac{\eta_r^{\,2}}{c_r^{\,2}}\tilde{W}\hat{p}\right) dV = \iint_{S}\tilde{W}\,\nabla\hat{p}\bullet\vec{n}\,dS - \iint_{T_p}\tilde{W}\,\nabla\hat{p}\bullet\vec{n}\,dS\,. \tag{49}$$

Boundary integrals on the lateral surfaces of the duct vanish because of vanishing normal component of acoustic particle velocity. On the surface, S, the source plane, normal velocity is specified, and on the surface T_p, the termination plane, the impedance condition of Eq. (38) is applied. The weighted residual formulation is

$$\iiint_{\mathbb{R}}\left(\nabla\tilde{W}\bullet\nabla\hat{p}+\frac{1}{\rho_r}\frac{\partial\rho_r}{\partial x}\tilde{W}\frac{\partial\hat{p}}{\partial x}-\frac{\eta_r^{\,2}}{c_r^{\,2}}\tilde{W}\hat{p}\right)dV=i\eta_r\rho_r\iint_S\tilde{W}\,\hat{u}\,dS-\frac{i\eta_r\rho_r}{Z}\iint_{T_p}\tilde{W}\,\hat{p}\,dS\,. \quad (50)$$

In Eq. (50) note that the impedance is normalized relative to the source plane conditions. The formulation to this point is fully three-dimensional. The assumed axi-symmetric geometry is taken advantage of with the separation for the acoustic and internal energy field approximations

$$\hat{p}=P(x,r)\,e^{-im\theta}\ \text{and}\ \hat{u}=u(x,r)\,e^{-im\theta} \quad (51)$$

and for the weighting functions

$$\tilde{W}=W(x,r)\,e^{im\theta}\,. \quad (52)$$

The weighted residual formulation is now two-dimensional for each circumferential mode number m in the form

$$\iint_{\Sigma}\left(\frac{\partial W}{\partial x}\frac{\partial P}{\partial x}+\frac{\partial W}{\partial r}\frac{\partial P}{\partial r}+\frac{1}{\rho_r}\frac{\partial\rho_r}{\partial x}W\frac{\partial P}{\partial x}-(\frac{\eta_r^{\,2}}{c_r^{\,2}}-\frac{m^2}{r^2})WP\right)rdrdx = i\eta_r\int_0^1 W\,u\,rdr-\frac{i\eta_r\rho_r}{Z}\int_0^1 W\,P\,rdr\,. \quad (53)$$

Σ is the computational area in the x,r plane.

Acoustic pressure, $P(x,r)$, and internal energy, $u(x,r)$, are considered to be written in terms of a global interpolation matrix in based on values of acoustic pressure at discrete nodes in the computational domain. This is represented by

$$P = \left[N(x,r)\right]\underline{p} \text{ and } u = \left[N(x,r)\right]\underline{u}\,. \tag{54}$$

$\left[N(x,r)\right]$ is in principal an interpolation matrix that produces the value of the acoustic pressure and internal energy at a point x,r in the computational domain from discrete values of acoustic pressure at the nodes $\underline{p}$ and internal energy at the nodes $\underline{u}$. The weighting functions are taken as the interpolation functions to produce the discrete form of the weighted residual

$$\iint_{\Sigma}\left(\left[N_x\right]^T\left[N_x\right]+\left[N_r\right]^T\left[N_r\right]+\frac{1}{\rho_r}\frac{\partial\rho_r}{\partial x}\left[N\right]^T\left[N_x\right]-\left(\frac{\eta_r^{\,2}}{c_r^{\,2}}-\frac{m^2}{r^2}\right)\left[N\right]^T\left[N\right]\right)\underline{p}\,r\,dr\,dx$$
$$= i\,\eta_r\int_0^1\left[N\right]^T\left[N\right]\underline{u}\,r\,dr-\frac{i\,\eta_r\rho_r}{Z}\int_0^1\left[N\right]^T\left[N\right]\underline{p}\,r\,dr\,. \tag{55}$$

Equation (55) represents a discrete set of algebraic equations for the nodal values of acoustic pressure. The interpolation matrix $\left[N(x,r)\right]$ at this point exists only in principle. In the finite element formulation interpolation is done over small but finite subdomains in the x,r plane. Following standard finite element method procedures the subdomains are isoparametric quadrilaterals with quadratic serendipity interpolation functions. The weighted residual formulation of Eq. (55) is obtained by a standard finite element method assembly process.

The boundary condition at the source plane is implemented by expanding the input acoustic particle velocity in terms of incident and reflected acoustic modes scaled by their modal amplitude coefficients [12]. Incident modal amplitudes are input, and reflected modal amplitudes are part of the solution. Post-processing of the solution

determines the acoustic pressure and particle velocity both at the source and from this the source impedance.

The assumed temperature profile in the duct is specified, as is the constant steady state pressure. The perfect gas law is used to determine the mean density profile and the gradient of the mean density. These profiles are required for the finite element method model of Eq. (55).

The finite element code described is imbedded in an optimization scheme that uses the source impedance to determine the termination impedance. Termination impedance is input, and the finite element method code is run to determine the source impedance. If a known impedance is specified for the source, an initial choice for the termination impedance is made, and the magnitude squared of the difference between the resulting computed source impedance and the specified source impedance is computed and defined as the error. An iterative scheme based on the downhill Simplex method [15] is used to update the termination impedance and converge on a value that is consistent with the specified source impedance. The process converges reliably and quickly.

2.2.3. Finite Element Modeling Code Validation and Benchmarking

Several calculations are available to benchmark the finite element codes that have been developed. In the first case considered the power reflection and transmission coefficients were calculated for propagation in a medium at uniform temperature (uniform specific acoustic impedance, $\rho_1 c_1$) with the termination impedance purely

resistive with impedance $\tilde{Z} = \rho_2 c_2$. The reflection coefficient evaluated at the source for a duct of length L can be determined from a plane wave analysis as

$$R_c = \frac{P^-}{P^+} = \frac{\dfrac{\rho_2 c_2}{\rho_1 c_1} - 1}{\dfrac{\rho_2 c_2}{\rho_1 c_1} + 1} \; e^{-2ikL}. \tag{56}$$

The power reflection coefficient is

$$R_\Pi = \left| \frac{P^-}{P^+} \right|^2 = \frac{\left(\dfrac{\rho_2 c_2}{\rho_1 c_1} - 1 \right)^2}{\left(\dfrac{\rho_2 c_2}{\rho_1 c_1} + 1 \right)^2}. \tag{57}$$

The simplest version of the finite element code can be used to calculate the power reflection coefficient with a uniform temperature distribution. For this example the nondimensional termination impedance was set as $Z / \rho_1 c_1 = \rho_2 c_2 / \rho_1 c_1 = 2$. The acoustic power reflection coefficient was $R_\Pi = 1/9 = 0.111$. For the finite element method code a nondimensional frequency $kR = 2.0$ was chosen, and the tube length was taken as $5R$. Sea level conditions applied with $\rho_0 = 1.222578$ kg m-3 and $T_0 = 289$ K. Figure 2 shows contours of acoustic pressure magnitude for the acoustic field in the tube. The standing wave was generated by interaction of the incident wave and reflected wave with a power reflection coefficient of $R_\Pi = 0.111$ calculated by post-processing acoustic pressure and acoustic particle velocity from the finite element method results for the acoustic field in the tube. This was in exact agreement with the result generated from Eq. (57). Post-processing of the finite element method prediction for the acoustic field produced the source impedance $Z_s = 1.0579 - i\,0.7242$.

A second example considered the same geometry and nondimensional frequency, but now with a termination impedance of $Z = \tilde{Z} / \rho_1 c_1 = 5.20 - i1.16$. With the specified impedance the predicted acoustic power reflection coefficient was obtained from

$$R_{\Pi} = \left| \frac{P^-}{P^+} \right|^2 = \frac{|Z-1|^2}{|Z+1|^2}, \tag{58}$$

resulting in $R_{\Pi} = 0.4772$. Figure 3 shows the contours of acoustic pressure magnitude for this case. The calculated power reflection coefficient was $R_{\Pi} = 0.4772$, again calculated by post-processing acoustic pressure and acoustic particle velocity from the finite element method results for the acoustic field in the tube. This was in exact agreement with the value obtained from Eq. (58). The corresponding acoustic power absorption coefficient was $T_{\Pi} = 1 - R_{\Pi} = 0.5228$. The source impedance was $Z_s = 0.51 - i1.27$.

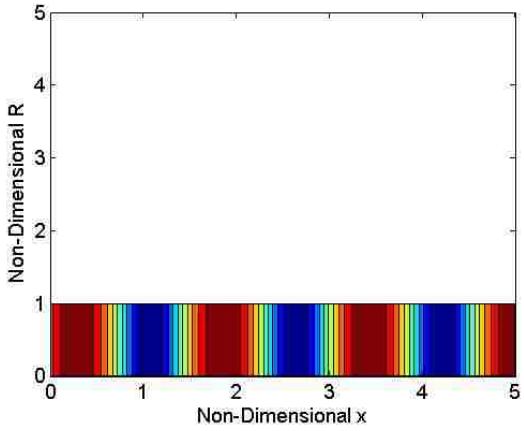

Figure 2. Acoustic pressure magnitude contours for the standing wave tube with uniform temperature and nondimensional frequency $kR = 2.0$. Termination impedance is $Z = 2.0 + i\,0.0$. The source impedance is $Z_s = 1.0579 - i\,0.7242$.

A third example calculation used a second version of the code that determined termination impedance from specified source impedance. This code is applicable to a situation in which impedance is measured at some location in the duct away from the sample, as might be the case if instrumentation had to be placed in a less hostile environment than that which existed at the sample. The case shown in Fig. 3 was used. The presumed measured impedance at the source plane, $x = 0$, was $Z_s = 0.5110 - i1.2747$, and this served as the input "target impedance". The code beginning with an initial guess for the termination impedance and with a sequence of iterations based on a downhill Simplex optimization scheme [15] converged on a termination impedance that produced the target measured (source) impedance to within a specified tolerance. In this example with constant temperature the iterated termination impedance was $Z = \tilde{Z} / \rho_1 c_1 = 5.1937 - i1.1552$, which was a very close approximation of the termination impedance used to produce the results shown in Fig. 3.

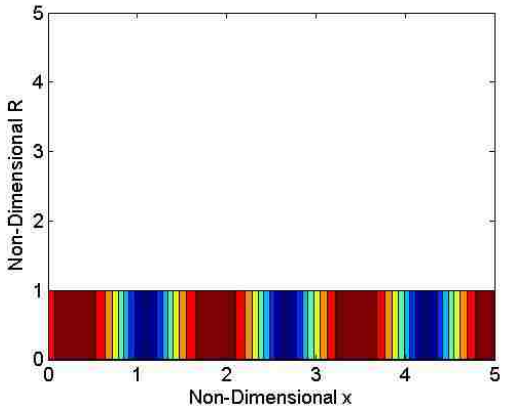

Figure 3. Acoustic pressure magnitude contours for the standing wave tube with uniform temperature and nondimensional frequency $kR = 2.0$. Termination impedance is $Z = 5.20 - i1.16$. The source impedance is $Z_s = 0.51 - i1.27$.

Another example addressed the same geometry and frequency, but with a nonuniform temperature in the tube. The temperature variation was chosen to be constant at 289 K from $x = 0.0$ to $x = 1.0$. From $x = 1.0$ to $x = 5.0$ the temperature varied linearly from 289 K to 844 K. Figures 4, 5, and 6 show the variation of mean temperature, mean density, and speed of sound for this case.

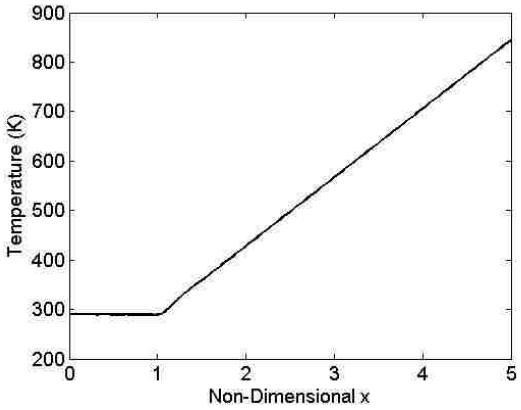

Figure 4. Variation of mean temperature in the standing wave tube.

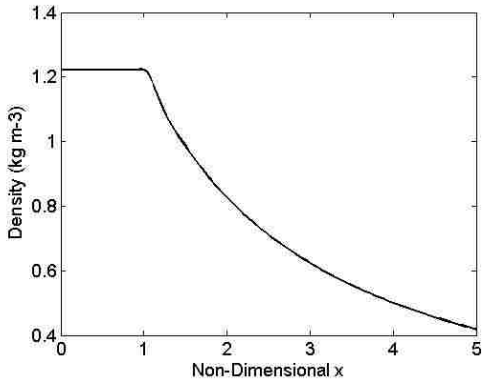

Figure 5. Variation of mean density in the standing wave tube.

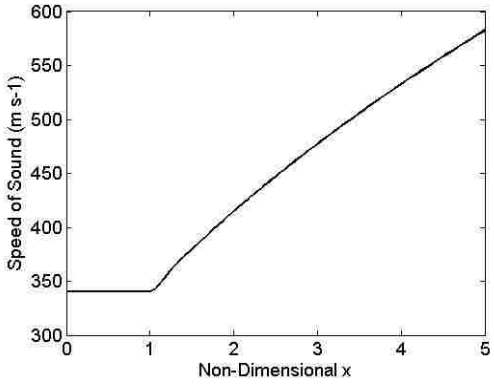

Figure 6. Variation of the speed of sound in the standing wave tube.

Figure 7 shows the acoustic pressure magnitude contours for this case. A standing wave was present, but due to the increase of temperature and speed of sound over the length of the tube the wave length became longer near the termination. With the same nondimensional impedance as in the previous case, the power reflection coefficient, $R_{\Pi} = 0.6626$, increased substantially, and the power absorption coefficient, $T_{\Pi} = 0.3374$, decreased correspondingly compared to the equivalent case when temperature was constant as shown in Fig. 3. The

source impedance was determined to be $Z_s = 0.1028 + i\,0.0624$. This case also provided a benchmark calculation for conservation of acoustic power in which acoustic power at six cross-sections along the tube was found to match source power computed from the incident and reflected waves at the source.

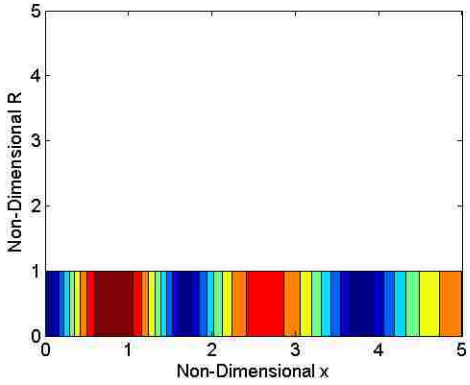

Figure 7. Acoustic pressure magnitude contours for standing wave tube with nonuniform temperature and nondimensional frequency $kR = 2.0$. Termination impedance is $Z = 5.20 - i\,1.16$. Source impedance is $Z_s = 0.10 + i\,0.06$.

A final benchmark resulted when the computed source impedance, $Z_s = 0.1028 + i\,0.0624$, was used in the iterative version of the finite element method code to determine the corresponding termination impedance. The result was $Z = 5.2028 - i\,1.1488$, a close approximation to the termination impedance used to generate the source impedance.

The finite element analysis is structured with termination impedance nondimensional with respect to the source characteristic impedance $\rho_1 c_1$. In an iteration

the impedance returned is $Z = \frac{\tilde{Z}}{\rho_1 c_1}$, where $\tilde{Z}$ is the dimensional impedance. In order to have the iterated termination impedance scaled relative to the termination characteristic impedance $\rho_2 c_2$ it is necessary to note that the dimensional impedance is $\tilde{Z} = \rho_1 c_1 Z$. Normalization of the iterated impedance relative to $\rho_2 c_2$ then yields $Z_2 = \frac{\tilde{Z}}{\rho_2 c_2} = \frac{\rho_1 c_1}{\rho_2 c_2} Z$. Z_2 is the iterated nondimensional termination impedance relative to $\rho_2 c_2$, while Z is the iterated nondimensional termination impedance relative to $\rho_1 c_1$.

2.3. Combination of the Two-Microphone and Finite Element Methods

The data reduction method used with this test fixture requires the use of both the two-microphone method and the finite element method. The two-microphone method allows the calculation of impedance at an arbitrary cross-section of the tube. It requires that the speed of sound, and therefore the air temperature, must be constant along the tube between the microphone location and the location of the impedance plane cross-section. At a sufficient distance from the furnace, the air within the tube is at room temperature. The impedance at the transition plane, x_P, can be calculated using the two-microphone method. The finite element method translates impedance from the transition plane along the tube with a varying temperature profile to the sample face. The finite element method requires the transition plane impedance from a cross-section of the tube at room temperature. This impedance is calculated using the two-microphone method and referred to as the transition plane impedance. The result is a method that calculates the impedance of a sample at an elevated temperature using pressure measurements made at room

temperature. Pressure measurements are made at the microphones, impedance is calculated from those measurements at an intermediary tube transition plane cross-section, and finally impedance is calculated at the sample face using the transition plane impedance.

3. TEST FIXTURE

The test fixture was designed to allow the measurement of the acoustic absorption coefficient, the reflection coefficient, and the impedance of an acoustic sample in an elevated temperature environment. This was achieved with a combination of the traditional two-microphone method measurement and finite element analysis. This test fixture allows acoustic signal generation and measurement to be performed at room temperature while the acoustic sample is at an elevated temperature.

A schematic of the physical structure of the test fixture can be seen in Fig. 8. It consists of a 0.3048 m diameter Audiobahn acoustic driver mounted in a sealed enclosure. A second sealed enclosure mates the face of the driver to the smaller diameter tube. The tube has a 0.0508 m inner diameter and a 0.0635 m outer diameter. It is 3.65 m long and made of stainless steel. At the other end of the tube, a 0.0508 m diameter, 0.0254 m long machined stainless steel billet is inserted as the backing plug. The acoustic sample is placed in front of the backing plug and inserted into the tube at a location inside the tube furnace, allowing the sample to be heated. A temperature profile consistent with the heating is created along the length of the tube. The tube length is sufficient to allow the driver to remain at room temperature. Instrumentation is added to perform acoustic and thermal measurements. A schematic of the instrumentation can be seen in Fig. 9.

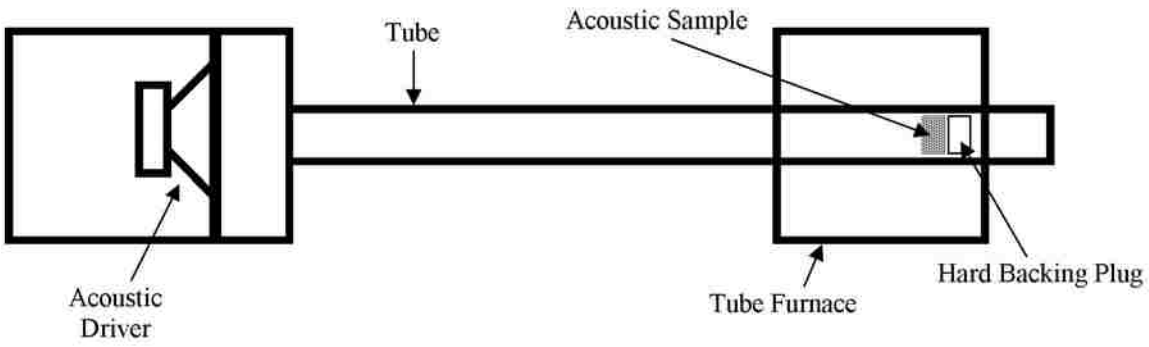

Figure 8. Schematic of the structure of the test fixture.

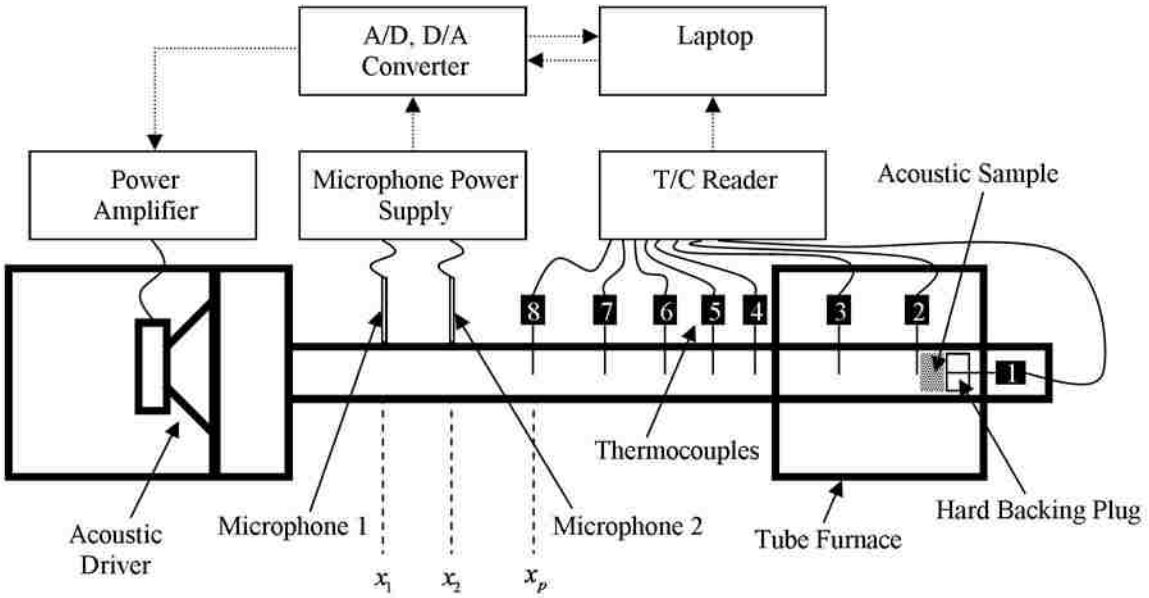

Figure 9. Schematic of the structure of the test fixture with instrumentation.

Two 0.00635 m diameter B&K type 4938 microphones with type 2670 preamplifiers are mounted perpendicular to the side of the tube flush with the tube interior. They are located at x_1 and x_2 as shown in the schematic in Fig. 9 and the photograph in Fig. 10. The microphone power supply is a B&K NEXUS 2690. A backing plug was made for calibration purposes, allowing the microphones to be mounted in the

plug with axes perpendicular to the tube cross-section. When mounted in the plug, the microphone faces are flush with the surface of the backing plug. The plug can be seen in Fig. 11.

Seven Omega type K thermocouples are mounted perpendicular to the length of the tube. They are each inserted into the tube centerline as suggested in the schematic in Fig. 9 and the photograph in Fig. 12. The sample backing plug was made to allow the insertion of another type K thermocouple through the rear to the face of the plug. It is shown in the schematic in Fig. 9 and the photograph in Fig. 13. These thermocouples are used to measure the temperature profile along the length of the tube and of the temperature difference across the acoustic sample. The thermocouple signals are read using a TempScan/1100 controlled by Omega ChartView.

Figure 10. Microphones mounted in the side of the tube in the measurement location.

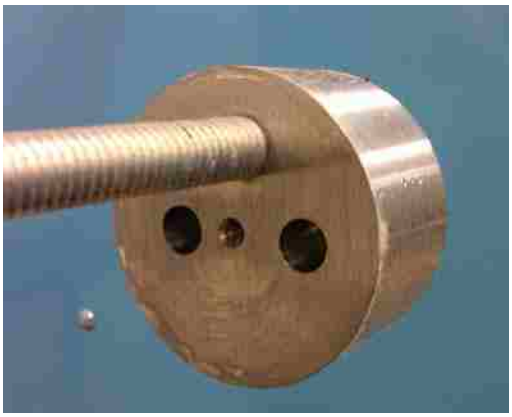

Figure 11. Backing plug used to determine microphone calibration gain and phase angle correction factors.

Figure 12. Thermocouple mounted along the length of the tube.

Figure 13. Backing plug with backing plug thermocouple.

An Echo AudioFire12 is used for all audio signal digital-to-analog and analog-to-digital conversion. It is controlled with the AudioFire Console software package, which

communicates with Adobe Audition through the ASIO transfer protocol. Adobe Audition is multi-track digital recording software. It has the capability to record multiple audio signals while simultaneously generating audio signals with the assistance of the AudioFire12. In addition it has extensive audio signal editing and analysis capabilities. These capabilities are used to produce the electronic audio signals amplified with a QSC PLX3402 power amplifier that power the acoustic driver.

4. EXPERIMENTAL PROCEDURE

Microphone responses must be characterized to ensure accurate pressure measurement. The microphone amplitude calibration (gain) factor was determined using a B&K Sound Calibrator Type 4231. This factor relates the physical acoustic sound pressure level to the equivalent digitized acoustic amplitude data used for numerical calculations. The two-microphone method requires the transfer function between two microphones. It does not require that each microphone's frequency response be calibrated precisely to the physical pressure values. However, differences in the relative frequency responses of each microphone relative to one another introduce error. Gain and phase correction factors between the two microphones were determined using end cap measurements taken with the plug shown in Fig. 11. These correction factors reduce errors due to differing microphone amplitude and phase responses. The microphones were mounted in the backing plug perpendicular to the tube cross-section and flush with the surface of the backing plug. Banded white noise was generated within the tube and measured by the microphones. Ideally, the two microphones would show identical frequency responses. In practice, however, they differ. The frequency dependent transfer function, H_{12_C}, between the two microphones was obtained to determine the amplitude and phase angle response differences between the microphones as

$$H_{12_C}(\omega) = \frac{P_{2_O}(\omega, x_2)}{P_1(\omega, x_1)}. \tag{59}$$

The uncorrected frequency response of Microphone 2, P_{2_O}, was then corrected for differences in microphone frequency response by

$$P_2(\omega, x_2) = \frac{P_{2_O}(\omega, x_2)}{H_{12_C}(\omega)}. \tag{60}$$

This reduced errors due to differing microphone frequency responses. The microphones are then mounted in the side of the tube flush with the tube interior, and the noise floor was recorded simultaneously for both microphones.

Samples were tested using a piecewise testing procedure at each temperature. The furnace was brought to temperature at a safe ramp rate of 5 °C per minute, and the temperature at each thermocouple was recorded once the system reached a steady state temperature. It is important to note that the temperature within the tube may reach equilibrium before the internal temperature of the sample. Sufficient time was allowed for the sample to reach an equilibrium temperature as well. White noise banded from 200 to 1,000 Hz was played from Adobe Audition. The QSC amplifier amplitude starting from zero was increased until the microphone signals were sufficiently high without clipping anywhere in the signal chain. Once the appropriate signal level was reached, one minute fifteen second data records were recorded simultaneously for the two microphones. The recording process was repeated using white noise banded from 800 to 2,200 Hz. The first fifteen seconds of the data records were removed to enhance signal stability. The wave files were converted to ASCII text data arrays using Adobe Audition for use in the data reduction. The furnace temperature was adjusted, and this process was repeated.

5. TEST FIXTURE VALIDATION

It was necessary to validate the test fixture against known data and accepted testing methods at room temperature before it was used to make elevated temperature measurements. Four acoustic samples were used for the validation process. A one degree-of-freedom and a two degree-of-freedom acoustic lining typical for aircraft turbofan engine noise reduction were used to validate impedance measurements. An exploded view of a generic one degree-of-freedom lining is shown in Fig. 14.

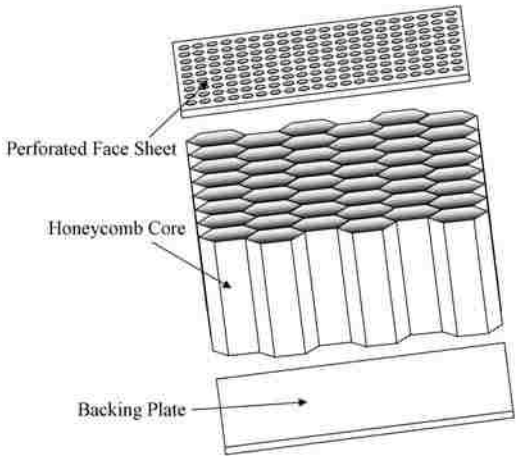

Figure 14. Exploded schematic of an acoustic lining.

It consists of a porous face sheet backed by a honeycomb core and a rigid backing plate, creating a cavity. The one degree-of-freedom lining used in this investigation consists of a drilled titanium perforated face sheet and a titanium honeycomb core. The physical parameters for the sample were: face sheet thickness 0.019 in (0.483 mm); face sheet open area ratio 0.067; face sheet hole diameter 0.043 in (1.092 mm); honeycomb depth 0.55 in (13.97 mm). The honeycomb core would normally be closed by a rigid backing

plate to complete the cavity. In the sample available for this investigation the backing plate was not included so that the backing plug filled that role. An impedance model at near standard temperature for this one degree-of-freedom lining was generated from proprietary data, however available empiricism for resistance and mass reactance for the face sheet has been limited to a pin mat perforated composite face sheet. The resulting deficiency in the face sheet model for the titanium sample is not known. It also is noted that the role of the backing plug as the sample backing plate had implications in the impedance model as described in Section 7.4.2.

A two degree-of-freedom lining was obtained by insertion of another porous layer, or septum, in the honeycomb core, creating two coupled cavities. The two degree-of-freedom lining in this investigation had a pin mat perforated composite face sheet and a porous weave material acting as the septum. Physical parameters for this sample were: face sheet thickness 0.034 in (0.864 mm); face sheet open area ratio 0.075; face sheet hole diameter 0.043 in (1.092 mm); septum insertion depth 0.19 in (4.826 mm); septum DC flow resistance 110 cgs Rayls; septum nonlinearity factor 1.7; septum cross frequency 10,000 Hz; septum backing cavity depth 1.46 in (37.084 mm). A proprietary empirically based impedance model is available for prediction of the impedance of the two degree-of-freedom lining. The empiricism of the model is based specifically on the pin mat perforated face sheet and the septum material using data obtained at near standard temperatures. The one degree-of-freedom and two degree-of-freedom linings are described as reactive linings.

A 2.5 in (63.5 mm) thick refractory fire brick and a 0.55 in (13.97 mm) thick acoustic ceiling tile were used to validate absorption coefficient measurements. Refractory fire brick refers to a high temperature refractory material commonly used in ceramic furnaces. An existing, qualified traversing microphone method tube was used to measure baseline absorption coefficients for the fire brick and acoustic ceiling tile materials. The traversing microphone tube had a larger diameter than the test fixture being validated, requiring that different samples be used in the two fixtures. Fire brick and acoustic ceiling tile material are not completely homogenous, and the acoustic properties can be presumed to vary slightly between samples. This was a source of possible differences in absorption measurements in the large and small tubes.

5.1. Baseline Signal Characteristics

The fidelity of the acoustic pressure data measured in the two-microphone tube is dependent on the signal-to-noise ratio of the acoustic signals. This is addressed in [2 - 8]. The upper frequency limit of the tube is determined as a function of the tube's inner diameter, limitations of the acoustic source, and limitations of the data acquisition system. For plane wave propagation, the shortest (corresponding to the highest frequency) acoustic wavelength, λ_S, must satisfy

$$\lambda_S \geq 1.706d \tag{61}$$

where d is the inner tube diameter [3]. For this test fixture plane wave propagation extended to just under 4,000 Hz. In the present study testing was performed up to 2,200 Hz for two reasons; the alternate validation traversing microphone test facility with a larger diameter tube supports frequencies only up to 1,800 Hz, and the available acoustic

driver for the new two-microphone test facility performs poorly above 2,200 Hz. The longest wave length λ_L (corresponding to the lowest frequency) is determined by the acoustic source, data acquisition system limitations, and the microphone spacing, s. The ASTM Standard for two-microphone testing [3] recommends that this limit be

$$\lambda_L \leq 100s\,. \tag{62}$$

For this test fixture measurements made below 135 Hz should be disregarded on this basis. Initially, tube performance was investigated from 50 to 2,200 Hz. In order to maintain a high acoustic signal-to-noise ratio across the entire bandwidth, the electronic input signal was segmented into three separate bandwidths. The first spanned from 50 to 300 Hz, the second from 200 to 1,000 Hz, and the third from 800 to 2,200 Hz. The banded noise signals were created using Adobe Audition. White noise was created spanning a bandwidth of 0 to 48 kHz. A fourth order Butterworth band pass filter was applied to limit the bandwidth of each of the three signals. The electrical source signals can be seen in Figs. 15 through 17.

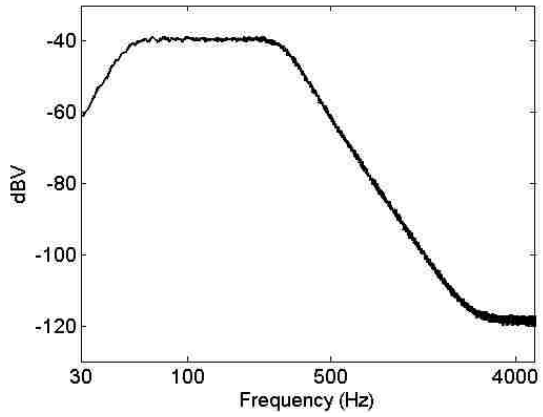

Figure 15. Low frequency bandwidth source signal.

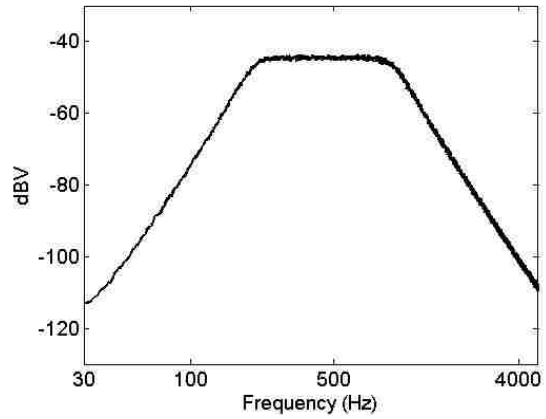

Figure 16. Midrange frequency bandwidth source signal.

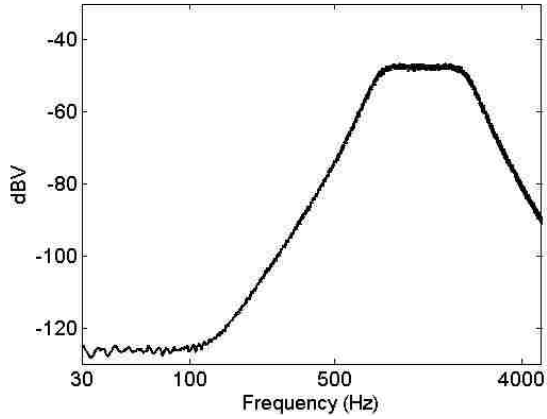

Figure 17. High frequency bandwidth source signal.

The amplitude of the acoustic signals was adjusted using the QSC amplifier. A sufficient signal-to-noise ratio is necessary for data fidelity. Figures 18 and 19 show the noise floor and pressure measurements at each microphone location. The noise floor tends to increase as the frequency decreases.

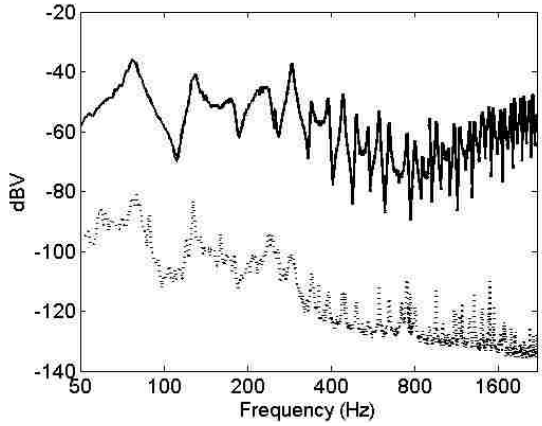

Figure 18. Microphone 1 signal amplitude with noise floor amplitude.
[–Signal Amplitude, ··· Noise Floor Amplitude]

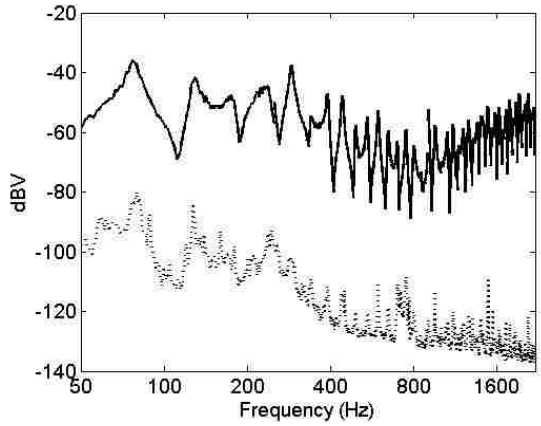

Figure 19. Microphone 2 signal amplitude with noise floor amplitude.
[–Signal Amplitude, ··· Noise Floor Amplitude]

The segmentation and subsequent independent control of the amplitude of the input signal allows some degree of compensation for the rise in the noise floor at lower frequencies. The acoustic signal-to-noise ratio was verified at each microphone location as shown in Figs. 20 and 21. The signal-to-noise ratio tends to decrease as frequency decreases. The ASTM Standard [3] recommends that the acoustic signal be at least 10 dB above the noise floor. This requirement is met at both microphone locations.

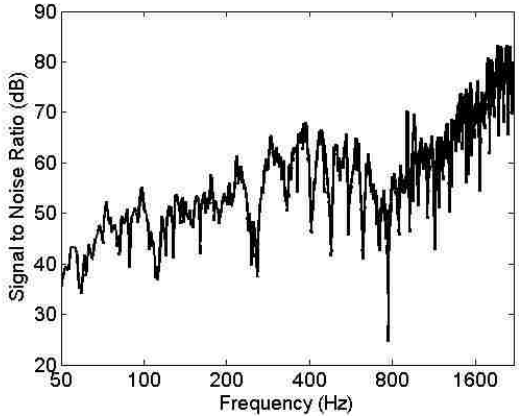

Figure 20. Microphone 1 signal-to-noise ratio.

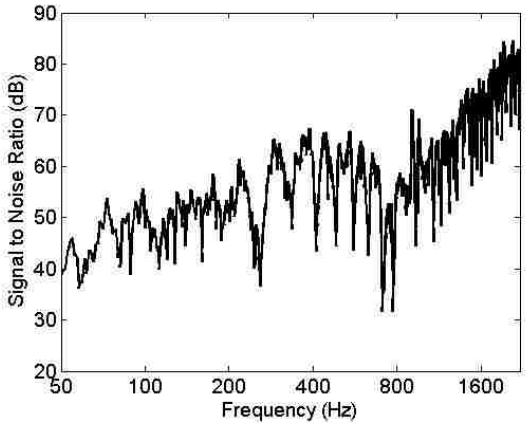

Figure 21. Microphone 2 signal-to-noise ratio.

5.2. Sources of Interference

Measurements made at low frequencies showed errors. Examination of quantities calculated from the raw pressure measurements helped to identify noise sources. Figure 22 shows the magnitude of the reflection coefficient of the one degree-of-freedom acoustic lining sample at room temperature, and Fig. 23 shows the two-microphone method measured impedance of the one degree-of-freedom lining at room temperature. The impedance clearly degraded at lower frequencies. Calculated quantities below 135 Hz violate the constraint given in Eq. (62) and should be disregarded. Calculated

quantities between 135 and 250 Hz also exhibited errors. The impedance became erratic, and reflection coefficient magnitudes greater than unity are physically impossible for a passive element. The close proximity of electrical conduit and fluorescent lighting fixtures often causes interference in this range of frequencies. Electrical interference can add energy artificially to the measured signal causing reflection coefficient magnitudes greater than unity. The interference can also cause the measured electrical signal to misrepresent the physical response of the sensor. This would account for the erratic impedance behavior. Impedance calculations above 250 Hz did not indicate noise interference further strengthening the position that the noise was due to nearby electrical conduit and fluorescent lighting fixtures.

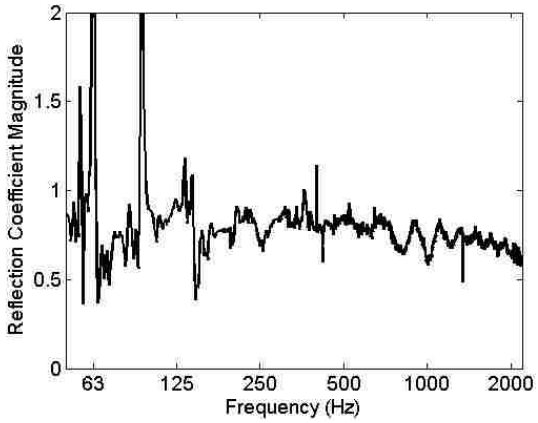

Figure 22. Two-microphone method reflection coefficient magnitude for the one degree-of-freedom lining at room temperature. [– Reflection Coefficient Magnitude, ··· Reflection Coefficient Phase Angle]

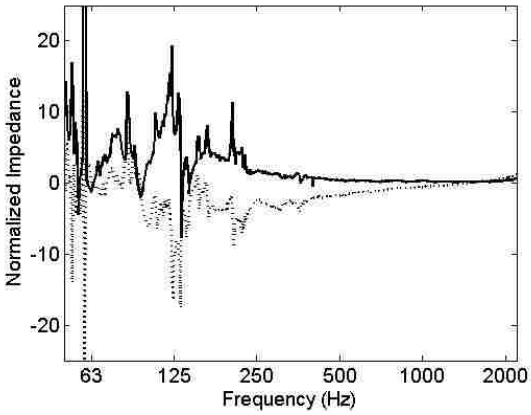

Figure 23. Two-microphone method sample normalized impedance resistance and reactance for the one degree-of-freedom lining at room temperature. [– Two-Microphone Method Normalized Resistance, ··· Two-Microphone Method Normalized Reactance]

5.3. Backing Plug Comparison

Ideally, the backing plug would have an air tight coupling to the tube. This test fixture requires that the sample and the backing plug be inserted a length into the tube. In order to be inserted, the backing plug must have a slip fit with the inner diameter of the tube. This slip fit tolerance has the potential to introduce acoustic loss behind the sample. The tube is 3.65 m long. The speed of sound used to generate the impedance in Fig. 23 was 344.5 m s-1. As the operating frequency decreases, the system acts increasingly more like a pressure vessel. This would tend to intensify the effects of leaks within the system.

In order to characterize losses due to the inserted backing plug, a second completely external backing plug was created. It was a machined cylindrical billet with the same diameter as the outer diameter of the tube. It was attached to the end of the tube using a pipe coupler with rubber gaskets, which created an airtight seal. This alternate backing plug cannot be used at elevated temperatures, because the gaskets would fail.

The impedance of each of the two plugs was measured at room temperature with the two-microphone method. The impedance of the inserted plug was then subtracted from the impedance of the alternate plug. Figure 24 shows the difference in resistance and reactance. Ideally the difference would vanish at each frequency. The results indicate that as frequency decreased, a small but significant difference in resistance and reactance existed down to about 800 Hz. Below 800 Hz the impedance components of the two plugs became significantly different. Above 800 Hz both plugs produced very similar results. This behavior suggests that the acoustic response of the inserted plug may have influenced measured sample impedance. To account for this possibility, impedance measurements were compared with the empirical model for the one degree-of-freedom sample for which the backing plug doubled as the sample backing plate.

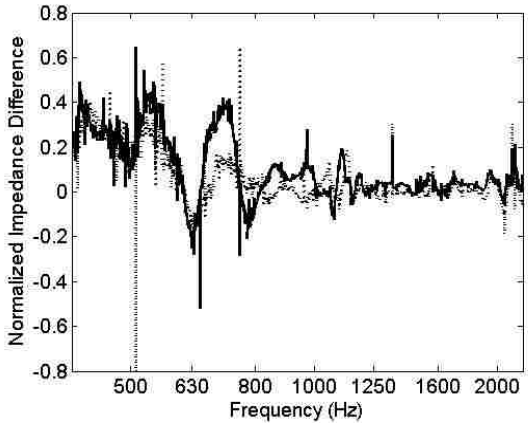

Figure 24. Two-microphone method normalized impedance difference between the externally and internally mounted hard backing plugs at room temperature. [– Two-Microphone Method Normalized Resistance, ··· Two-Microphone Method Normalized Reactance]

5.4. Benchmarking at Room Temperature

Impedance measurements from the new test fixture were compared with measurements from an independent testing method and with empirically based mathematical impedance models. All measurements were taken at room temperature. The two-microphone method was used to obtain impedance and absorption of samples in the new test fixture. Once measurements using the two-microphone method were validated, impedance was calculated using the hybrid two-microphone/finite element method for comparison.

5.4.1. Benchmarking Using the Two-Microphone Method and the Absorption Coefficient

Samples cut from a refractory fire brick commonly used in high temperature furnaces were tested using a traversing microphone impedance tube and the test fixture being validated using the two-microphone method. The traversing microphone impedance tube had a larger diameter than the test fixture being validated, so one sample was cut for each tube. Fire brick has local variations of acoustic properties, and the two samples cut from the brick were similar but not identical. The differences may have affected measured acoustic absorption of each sample. Figure 25 compares the two measurements at room temperature. The trends are acceptably close considering separate samples were used.

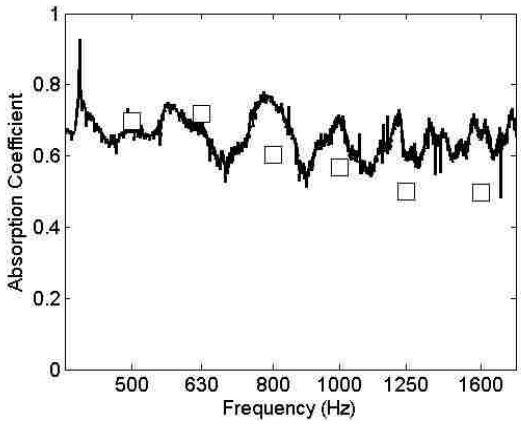

Figure 25. Two-microphone method and traversing microphone method absorption coefficient magnitude of the refractory fire brick at room temperature. [– Two-Microphone Method Absorption Coefficient, ☐ Traversing Microphone Method Absorption Coefficient]

Acoustically absorbent ceiling tile was tested in the same way as the refractory brick. Two separate samples were used to accommodate the differing tube diameters, so again the samples differed slightly. The results are shown in Fig. 26. The two methods yielded similar trends again noting that separate samples were tested.

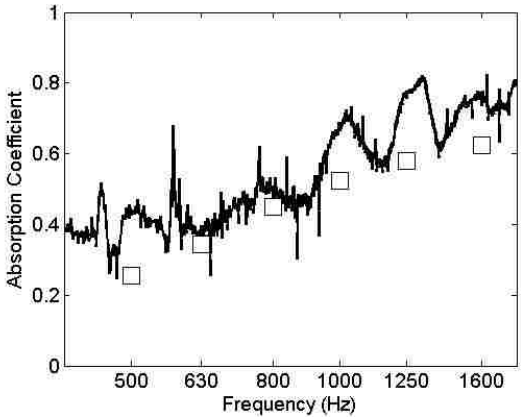

Figure 26. Two-microphone method and traversing microphone method absorption coefficient magnitude of the acoustic tile at room temperature. [– Two-Microphone Method Absorption Coefficient, ☐ Traversing Microphone Method Absorption Coefficient]

5.4.2. Benchmarking Using the Two-Microphone Method and Impedance Models

Impedance was measured for the one and two degree-of-freedom lining samples using the two-microphone method. Room temperature impedance data were compared with an empirically based impedance lining model for each of the two samples. The two degree-of-freedom lining included a hard backing plate. The one degree-of-freedom lining used for validation, however, had no hard backing plate. In this case the backing plug acted as the lining backing plate. The backing plug had a complex reflection coefficient shown in Fig. 27. This behavior indicates that there was a loss in the magnitude of the reflected wave that was relatively constant with frequency. The phase shift was frequency dependent. For validation purposes the empirical one degree-of-freedom model should be extended to include the acoustic behavior of the backing plug.

The impedance of a one degree-of-freedom lining is a combination of the cavity impedance and face sheet impedance. The hard backing plate is assumed to have perfect acoustic reflection. Figure 27 demonstrates that this is not the case when the backing plug replaces the lining hard backing plate. A modification to the lining model can be made to accommodate the nonrigid impedance of the hard backing plug. Figure 28 shows a cutaway schematic of the one degree-of-freedom lining with the hard backing plug acting as the hard backing plate with a local coordinate system.

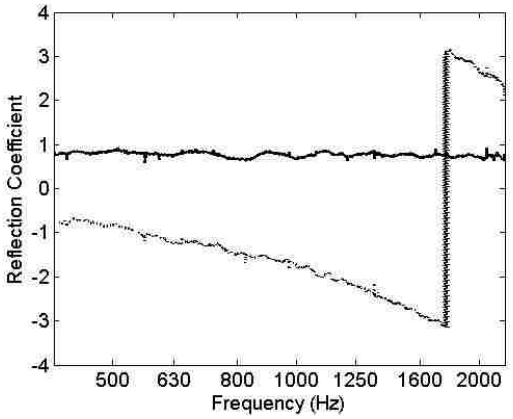

Figure 27. Two-microphone method reflection coefficient magnitude and phase angle for the hard backing plug at room temperature. [– Two-Microphone Method Reflection Coefficient Magnitude, ··· Two-Microphone Method Reflection Coefficient Phase Angle]

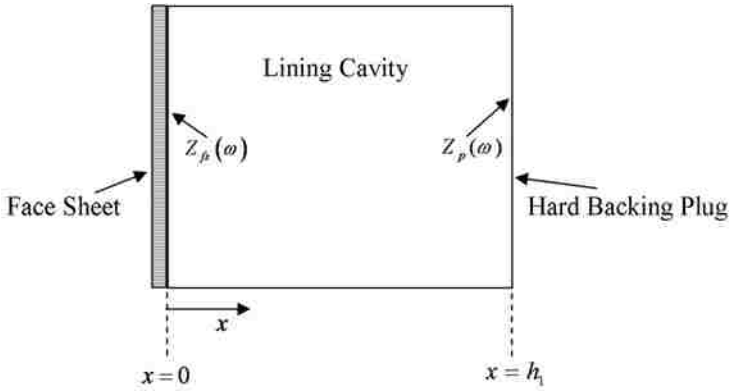

Figure 28. Cutaway schematic of the one degree-of-freedom lining with the hard backing plug acting as the lining hard backing plate.

The backing plane of the lining cavity is the hard backing plug. It has an impedance of $Z_p(\omega)$, which is a measured quantity. This impedance is required to find the cavity impedance at the face sheet given the termination impedance at the hard backing plug. The coordinate x is interpreted as the distance from the face sheet. The hard backing plug termination is at $x = h_1$. Acoustic pressure in the cavity is

$$P_c(\omega, x) = P_{rc}(\omega) e^{i(-kx)} + P_{lc}(\omega) e^{i(kx)} \tag{63}$$

where $P_c(\omega,x)$ is the pressure field in the cavity and $P_{rc}(\omega)$ and $P_{lc}(\omega)$ are the amplitudes of the right and left running acoustic pressure waves in the cavity. The corresponding particle velocity is

$$u_c(\omega,x)=\frac{1}{\rho c}\left(P_{rc}(\omega)e^{i(-kx)}-P_{lc}(\omega)e^{i(kx)}\right). \tag{64}$$

At the backing plug where $x=h_1$ a measured termination impedance, $Z_p(\omega)$, is available and provides a means of determining the complex ratio $P_{lc}(\omega)/P_{rc}(\omega)$ denoted by $R_{fs}(\omega)$ and interpreted as the reflection coefficient phased with respect to the origin at the face sheet. Equations (63) and (64) and the definition of impedance provide the relationship:

$$\rho c\frac{1+\dfrac{P_{lc}(\omega)}{P_{rc}(\omega)}e^{2i(kh_1)}}{1-\dfrac{P_{lc}(\omega)}{P_{rc}(\omega)}e^{2i(kh_1)}}=\rho c\frac{1+R_{fs}(\omega)e^{2i(kh_1)}}{1-R_{fs}(\omega)e^{2i(kh_1)}}=Z_p(\omega). \tag{65}$$

Equation (65) is solved for $R_{fs}(\omega)$ to yield

$$R_{fs}(\omega)=\frac{\dfrac{Z_p(\omega)}{\rho c}-1}{\dfrac{Z_p(\omega)}{\rho c}+1}e^{-2i(kh_1)}. \tag{66}$$

The impedance represented by the cavity at the face sheet is then

$$Z_{cfs}(\omega)=\rho c\frac{1+R_{fs}(\omega)}{1-R_{fs}(\omega)}. \tag{67}$$

With the lumped parameter impedance for the face sheet, $Z_{fs}(\omega)$, representing the ratio of pressure drop across the face sheet to particle velocity through the face sheet, the lining model is then

$$Z(\omega) = Z_{fs}(\omega) + \rho c \frac{1 + R_{fs}(\omega)}{1 - R_{fs}(\omega)}. \tag{68}$$

In the case when the termination tends toward perfect reflection $Z_p(\omega) \to \infty$, and $R_{fs}(\omega) \to e^{-2ikh_1}$. The lining impedance is then the usual one degree-of-freedom model

$$Z(\omega) = Z_{fs}(\omega) - i\rho c \cot(kh_1) \tag{69}$$

where $Z_{fs}(\omega)$ is generally specified with empirical data. Equation (68) provides the extended model, and, with measured termination $Z_p(\omega)$ available, the usual model can be supplemented to account for the backing plug impedance.

Measured impedance for the backing plug is also obtained at elevated temperatures to improve the one degree-of-freedom impedance model in these cases. The lining model for the two degree-of-freedom lining need not be supplemented, because the backing plate is part of the sample.

Room temperature impedance data was compared with the supplemented empirically based impedance model for the one degree-of-freedom lining. This is shown in Fig. 29. The comparison is generally good. Resistance was predicted quite well, while the modeled reactance was less negative uniformly over the frequency bandwidth. This result was not unexpected because the empiricism of the model is based on a pin mat perforated composite face sheet, while the one degree-of-freedom lining uses a drilled titanium face sheet.

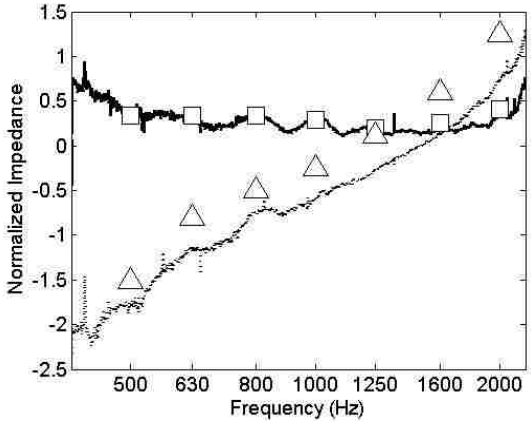

Figure 29. Two-microphone method normalized impedance and modeled normalized impedance for the one degree-of-freedom lining at room temperature. [··· Two-Microphone Method Normalized Reactance, ☐ Modeled Normalized Resistance, △ Modeled Normalized Reactance]

The two degree-of-freedom lining was also tested at room temperature using the two-microphone method. This lining had an inserted septum made of a proprietary woven material. Figure 30 compares the empirical model impedance with the measured impedance. Comparison is very good for resistance. This is not unexpected, because in this case the empirical model is specifically for the pin mat perforated composite face sheet. Comparison for reactance is not quite as good, particularly in the mid-frequency range. In this type of lining with the inserted weave septum, there is necessarily some imprecision in specification of the septum insertion depth.

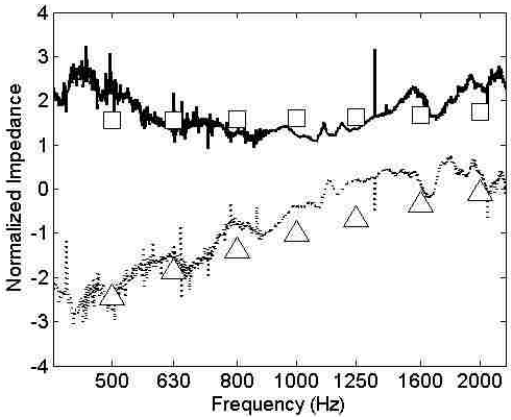

Figure 30. Two-microphone method normalized impedance and modeled normalized impedance for the two degree-of-freedom lining at room temperature. [··· Two-Microphone Method Normalized Reactance, □ Modeled Normalized Resistance, △ Modeled Normalized Reactance]

The agreement between quantities measured in this test fixture and reference data is sufficient evidence that the two-microphone impedance tube produces results commensurate with existing and accepted measurement methods within the frequency range of interest using the two-microphone method.

5.4.3. Benchmarking Using the Hybrid Method

At room temperature the traditional two-microphone impedance calculation method and impedance calculation using the hybrid two-microphone/finite element propagation method should be equivalent. The one degree and two degree-of-freedom linings were tested at room temperature. Impedance was measured using the traditional two-microphone method at the location of Thermocouple Number 8. The finite element propagation method was then used to transfer the impedance from the Thermocouple Number 8 location to the sample face. This allows direct comparison of the two-microphone method and the hybrid two-microphone/finite element method. The results

show nearly identical results as shown in Fig. 31 and Fig. 32. This validates the use of the finite element method with transition plane impedance data obtained using this test fixture.

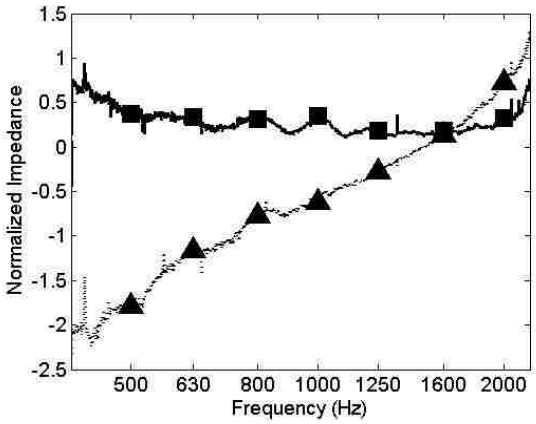

Figure 31. Two-microphone method normalized impedance and hybrid method normalized impedance for the one degree-of-freedom lining at room temperature. [··· Two-Microphone Method Normalized Reactance, ■ Hybrid Model Normalized Resistance, ▲ Hybrid Model Normalized Reactance]

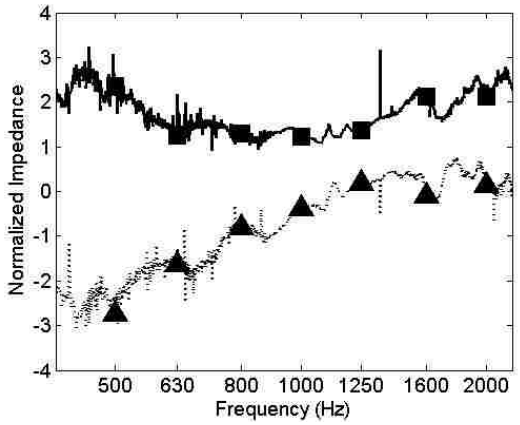

Figure 32. Two-microphone method normalized impedance and hybrid method normalized impedance for the two degree-of-freedom lining at room temperature. [··· Two-Microphone Method Normalized Reactance, ■ Hybrid Model Normalized Resistance, ▲ Hybrid Model Normalized Reactance]

This section has demonstrated that the test fixture developed for this investigation produces sample impedance measurements that are in reasonable agreement with measurements obtained by accepted testing methods and models. Absorption coefficient measurements taken with a traversing microphone method impedance tube were similar to measurements taken with this test fixture. Impedance measurements taken with this test fixture showed good agreement with empirically based impedance models for acoustic lining samples. The hybrid two-microphone/finite element method produced impedances nearly identical to results calculated using the classical two-microphone method at room temperature. This allows optimism that measurements at elevated temperatures can be made successfully.

6. EXPERIMENTAL RESULTS AT ELEVATED TEMPERATURES

In this section elevated temperature impedance measurements will be compared with room temperature measurements for four samples. In addition, measured high temperature impedance determined using the empirical impedance models is compared to measured impedance for the one and two degree-of-freedom linings.

6.1. High Temperature Impedance Results Compared with Room Temperature Impedance

The one degree-of-freedom lining was inserted into the tube, and the system was heated until the sample face reached 319 °C. Heating one end of the tube with the other end held at room temperature generated a temperature profile that was a function of the nondimensional position x along the length of the tube. Seven thermocouples measured temperatures along the centerline of the tube as depicted in Fig. 9. Temperature measured at the tube centerline was taken to represent the temperature of the entire cross-section. This ignored potential convective behavior and temperature variation with tube radius that may have existed within the tube. Figure 33 shows thermocouple temperatures. The finite element method uses a spline curve fit of the discrete temperature data points in its calculations. The interpolated temperature profile can also be seen in Fig. 33. Impedance was measured in the room temperature section of the tube and transferred using the finite element code to the sample face. The results can be seen in Fig. 34 compared to measured room temperature impedance. Increased temperature had a clear effect on the sample impedance. Resistance increased at low frequency, and the reactance was significantly more negative.

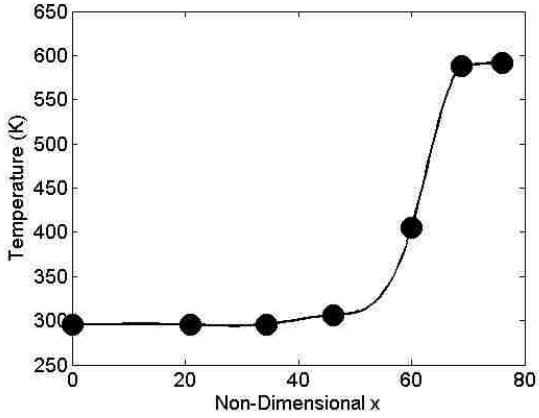

Figure 33. Thermocouple temperature measurements and spline fit temperature profile for the one degree-of-freedom lining at 319 °C. [● Measured Thermocouple Temperature, – Hybrid Method Spline Fit Temperature Profile]

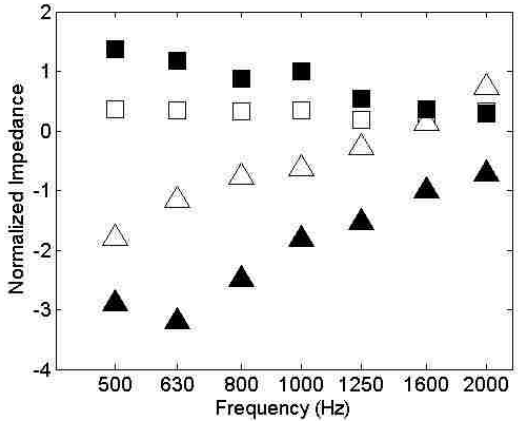

Figure 34. Room temperature hybrid method normalized impedance and elevated temperature hybrid method normalized impedance at 319 °C for the one degree-of-freedom lining. [□ Room Temperature Normalized Resistance, △ Room Temperature Normalized Reactance, ■ 319 °C Normalized Resistance, ▲ 319 °C Normalized Reactance]

The two degree-of-freedom lining is made from composite materials that cannot survive temperatures as high as the one degree-of-freedom lining. The maximum testing temperature for the two degree-of-freedom lining was limited to 101 °C at the sample face. Figure 35 shows the thermocouple temperature data points and spline fit curve.

Impedance was measured in the room temperature section of the tube and transferred to the sample face using the finite element model. Figure 36 shows the results.

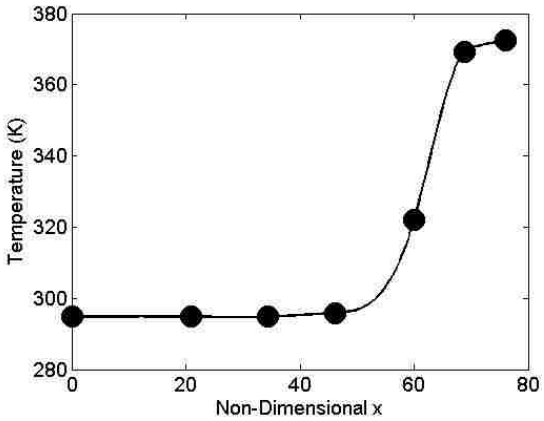

Figure 35. Thermocouple temperature measurements and spline fit temperature profile for the two degree-of-freedom lining at 101 °C. [● Measured Thermocouple Temperature, – Hybrid Method Spline Fit Temperature Profile]

In this case temperature had little effect on measured sample impedance. This result must be viewed considering the relatively small difference between room temperature and the elevated temperature at the sample.

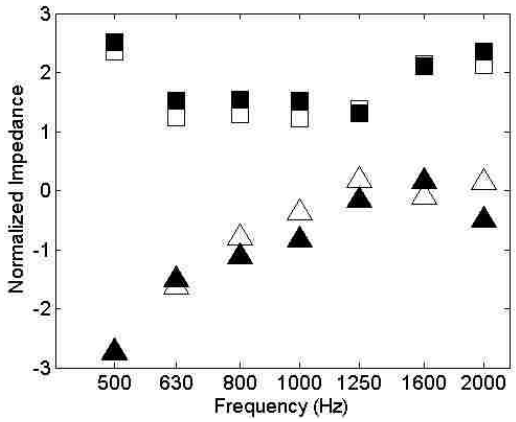

Figure 36. Room temperature hybrid method normalized impedance and elevated temperature hybrid method normalized impedance at 101 °C for the two degree-of-freedom lining. [□ Room Temperature Normalized Resistance, △ Room Temperature Normalized Reactance, ■ 101 °C Normalized Resistance, ▲ 101 °C Normalized Reactance]

The refractory fire brick sample can withstand temperatures well beyond the melting point of the steel tube and the thermocouple instrumentation. The extreme temperature limits were not attempted, however impedance measurements for the fire brick sample were obtained at 394 °C. The thermocouple data points and temperature profile are shown in Fig. 37. The impedance of the sample was determined from the measured pressure data, and the absorption coefficient was calculated. The comparison of room temperature and elevated temperature measurements is shown in Fig. 38. The absorption coefficient decreased at lower frequencies, but in general the behavior was similar at the two temperatures.

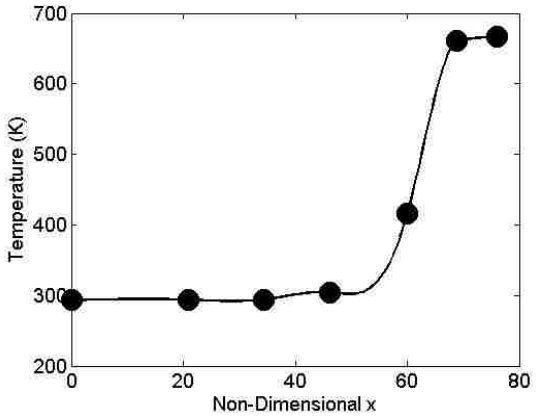

Figure 37. Thermocouple temperature measurements and spline fit temperature profile for the fire brick at 394 °C. [● Measured Thermocouple Temperature, – Hybrid Method Spline Fit Temperature Profile]

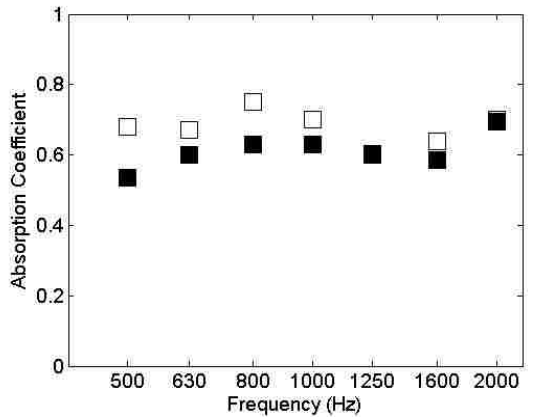

Figure 38. Absorption coefficient of the fire brick sample at room temperature and 394 °C. [□ Absorption Coefficient at room temperature, ■ Absorption Coefficient at 394 °C]

The acoustic tile sample was heated to 143 °C. Figure 39 shows the associated temperature data points and profile. The absorption coefficient was calculated from the measured impedance. The variation of absorption coefficient with frequency exhibited the same general trend at both elevated and room temperatures. These results are shown in Fig. 40.

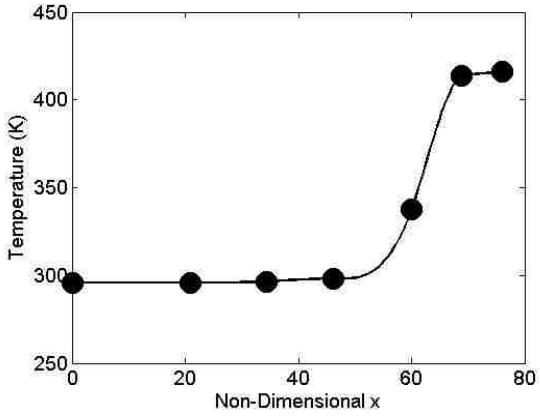

Figure 39. Thermocouple temperature measurements and spline fit temperature profile for the acoustic tile at 143 °C. [● Measured Thermocouple Temperature, – Hybrid Method Spline Fit Temperature Profile]

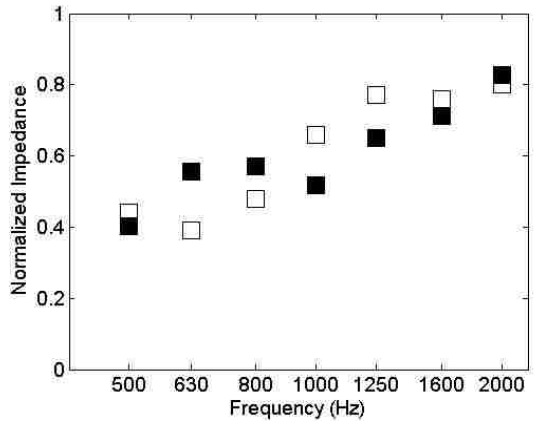

Figure 40. Absorption coefficient of the acoustic tile sample at room temperature and 143 °C. [□ Absorption Coefficient at room temperature, ■ Absorption Coefficient at 143 °C]

6.2. High Temperature Impedance Results Compared with Impedance Models

The proprietary impedance models for the one degree-of-freedom and two degree-of-freedom samples used in this investigation were developed using empirical data taken at near standard temperatures. The models include the effect of temperature, but not beyond the range used in the measurements taken during this investigation. The models

are therefore considered to be ad hoc. Impedance for the one degree-of-freedom lining was measured at 319 °C. It was then modeled with the proprietary impedance model at the elevated temperature. In order to see how impedance is expected to change with temperature, Fig. 41 is included to show modeled impedance for the one degree-of-freedom lining at room temperature and at 319 °C.

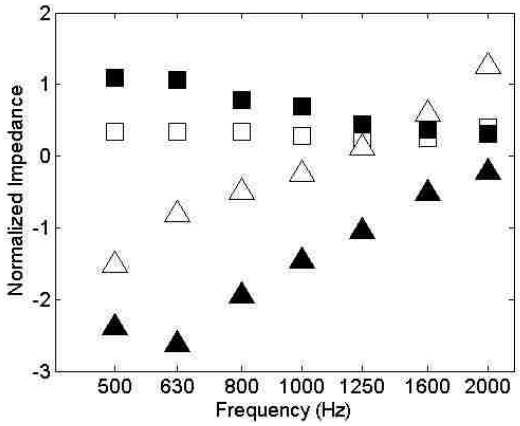

Figure 41. Ad hoc modeled normalized impedance for the one degree-of-freedom lining at room temperature and 319 °C. [□ Modeled Normalized Resistance at Room Temperature, △ Modeled Normalized Reactance at Room Temperature, ■ Modeled Normalized Resistance at 319 °C, ▲ Modeled Normalized Reactance at 319 °C]

Increasing temperature increased the modeled lining resistance and made the modeled reactance more negative. The comparison shown in Fig. 41 appears to be quite similar to the comparison of Fig. 34, which is based on measured impedance data.

Figure 42 compares measured impedance data at elevated temperature with ad hoc modeled impedance data. The quality of the comparison is somewhat better than that found in the room temperature case shown in Fig. 29. The measured resistance showed

close agreement with the modeled resistance, and the modeled reactance was consistently somewhat less negative over the frequency range. Since in a one degree-of-freedom lining model cavity reactance should be relatively well modeled for temperature effects, these results suggest that the empiricism of the model misses the elevated temperature effect on mass reactance of the face sheet to some extent. Temperature measurements made within and behind the lining indicate that there is a decreasing temperature profile within the lining. This is not captured in the empirical model.

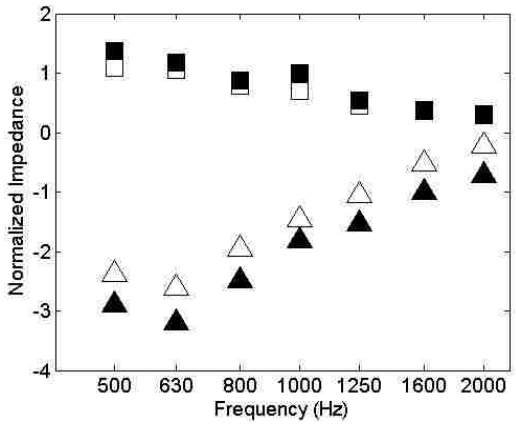

Figure 42. Hybrid method normalized measured impedance and ad hoc modeled normalized impedance for the one degree-of-freedom lining at 319 °C. [□ Modeled Normalized Resistance, △ Modeled Normalized Reactance, ■ Measured Normalized Resistance, ▲ Measured Normalized Reactance]

Impedance for the two degree-of-freedom lining was measured at 101 °C. It was also modeled using the proprietary impedance model extrapolated to temperatures beyond the intended range. Figure 43 compares the modeled impedances at room temperature and 101 °C. Based on the projections of the model there was little difference to be expected between measured impedance at room temperature and at elevated

temperature, and this was consistent with the measured impedance results shown in Fig. 36. This was due at least in part to the relatively small change in temperature used for the two degree-of-freedom tests. As with the one degree-of-freedom lining model the modeled resistance increased, and the modeled reactance became more negative.

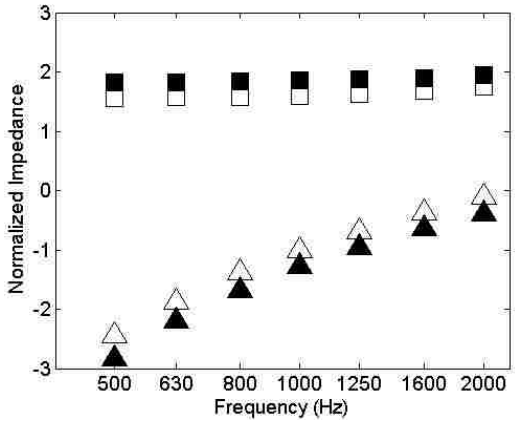

Figure 43. Ad hoc modeled normalized impedance for the two degree-of-freedom lining at room temperature and 101 °C. [□ Modeled Normalized Resistance at Room Temperature, △ Modeled Normalized Reactance at Room Temperature, ■ Modeled Normalized Resistance at 101 °C, ▲ Modeled Normalized Reactance at 101 °C]

Figure 44 compares measured impedance with the ad hoc modeled impedance. The quality of this comparison was not quite as good as in the case of the one degree-of-freedom lining shown in Fig. 42. The probability of a nonuniform temperature distribution in the lining is perhaps even more significant in this sample because the lining is considerably thicker than the one degree-of-freedom lining. The effect of nonuniform temperature is not captured in the lining model.

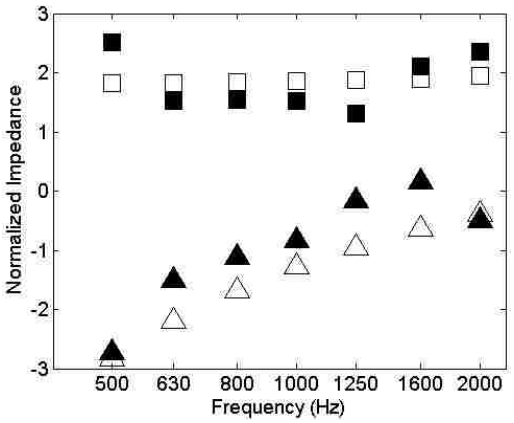

Figure 44. Hybrid method normalized impedance and ad hoc modeled normalized impedance for the two degree-of-freedom lining at 101 °C. [□ Modeled Normalized Resistance, △ Modeled Normalized Reactance, ■ Measured Normalized Resistance, ▲ Measured Normalized Reactance]

7. TEMPERATURE RELATED UNCERTAINTY

Speed of sound and density are each a function of the temperature in the tube. Unobserved variation in ambient temperature and error in thermocouple temperature measurement will contribute to error in the determination of measured impedance. In comparisons of measured and modeled impedance, temperature uncertainties also contribute to uncertainties in modeled impedance. Effects of temperature on measured and modeled impedance are explored here.

Temperature measurements from the test fixture are required at multiple stages in the impedance calculation process. The two-microphone method requires a constant speed of sound between the microphone measurement point and the plane where impedance is calculated. The finite element model requires temperature data points in the heated section of the tube. A system temperature measurement uncertainty level of ± 1.3 °C is significant enough to cause variation in the impedance calculation. This uncertainty arises from a combination of sensor uncertainty, data acquisition resolution, and observed fluctuations.

7.1. Sensitivity of Lining Impedance Model to System Temperature Uncertainty

Temperature is an input for both the one and two degree-of-freedom lining impedance models. Since these models were used as a benchmark for the measured impedance data at room temperature, their response to temperature variation was important. The models were also used on an ad hoc basis to benchmark at elevated temperatures. The ad hoc model sensitivity to temperature variation was assumed to be

represented by the room temperature sensitivity. Figures 45 and 46 show modeled impedance at room temperature for the one and two degree-of-freedom linings, respectively, with uncertainty bounds due to temperature uncertainty. There was very little sensitivity of modeled impedance to system temperature uncertainty at room temperature where the models are most accurate. Upper and lower uncertainty bounds that appear as single lines in Figs. 45 and 46 are indistinguishable. It was safely concluded that impedance model sensitivity to temperature uncertainties was small.

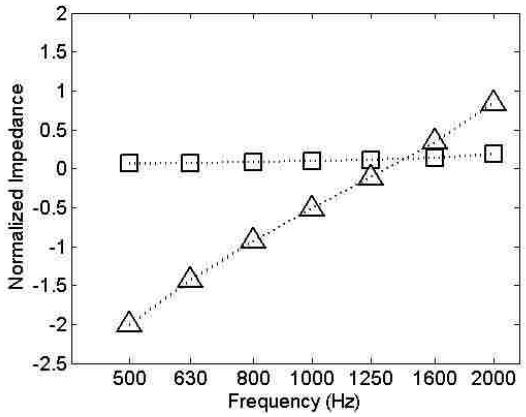

Figure 45. Modeled normalized impedance for the one degree-of-freedom lining at room temperature with uncertainty bounds. [□ Modeled Normalized Resistance, △ Modeled Normalized Reactance, ··· Measured Normalized Impedance Uncertainty Bounds]

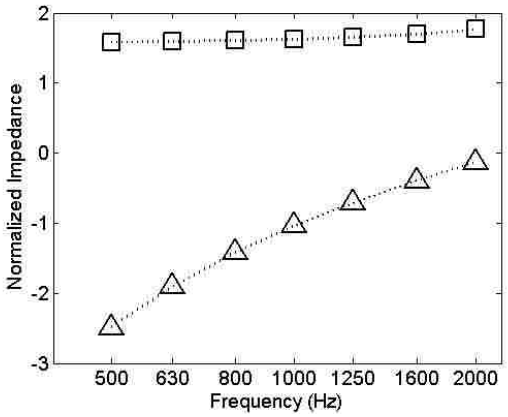

Figure 46. Modeled normalized impedance for the two degree-of-freedom lining at room temperature with uncertainty bounds. [□ Modeled Normalized Resistance, △ Modeled Normalized Reactance, ··· Measured Normalized Impedance Uncertainty Bounds]

7.2. Sensitivity of Calculated Impedance Due to System Temperature Uncertainty in the Two-Microphone Method Impedance Calculations

The finite element method requires source plane impedance as an input. This test fixture uses the impedance calculated from the two-microphone method at the cross-section of the tube located at Thermocouple 8 (Fig. 9) as the input for the finite element method. This plane is referred to as the transition plane. Measured impedance at the transition plane is strongly influenced by the speed of sound, and therefore by the temperature, within the tube. Figures 47 and 48 show the measured transition plane impedance, with the associated impedance uncertainty bounds due to the temperature uncertainty, for the one degree-of-freedom lining at room temperature. The results represent the nominal (measured) temperature with an error of ± 1.3 °C applied uniformly in the two-microphone method. The bandwidth shown in Figs. 47 and 48 is limited to emphasize the most sensitive portion of the impedance data. Uncertainty in the temperature clearly produces a measurable sensitivity in transition plane impedance. This

sensitivity influences the finite element model input transition plane impedance and will propagate through to the final sample impedance.

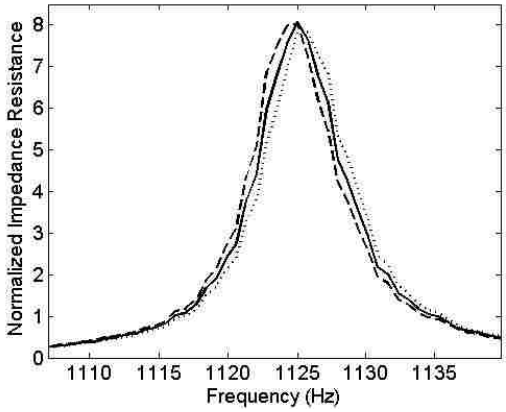

Figure 47. Measured normalized resistance at plane for the one degree-of-freedom lining at room temperature with uncertainty bounds.
[--- Normalized Impedance Upper Bound, – Normalized Impedance Nominal, ··· Normalized Impedance Lower Bound]

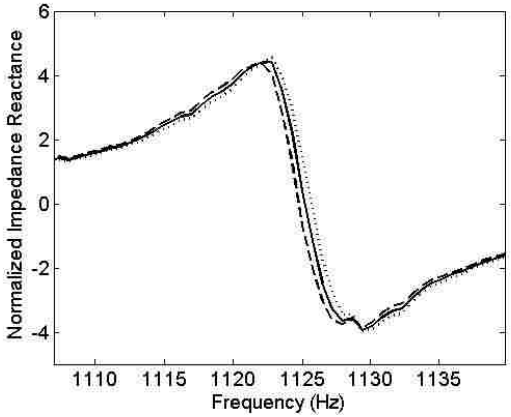

Figure 48. Measured normalized reactance at plane for the one degree-of-freedom lining at room temperature with uncertainty bounds.
[--- Normalized Impedance Upper Bound, – Normalized Impedance Nominal, ··· Normalized Impedance Lower Bound]

Figures 47 and 48 demonstrate the effect of system temperature uncertainty on the transition plane impedance, which is used as an input by the finite element method.

Figure 49 shows the effects of the transition plane impedance uncertainties propagated through the finite element model. The finite element model used to create the impedance data in Fig. 49 uses the nominal (measured) temperature profile for each calculation. The result is the isolation of the effects on sample impedance of system temperature uncertainty included only in the two-microphone method calculations.

To assess the total effect of system temperature uncertainty on sample impedance, the temperature variation must be included in both the transition plane impedance calculation and the finite element propagation temperature profile. Figure 50 shows the sample impedance of the one degree-of-freedom lining at room temperature with uncertainty bounds including system temperature uncertainties throughout the impedance calculation. There was only a slight increase in the impedance uncertainty bounds as compared to Fig 49. This comparison made it clear that the sample impedance uncertainty due to system temperature uncertainty was primarily a consequence of the transition plane impedance calculation.

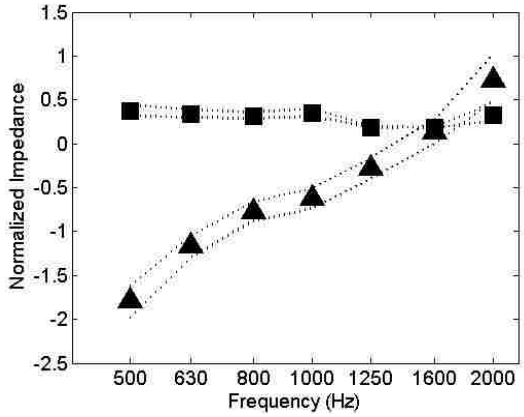

Figure 49. Hybrid method normalized impedance for the one degree-of-freedom lining at room temperature with uncertainty bounds due to system temperature uncertainty in the two-microphone method. [■ Measured Normalized Resistance, ▲ Measured Normalized Reactance, ··· Measured Normalized Impedance Uncertainty Bounds]

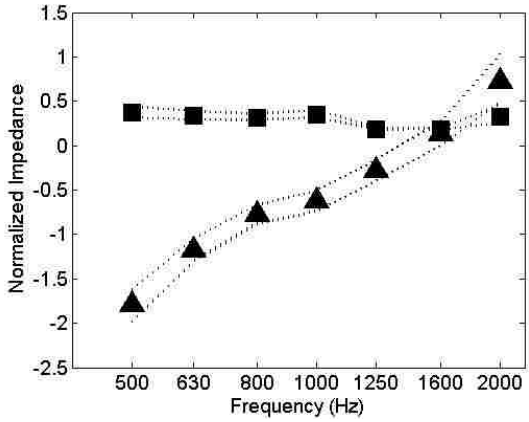

Figure 50. Hybrid method normalized impedance for the one degree-of-freedom lining at room temperature with uncertainty bounds due to system temperature uncertainty in the two-microphone method and finite element method models. [■ Measured Normalized Resistance, ▲ Measured Normalized Reactance, ··· Measured Normalized Impedance Uncertainty Bounds]

7.3. High Temperature Impedance Results Including System Temperature Uncertainty Compared with Impedance Models

The numerical impedance models used in this study are empirically based, implying that there is some degree of experimental uncertainty included in the models.

Experimental uncertainty also affects the impedance calculated with this test fixture. It is important to consider these uncertainties when comparing the two impedance data sets. It has been shown that the impedance models are relatively unaffected by the system temperature uncertainty. The measured impedance, however, is affected by the system temperature uncertainty. Figure 42 shows the elevated temperature one degree-of-freedom lining impedance calculation compared to the empirically based impedance model. Figure 51 shows the same impedance, with uncertainty bounds included for the measured impedance. Uncertainty bounds are not shown for the modeled impedance, because, as shown in Fig. 45, modeled impedance uncertainty due to system temperature uncertainty is small relative to the plotted scale. The uncertainty bounds encapsulate almost all of the modeled resistance. The modeled reactance was still less negative than the measured impedance with uncertainty bounds indicating that the empiricism of the mass reactance in the model was not valid for this lining at elevated temperatures.

Figure 52 shows impedance data similar to those in Fig. 44 for the two degree-of-freedom lining. The uncertainty bounds are now included for the measured impedance. The comparison of the resistance between the modeled and measured impedance is significantly improved when the effects of system temperature uncertainty are included. The uncertainty bounds of the reactance are tight below 1,600 Hz, showing little improvement.

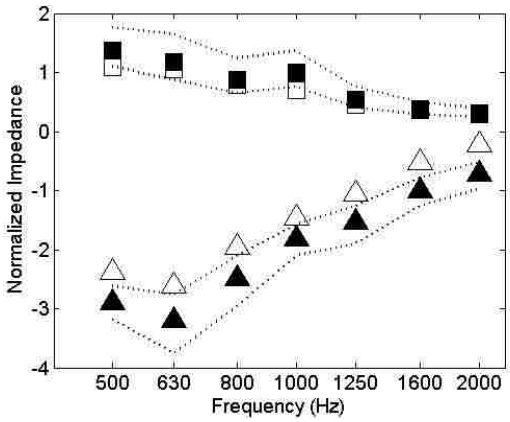

Figure 51. Hybrid method normalized impedance and modeled normalized impedance for the one degree-of-freedom lining at 319 °C with uncertainty bounds. [□ Modeled Normalized Resistance, △ Modeled Normalized Reactance, ■ Measured Normalized Resistance, ▲ Measured Normalized Reactance, ··· Measured Normalized Impedance Uncertainty Bounds]

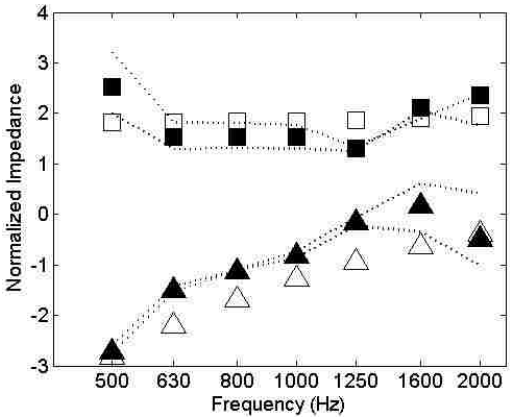

Figure 52. Hybrid method normalized impedance and modeled normalized impedance for the two degree-of-freedom lining at 101 °C with uncertainty bounds. [□ Modeled Normalized Resistance, △ Modeled Normalized Reactance, ■ Measured Normalized Resistance, ▲ Measured Normalized Reactance, ··· Measured Normalized Impedance Uncertainty Bounds]

8. CONCLUSIONS

This study sought to develop a method to measure the normal incidence acoustic impedance of a sample at elevated temperatures using microphones at room temperature. The result was a test fixture based on the two-microphone impedance measurement method and augmented by a finite element model that compensates for the stratified temperature profile along the length of the tube.

Impedance at a cross-section of the tube can be calculated using traditional two-microphone impedance tube methods. These methods are valid at locations within the tube where the temperature at the cross-section is the same as the temperature at the microphone locations. The finite element method transfers impedance measured at the transition plane using the two-microphone method along the length of the tube to the sample face. It uses an iterative procedure to determine the sample impedance. The method was validated analytically using several approaches. One approach used direct calculation of acoustic power absorption coefficients with a uniform temperature distribution along the length of the tube. Another determined termination impedance for a known source impedance in the case of nonuniform temperature. In these cases the "target" source impedance had previously been determined by direct calculation from specified termination impedance.

A two-microphone method impedance tube was constructed to create the conditions the necessary conditions for application of the finite element method. The tube is sufficiently long to allow the microphones to remain at room temperature while the

sample is at elevated temperatures, and it was instrumented to allow measurement of the temperature profile along the length of the tube. The tube was validated at room temperature using several methods. One method compared absorption coefficient data measured using the traversing microphone method with absorption coefficient data measured using the two-microphone method. These measurements were taken at room temperature. Another method compared impedance measured at room temperature with the two-microphone method with modeled impedance for samples of one degree-of-freedom and two degree-of-freedom reactive linings. In each of these cases measurements agreed well with model predictions. To validate the use of the finite element method with the test fixture, room temperature impedance measurements taken using the two-microphone method were compared with impedance measurements taken using the hybrid two-microphone/finite element model. The results were nearly identical.

Absorption coefficients of fire brick and acoustic tile samples were measured at both room and elevated temperatures. Some variation with temperature was observed, but in general the trends were similar as temperature increased. The impedances of the one and two degree-of-freedom lining samples were measured at room and elevated temperatures. The one degree-of-freedom lining showed a significant change in impedance with temperature. The resistance increased, and the reactance became much more negative. The impedance of the two degree-of-freedom lining showed little change with temperature over a limited temperature range.

Measured impedance data for the one and two degree-of-freedom reactive linings were compared with the impedance models at both room and elevated temperatures. The room temperature impedance showed reasonable agreement for both linings. At elevated temperature, the one degree-of-freedom lining model no longer accurately predicted the impedance. The two degree-of-freedom lining model showed reasonable agreement with the measured impedance at elevated temperature, though again, it is noted that the temperature range was limited.

Temperature was measured along the centerline of the tube. Some variation in the temperature profile was expected due to equipment measurement uncertainties and small physical temperature variations. Several calculations were made to investigate the potential effects of these temperature uncertainties. The impedance models showed very little sensitivity to temperature. Impedance at the transition plane did exhibit a noticeable sensitivity to temperature, and appeared to be the primary source of uncertainty error in the sample impedance calculation using the finite element method. Including the effects of temperature uncertainty in the high temperature impedance analysis demonstrated the need for accurate temperature measurements with strong steady state temperature control.

The result of this study was a test fixture and calculation method that can measure the normal incidence impedance of a sample at temperatures that can differ significantly from the temperature at the microphones. The fixture and calculation method were validated at room temperature using independent methods.

9. REFERENCES

[1] ASTM-C384-04, Impedance and absorption of acoustical materials by the impedance
tube method.

[2] M. G. Jones and P. E. Stiede, Comparison of methods for determining specific acoustic impedance. *Journal of the Acoustical Society of America* 101(5) (1997) 2694-2704.

[3] ASTM-E1050-08, Impedance and absorption of acoustical materials using a tube, two microphones, and a digital frequency analysis system.

[4] J. Y. Chung and D. A. Blaser, Transfer function method of measuring in-duct acoustic properties. I. theory. *Journal of the Acoustical Society of America* 68(3) (1980) 907-913.

[5] J. Y. Chung and D. A. Blaser, Transfer function method of measuring in-duct acoustic properties. II. Experiment *Journal of the Acoustical Society of America* 68(3) (1980) 914-921.

[6] A. F. Seybert and D. F. Ross, Experimental determination of acoustic properties using a two-microphone random-excitation technique. *Journal of the Acoustical Society of America*, 61(5) (1977) 1362-1370.

[7] F. J. Fahy, Rapid method for the measurement of sample acoustic impedance in a standard wave tube. *Journal of Sound and Vibration* 97(1) (1984) 168-170.

[8] T. Schultz, L. N. Cattafesta III, T. Nishida, M. Sheplak, Uncertainty analysis of the two-microphone method for acoustic impedance testing. *8th AIAA/CEAS Aeroacoustics Conference* (2002) 2002-2465.

[9] L. E. Kinsler, A. R. Frey, A. B. Coppens, J. V. Sanders, *Fundamentals of Acoustics*, John Wiley & Sons, Inc. 2000.

[10] A. Kapur, A. Cummings, and P. Mungur, Sound propagation in a combustion can with axial temperature and density gradients. *Journal of Sound and Vibration* 25(1) (1971) 129-138.

[11] A. Cummings, Ducts with axial temperature gradients: an approximate solution for sound transmission and generation. *Journal of Sound and Vibration* 51(1) (1977) 55-67.

[12] I. Danda Roy and W. Eversman, Far field calculations for turbofan noise. *AIAA Journal* 39(12) (2001) 2255-2261.

[13] W. Eversman, A reverse flow theorem and acoustic reciprocity in compressible potential flow in ducts. *Journal of Sound and Vibration* 246(1) (2001) 71-95.

[14] E. Listerud and W. Eversman, Finite element modeling of acoustics using higher order elements. Part I: non-uniform duct propagation. *Journal of Computational Acoustics* 12(3) (2004) 397-429.

[15] J. A. Nelder and R. Mead, A Simplex method for function minimization. *Computer Journal* 7 (1965), 308-313.

VITA

David R. Burd, born October 15, 1979, sparked his interest in acoustics and data acquisition learning audio recording techniques in multiple recording studios before college. He further explored signal processing in the context of vocal and guitar active effects processors. These experiences provided a practical foundation that his subsequent education would turn into a career path.

David obtained a B.S. from the department of Mechanical and Aerospace Engineering with a Minor in Mathematics from the University of Missouri at Rolla in May of 2002. He later received a Ph.D. from the department of Mechanical and Aerospace Engineering from the Missouri University of Science and Technology in December of 2010. His areas of study included acoustics, mechanical instrumentation and experimentation, mechatronics, control systems, vibrations, and robotics.